Photophysics of Lead-Halide Perovskites

Simon A. Bretschneider

Max Planck Institute for Polymer Research

I hereby declare that I wrote the dissertation submitted without any unauthorized external assistance and used only sources acknowledged in the work. All textual passages which are appropriated verbatim or paraphrased from published and unpublished texts as well as all information obtained from oral sources are duly indicated and listed in accordance with bibliographical rules. In carrying out this research, I complied with the rules of standard scientific practice as formulated in the statutes of Johannes Gutenberg-University Mainz to insure standard scientific practice.

Contents

Abstract

The Sun provides Earth with a greenhouse gas free source of energy that exceeds the annual energy consumption by orders of magnitude. Current solar cell technology limits the percentage of harvested solar energy that can be used to generate electricity; this is why new concepts and materials for photovoltaics are being explored. Lead-halide perovskite solar cells offer the chance for low-cost high-performance devices. As a result of the rapid technological development, perovskite solar cells have reached power conversion efficiencies exceeding 22% at the laboratory stage, which is comparable to established thin-film technologies. The success of lead-halide perovskites is based on the impressive charge transport and remarkably low recombination rates for a solution-processable semiconductor along with high optical absorption. Low transport and recombination losses in combination with a thin light absorbing layer are essential for a high-performance and low-cost solar cell. Despite their success in numerous optoelectronic devices, some of the most fundamental material and physical properties of lead-halide perovskites are still under intense debate.

The work included in this thesis is dedicated to the investigation of the photophysical properties of lead-iodide perovskites. The photophysics is discussed for three processes, here introduced in order of their occurrence, following photo-excitation of the material: the formation of polarons on a sub-picosecond timescale, the slow cooling of charge carriers on the order of hundred picoseconds and the radiative recombination in the nanosecond time range. The first chapters introduce solar energy, the theoretical background, and methodology followed by a summary of the experimental work performed during this thesis work. Using time-resolved THz spectroscopy, the formation of polarons was observed and quantified. Polarons in tetragonal $CH_3NH_3PbI_3$ and $CH(NH_2)_2PbI_3$ are formed within 0.4 picoseconds independent of the temperature. The formation of polarons resolves fundamental questions of the origin of the moderate charge carrier mobility and low radiative recombination. Along with the formation of polarons, charge carriers cool on two different timescales. The majority of the charge carriers cools within a few picoseconds. A smaller fraction of charge carriers cools much slower, requiring tens of picoseconds to reach the band minima, two orders of magnitude slower than in GaAs. The slow cooling of charge carriers was investigated using transient

absorption spectroscopy. The recombination of charge carriers was investigated on two different timescales using time-resolved photoluminescence spectroscopy. Concomitant to the slow cooling of charge carriers, high-energy photon emission with a photon energy in excess of up to 0.15 eV compared to the band edge emission was observed. The influence of different processing techniques to the recombination of charge carriers was investigated on a nanosecond timescale. As a result of the different processing conditions, the density of trap states changes along with the morphology of the perovskite film.

These results provide new insights into the fundamental properties, such as polaron formation and carrier cooling in lead-halide perovskites, and link the extrinsic characteristics, for instance trap density, to photophysical processes like the radiative recombination.

Kurzfassung

Die von der Sonne abgestrahlte Energie, welche die Erdoberfläche erreicht, übertrifft den aktuellen Energieverbrauch der Menschheit bei weitem. Da bei der Erzeugung von Strom und Wärme mittels Solarenergie keinerlei Treibhausgase emittiert werden, ist Solarenergie nicht nur im Überfluss vorhanden, sondern auch klimaneutral. Der weitere Ausbau der Produktion von Solarstrom ist aktuell vor allem durch die Effizienz von günstig verfügbaren Solarzellen beschränkt. Um deren Effizienz zu steigern, werden daher verschiedene Konzepte und Materialien erforscht. Ein vielversprechendes Material sind bleihalogenide Perowskite. Diese werden bereits erfolgreich als hocheffiziente und potentiell kostengünstige Solarzellen unter Laborbedingungen verwendet. Als Folge einer rasanten technologischen Entwicklung erreichen Perowskitsolarzellen eine Effizienz von mehr als 22%. Diese Effizienz ist vergleichbar mit dem Wirkungsgrad von etablierten Dünnschichtsolarzellen und nur wenig niedriger als die Effizienz von Siliziumsolarzellen, die bei 26% liegt.

Der Erfolg von bleihalogeniden Perowskiten als absorbierendes Material für Solarzellen hängt mit ihren herausragenden Materialeigenschaften zusammen. Perowskite vereinigen guten Ladungstransport und niedrige Rekombinationsraten mit hoher Absorption und guter Lösungsmittelprozessierbarkeit. Dies sind Eigenschaften, welche kostengünstige und hocheffiziente Solarzellen auszeichnet. Obwohl der Wirkungsgrad von Perowskit-basierten Solarzellen bereits dreiviertel der theoretisch möglichen Effizienz erreicht hat, sind viele Fragen zum Verständnis der grundlegenden Prozesse in bleihalogenide Perowskiten noch nicht komplett beantwortet.

Diese grundlegenden Fragen, welche in dieser Dissertation diskutiert werden, beschäftigen sich mit der Photophysik von auf Bleiiodid basierten Perowskiten. Die Photophysik wird anhand von drei Beispielen, geordnet nach ihrem zeitlichen Auftreten, diskutiert: die Entstehung von Polaronen im Bereich von wenigen Pikosekunden, das Abkühlen von heißen Ladungsträgern im Zeitraum von einhundert Pikosekunden und die Rekombination von Ladungsträgern im Nanosekundenbereich.

In den ersten drei Kapiteln wird die Photophysik von Perowskiten, die theoretischen Grundlagen sowie die Methodologie vorgestellt. Daran anschließend werden die

Ergebnisse dieser Dissertation diskutiert. Die Entstehung von Polaronen wurde mittels zeitaufgelöster THz Spektroskopie untersucht. In $CH_3NH_3PbI_3$ und $CH(NH_2)_2PbI_3$, die in tetragonaler Struktur vorliegen, kann die Entstehung von Polaronen in 0.4 Pikosekunden unabhängig von der Temperatur beobachtet werden. Die Entstehung von Polaronen liefert eine mögliche Erklärung für die nur moderat hohe Ladungsträgermobilität und niedrigen Rekombinationsraten, deren Ursprung bisher nicht zweifelsfrei geklärt werden konnte. Parallel zur Entstehung von Polaronen kühlen heiße Ladungsträger in zwei zeitlich verschiedenen Regimen ab: Ein Großteil der Ladungsträger kühlt innerhalb von wenigen Pikosekunden ab, ein kleiner Anteil innerhalb von mehreren zehn Pikosekunden. Das langsame Abkühlen von Ladungsträgern wurde detailliert mit transienter Absorptionsspektroskopie untersucht. Die Rekombination von Ladungsträgern wurde ebenfalls auf zwei verschiedenen Zeitskalen untersucht. Photolumineszenz mit einem Energieüberschuss von 150 meV im Vergleich zur Photolumineszenz, welche von den Bandminima ausgeht, wurde parallel zum Abkühlen der heißen Ladungsträger im Bereich von etwa hundert Pikosekunden beobachtet. Der Einfluss verschiedener Herstellungsmethoden wurde anhand der Rekombination von Ladungsträgern im Nanosekundenbereich untersucht. Dabei stellte sich heraus, dass sich bei der Verwendung verschiedener Herstellungsmethoden neben der Morphologie der Perowskitschicht auch die Dichte der Störstellen ändert.

Die präsentierten Ergebnisse erlauben neue Einblicke in die Photophysik von Bleiiodidbasierten Perowskiten, beispielsweise die Entstehung von Polaronen und das Abkühlen von Ladungsträgern. Ebenso wird der Zusammenhang zwischen extrinsischen Eigenschaften wie der Störstellendichte und der dazugehörigen photophysikalischen Charakteristika beleuchtet.

1. Introduction

Due to the anthropogenic emission of greenhouse gases, which starting during the beginning of the industrialization in the middle of the 19th century, the concentration of carbon dioxide in the atmosphere has increased by a factor of two above the average of the last 400.000 years. Climate change is a fact. Without a significant reduction of the emission of greenhouses gases, the global average temperature will rise by 4 °C by 2100. Even though the commitment to fulfill the resolution of the Paris climate agreement may be questionable, economic factors indicate change: the amount of emitted carbon dioxide per $ increase of the gross domestic product decreased by 18% and the average prices of roof-top photovoltaic installations decreased by 54% in the United States between 2008 and 2015. [Oba17] The total amount of consumed energy[1] in 2015 was 110 PWh. 40% of the consumed energy was oil-based, only 20% was electricity. The energy consumption is projected to increase drastically, until 2040 e.g. by 12 PWh from India alone and by 9 PWh from China, which share the biggest fractions of the total increased consumption. It is expected that until 2040 up to two-thirds of the additional installed power capacity will come from renewable sources owing to the projected low costs of renewable energy power plants, specifically about 75 GW to-be-installed power from solar energy.[2] The price of solar energy based on bids to electricity auctions[3] was 81$ per MWh for production in Germany, which is still higher compared to new coal plants (55$) or natural gas plants (45$). However, for production in more favorable regions, such as the US or Chile, bids were as low as 30$ per MWh, making photovoltaics the cheapest source of power.[4] These low prices are mostly based on scaling effects of the solar cell production, for instance the increased ingot size of silicon and more efficient production methods. For silicon-based photovoltaics, the possible efficiency enhancement arises from multi-junction-cells, i.e. stacked solar cells with different absorber materials. Proposed materials in addition to silicon are Kesterites, however in the last years another material, which allows tunable absorber properties and is suitable for high-performance solar cells has appeared: halide perovskites.

---

[1]Total final consumption, obtained from the total primary energy supply after losses due to conversion to ready-to-use energy, IEA Key world energy statistics 2017.
[2]IEA world report 2017
[3]Where is the solar industry headed (Martin A. Green, UNSW Wales, 30.11.17)
[4]IRENA Energy auctions executive summary 2016

Lead-halide perovskites have emerged as promising materials for optoelectronic devices in late 2012 and have made an astonishing rise in the science community [Koj09, Lee12]. Solar cells prepared from halide perovskites can be solution-processed and utilize cheap feedstock. Even though the technology is still in the laboratory phase, its implementation in multi-junction solar cells is already state of the art with power conversion efficiencies reaching almost 24 % for copper indium gallium selenide (CIGS) based photovoltaics and 27% for Si-based photovoltaics. [She18, Nah18] The preparation and engineering of perovskite absorption layers is still a challenge, especially for larger (>1 cm^2) areas. In addition to the technological challenges, fundamental properties of the material, such as the origin of the extraordinary low recombination rates, are still under investigation. [Her16b, Str17, Sum16].
This thesis aims to investigate the fundamental photophysical and engineering-related properties of solution-processed lead-iodide using ultrafast spectroscopy.

1.1. Outline of this thesis

Three different ultrafast spectroscopy techniques (transient absorption spectroscopy, time-resolved photoluminescence spectroscopy, time-resolved Terahertz (THz) spectroscopy) have been used here to investigate the photophysical properties in the femto- to nanosecond region, spanning from the visible to the THz spectral range. This thesis is organized as follows:
In **chapter 2**, the underlying principles of semiconductors, solar cells and ultrafast spectroscopy are introduced, especially those which are required in order to investigate the properties of charge carrier generation, cooling and recombination. In **chapter 3**, the used perovskite deposition and spectroscopy methods are introduced. In **chapter 4**, the generation of polarons and initial cooling of charge carriers in lead-iodide perovskites using time-resolved THz spectroscopy is investigated: polarons were found to form temperature-independently within 400 fs, whereas the cooling of charge carriers is dependent on both the initial excess pump energy and temperature. **Chapter 5** analyses the cooling of hot carriers in lead-iodide perovskite using transient absorption and time-resolved photoluminescence spectroscopy. It is found that excitation of the perovskite above an energy of 2.5 eV results in a cooling of hot carriers and subsequent repopulation of the band-edges in the order of 100 ps, simultaneously to the emission of high-energy photons. In **chapter 6**, the photophysical changes of lead-iodide perovskite films before and after methylamine treatment are explored using temperature and time-resolved photoluminescence spectroscopy. The measurements show that the treatment results in a blue shift of the emission and a reduction of the trap-assisted lifetime. Both effects are attributed to the increased trap density and structural disorder. Furthermore, the effects of the treatment to solar cells

were investigated. The enhanced power conversion efficiency due to the treatment originates from improved morphology and charge carrier extraction. **Chapter 7** summarizes the thesis and provides an outlook.

2. Theoretical Background

2.1. Semiconductors

In solid state physics, one distinguishes three types of materials based on their properties: metals, semiconductors and insulators. Two characteristic properties are used to differentiate between the materials, the electrical conductivity at temperatures near 0 K[1], the presence of forbidden energy levels at the Fermi level E_F (lowest unoccupied state) and width of the energy gap. Metals are conductive at 0 K and E_F lies within a band of allowed energy states. Semiconductors and insulators are non-conductive at 0 K and E_F lies within a band of forbidden energy states. A semiconductor can be distinguished from an insulator by its behavior upon the addition of an external charge and the ability to adjust the conductivity. In an insulator, an additional electron will be strongly localized close to the positively charged ions, whereas in the case of a semiconductor the electron interacts only weakly with the lattice and therefore can be described as a free electron. The electric conductivity of a semiconductor can be tuned over a broad range due to the addition of atoms with excess positive or negative charge (doping). [Lei11] For a more detailed look on the background of charge carriers in a semiconductor, the electronic band structure will be introduced.

2.1.1. Electronic band structure

In order to describe the properties of an electron in a solid, the time-independent Schrödinger equation needs to be solved under the condition of a periodic potential V($\boldsymbol{r}$), which reads:

$$\mathcal{H}\psi(\mathbf{r}) = \left(-\frac{\hbar^2}{2m}\Delta + V(\mathbf{r})\right)\psi(\mathbf{r}) = E\psi(\mathbf{r}). \qquad (2.1)$$

Here, $\mathcal{H}$ is the Hamiltonian, ψ a wave function, $\hbar$ the reduced Planck constant, m the mass of the electron, Δ the Laplace operator and E the energy of the electron. To solve the Schrödinger equation, it is beneficial to transform the coordinate system from real space

---

[1]Specific: zero thermal energy for an ideal crystal.

to the reciprocal space, also called **k**-space. Upon Fourier transformation of a lattice in the real space, a lattice in the reciprocal space is obtained. The reciprocal lattice can be described with the vector $\mathbf{G} = h\mathbf{g}_1 + k\mathbf{g}_2 + l\mathbf{g}_3$, where the $\mathbf{g}_i$ are the base vectors and h,k and l the so called *Miller*-indices. A solution to the Schrödinger equation in a periodic potential is a modulated plane wave, also called *Bloch wave*:

$$\psi(\mathbf{k}) = u_k(\mathbf{r})e^{i\mathbf{k}\mathbf{r}},$$

where **k** is the wave vector, which adapts values of $k_i = 0, \pm 2\pi/L, \pm 4\pi/L, ...$ with $i = x, y, z$ and L the macroscopic dimension of the crystal, $u_k(\mathbf{r}) = u_k(\mathbf{r} + \mathbf{r}_n)$ describes the periodicity of the lattice and therefore the potential V($\mathbf{r}$) [Iba09]. Utilizing the periodicity of the lattice we can rewrite equation 2.1:

$$\mathcal{H}\psi_{\mathbf{k}} = \mathcal{H}\psi_{\mathbf{k+G}} = \mathrm{E}(\mathbf{k})\psi_{\mathbf{k}}$$
$$= \mathrm{E}(\mathbf{k})\psi_{\mathbf{k+G}}.$$

Due to the equivalence of E(**k**) and E(**k+G**), i.e. the periodicity of E(**k**), it is sufficient to describe E(**k**) in the entire periodic lattice via the investigation of the E(**k**) in the first Brillouin zone with the boundaries $G = \pm 2\pi/a$. The energy surface E(**k**) is the also known better as the *electronic band structure*.
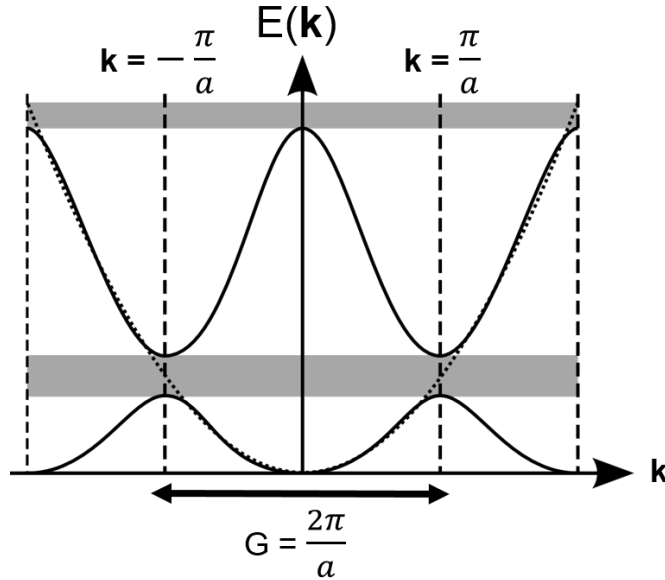

Figure 2.1.: Schematic representation of the one-dimensional energy surface E(**k**) of a nearly-free electron in a periodic lattice (solid line) with the lowest two energy gaps (gray-shaded areas) at the boundaries of the Brillouin zone at $\pm\pi/a$. The dotted line represents the energy surface of the free electron for comparison. Adapted from [Iba09]

For an electron which is weakly perturbed due to a potential, a *nearly free* electron, the energy in one dimension can be calculated as $E(k) = \hbar^2 k^2/2m_e$ [Iba09]. Due to the periodicity of the potential, the energy of the electron is degenerated at the boundary of the Brillouin zone at $G = \pm\pi/a$ (as indicated in figure 2.1). As a result of the energetic degeneracy, the description of an electron at $G = \pm\pi/a$ is by definition a superposition of at least two plane waves. [Iba09] In the case of two counter-propagating plane waves with $\psi_{1,2} = \exp(\pm i\pi x/a)$, constructive interference of the two waves occurs at $k = \pm G/2$ due to the (Bragg-) reflected wave at the neighboring atom. The corresponding probability densities, ψ^2, of the standing waves have a maxima either at the atom or in between the two atoms. For the former case, the energy at the boundary of the Brillouin zone is reduced, for the latter one increased, which in combination with the net-zero velocity of the standing wave ($\partial E/\partial k = 0$) at the boundary results in an energy gap and flat band structure at $G = \pm\pi/a$ (see figure 2.1).[2]

An alternative method to calculate the band structure is the tight-binding model. Here, the approach is to utilize that most of the electrons are localized closely to the core of the atom and therefore retain the majority of the characteristics of a free atom. Only a small fractions of total electrons of an atoms can be considered as nearly-free. [Iba09] For the calculation of the electronic band structure of lead-halide perovskites, much more sophisticated methods are required. An approach is the Kohn-Sham density function theory, which is modified using gradient approximation for the energy and spin-orbit coupling [Koh65, Dem16, Zhe15a] or molecular dynamics [Fro16b].

An important characteristic property derived from the band structure is the effective mass of the electron, which can deviate from the free electron mass [Iba09, Lei11]. In the vicinity of the band minima, the energy of an electron can be approximated using the energy of an electron in vacuum (*effective mass approximation*), but with an effective (tensorial) mass:

$$\left(\frac{1}{m^*}\right)_{i,j} = \frac{1}{\hbar^2}\frac{\partial^2 E(\mathbf{k})}{\partial k_i \partial k_j}$$

The curvature of the electronic band is related to the effective mass (high effective mass $\leftrightarrow$ more flat curvature of the band and vice-versa). Another important quantity related to the band structure is the density of states (DOS), D(E). The DOS can be calculated by integration of a shell of the energy surface E($\mathbf{k}$):

$$D(E) \simeq \frac{1}{(2\pi)^3}\int\limits_{E(\mathbf{k}=const.)}\frac{1}{|\nabla E(\mathbf{k})|}dE$$

---

[2]For a more detailed discussion, see [Iba09]

Important for the calculation of the DOS are flat areas in the energy surface (where $|\nabla E(\mathbf{k})|$ vanishes), which result in critical point of the DOS, e.g. high or low density of states. For a parabolic energy surface, the DOS scales with the square root of the energy: $D(E) \sim \sqrt{E}$. The calculated DOS is valuable to connect the electronic band structure and derived experimental data, such as in section 5.1. [Dem16, Iba09]

The occupation of the energy bands at a given temperature and energy gap determines the properties of a solid as illustrated in Fig. 2.2, either metallic, insulating of semi-conducting behavior.
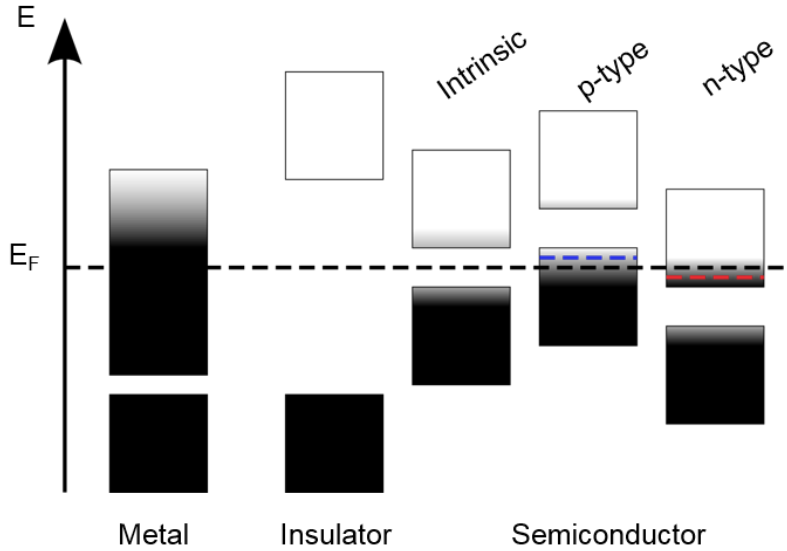
Figure 2.2.: Schematic energy diagrams of a metal, insulator and semiconductors at non-zero temperature, the color gradient represents the population of a band (white equals empty, black full). The metal has a population above the Fermi level E_F, allowing conduction even at zero temperature. The insulator has a large band gap between the highest occupied band and lowest unoccupied band. Semiconductors have a smaller band gap compared to insulators, which allows thermally-activated population of the valence band for an intrinsic semiconductor. For doped semiconductors, the Fermi energy is closer to the valence/conduction band. The dashed blue/red lines represent the doped states. Adapted from [Iba09]

For electrons and holes[3], which are fermions and therefore follow the Pauli-principle, the population follows the Fermi-distribution:

$$f(E,T) = \frac{1}{\exp\left(\frac{E-E_F}{k_B T}\right) + 1},$$ (2.2)

where k_B is the Boltzmann constant, T the temperature and E_F the Fermi energy, which marks the difference between populated and unpopulated states at 0 K [Iba09]. From equation 2.2 and illustrated in figure 2.2, it can be seen that for elevated temperature, even states above the (energy) band gap may be populated. For an insulator, the band gap is too large to allow thermal population of the intrinsically empty band at reasonable temperatures. Consequently, the valence band (VB) combines the highest populated states at 0 K. For an intrinsic semiconductor at room temperature, a small (thermally-induced) population in the otherwise empty band above the Fermi energy band (conduction band, CB) exists. As an example, in Silicon (Si), the intrinsic charge carrier density, n, is $1.5 \cdot 10^{10}\ cm^{-3}$, around 10 orders of magnitude lower than in e.g. copper [Iba09]. The number of charge carriers in the conduction band can be increased by unintentional (impurities) or intentional doping, either increasing the number of electrons (donating electrons) or holes (accepting electrons). In case of intentional doping, the energy required to ionize donor/acceptor is small, therefore enhancing the number of charge carriers at finite temperatures. For Si, which has four valence electrons, phosphor acts as a donor of electrons (five valence electrons) and boron acts as an acceptor (three valence electrons). In the case of small ionization energies (thermal energy at room temperature $E = k_B T \sim 26$ meV$\sim$ 6.2 THz), the dopants become ionized at room temperature. For the case of a donor, the number of electrons in the conduction band increases (n-type doping, see also figure 2.2) and the Fermi level at room temperature is shifted much closer to the conduction band. For the case of an acceptor (p-type doping, see figure 2.2), the number of holes close to the valence band maximum increases and the Fermi level is shifted closer to the valence band. For unintentional doping (e.g. point, line and plane defects, dangling bonds at the surface, impurities, interstitial heavy atoms) the ionization energy is more likely to be much higher than $k_B T$ and results in trapped charge carriers. A high density of trap states is highly detrimental to the mobility of a charge carrier and enhances the non-radiative recombination of electrons from the conduction and holes from the valence band (see section 2.5).

For the case of the nearly-free electron in a periodic lattice (see figure 2.1) and as illustrated in figure 2.3, the minimum of the valence band and the maximum of the conduction band share same value of $\boldsymbol{k}$. This is the case for e.g. GaAs and is called a *direct* (energy)

---

[3]After excitation of an electron with an energy larger than the energetic gap, a vacant state is created, called a *hole*. This quasi-particle behaves like an electron with negative effective mass and a positive charge.
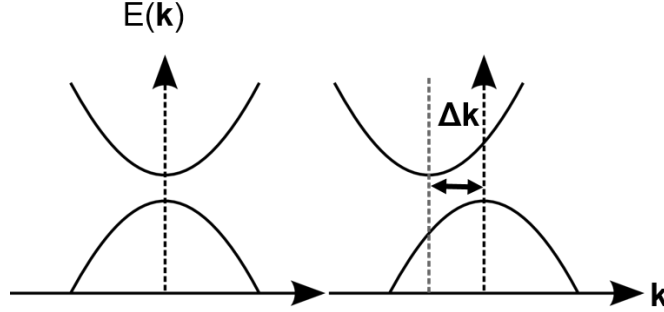
band gap.

Figure 2.3.: Schematic illustration of a direct and an indirect band gap. The band minima of the direct band gap have the same position in the k-space. For an indirect band gap, there is an offset of $\Delta\mathbf{k}$ in k-space exists between the band minima.

For silicon, the band minima are separated in k-space by Δk, making the band gap *indirect*. The nature of the band gap, whether it is direct or indirect, relates to the properties of the semiconductor, especially to the emission/recombination and absorption probabilities. In order to absorb or emit a photon with the energy of the indirect band gap and in fulfillment of the energy and crystal momentum conservation, the additional incorporation of a quasi-particle, a *phonon*, is required. A phonon is of small energy ($E_{\text{phon}} \ll E_{\text{phot}}$), but allows the requirement of conservation of crystal momentum to be met: $\mathbf{k}_{\text{phot}} = \Delta\mathbf{k} - \mathbf{k}_{\text{phon}} = 0$. Due to the necessity of an additional phonon, the phonon-assisted indirect absorption and emission are less likely in comparison to the absorption and emission of a direct band gap semiconductor.

2.1.2. Phonons and carrier-phonon interaction

When electrons and lattice ions are not considered separately as above, the Hamiltonian also include terms that describe the lattice motion and the coupling between electrons/holes and the lattice:

$$\mathcal{H} = \mathcal{H}_{\text{electron}} + \mathcal{H}_{\text{lattice}} + \mathcal{H}_{\text{coupling}} \tag{2.3}$$

The Hamiltonian of the lattice $\mathcal{H}_{\text{lattice}}$ also depends on the position of the electrons, which is why the *Born-Oppenheimer*-approximation is used. Due to the large mass difference between electrons and lattice ions, their motion happens on different timescales (electrons fast; ions much slower). Electrons move in an effectively *frozen* ionic potential; the lattice ions move within time-averaged parametric electron potential, i.e. the electrons follow the

lattice ion motion parametrically. [Lei11] The solution of the lattice-Hamiltonian is a set of coupled harmonic oscillators which have quantized energies. The quasi-particle of the lattice vibration is the phonon, which is is a Boson [Iba09, Giu17]. In analogy to the electronic band structure, phonons also have an energy surface, called dispersion relation. For a two-atomic base (i.e. GaAs, CdTe), the dispersion of a linear chain is the following:

$$\omega^2(k) = f\left(\frac{1}{M_1} + \frac{1}{M_2}\right) \pm f\sqrt{\left(\frac{1}{M_1} + \frac{1}{M_2}\right)^2 - \frac{4}{M_1 M_2}\sin^2\frac{ka}{2}}, \qquad (2.4)$$

where M_i are the masses of the base atoms, f the coupling constant between the atoms and a the distance between two identical atoms. [Iba09]. For a base with more than one atom, we can identify both *optical* and *acoustic* phonons, respectively (as illustrated in figure 2.4). If two neighboring atoms are displaced in the same direction, we speak of acoustic phonons (minus sign in equation 2.4). If they are displaced in different directions, we classify the corresponding phonon as optical (plus sign in equation 2.4). The out of phase motion of neighboring atoms creates a dipole moment that can couple to an electromagnetic field. In addition to the optical and acoustic phonons, another classification of phonons can be made by considering the direction of atomic displacement with respect to the wave-vector $\boldsymbol{k}$. If the displacement is parallel to $\boldsymbol{k}$, one speaks of longitudinal phonons. For displacement perpendicular to $\boldsymbol{k}$ we speak of transverse phonons. The number of phonon modes is dependent on the dimensionality of the lattice and the number of atoms, N, in the unit cell/atomic base. We find 3 acoustical (specifically one longitudinal acoustic (LA) and two transverse acoustic (TA)) and $3N$-3 optical phonons [Iba09]. The factor of three originates from the three degrees of freedom of an atom. Due to the quantized energy of the phonon and its bosonic nature, the average excitation number follows the Bose-Einstein distribution [Zeg11]:

$$\langle n \rangle = \frac{1}{\exp\left(\frac{E - E_F}{k_B T}\right) - 1}.$$

In combination with the discrete energy of a quantum mechanical oscillator $E_n = (n + 1/2)\hbar\omega$, we obtain the average internal energy for a single atomic unit cell in three dimensions, $\langle U \rangle \sim 3N\hbar\omega(1/2 + \langle n \rangle)$ [Iba09]. The *Debye* temperature Θ_D is relevant for the thermal population of phonons. of a semiconductor. Based on the Debye approximation (thermal excitation can be approximated as a superposition of plane waves in a homogeneous elastic medium), it describes the temperature, above which states are occupied. The Debye temperature can be calculated $\Theta_D = \hbar v_s / k_B \sqrt[3]{6\pi^2 N/V}$, where v_s is the speed of sound and N/V the atom density [Iba09]. In addition to the properties of the phonons which are described by $\mathcal{H}_{\text{lattice}}$, the last term in equation 2.3, $\mathcal{H}_{\text{coupling}}$, describes
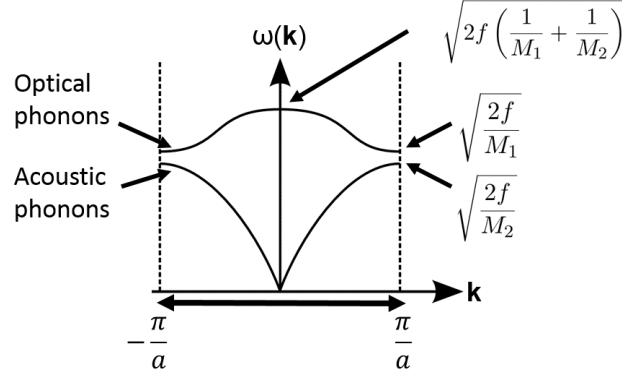
Figure 2.4.: Schematic illustration of the phonon dispersion relation for a two-atomic base. One can distinguish the higher frequency optical phonon branch and the lower frequency acoustic phonon branch with the respective frequencies calculatable from the masses and the coupling frequencies in the center and at the boundary of the Brillouin-zone. Adapted from [Iba09]

the coupling of charge carriers and phonons. Two general types of interactions can be distinguished, either the interaction via the (short-range) deformation potential (which locally perturbs the lattice and changes the electronic band structure) or the (long-range) polar-optical interaction, which dominates in polar semiconductors like GaAs, CdTe or $MAPbI_3$. The polar-optical interaction is the interaction of charge carriers with LO-phonons. [Lei11, Giu17] Two important examples of the polar-optical interaction are the cooling of hot carriers (see section 2.5) or the formation of polarons. A polaron is a charge carrier dressed by nuclear polarization. [Zhu15b] Depending on the strength of the interaction between a charge carrier and LO-phonon, polarons can be described with a coupling constant α:

$$\alpha = \frac{e^2}{\hbar c}\sqrt{\frac{m_e^* c}{2\hbar\omega_{LO}}}\left(\frac{1}{\varepsilon_\infty} - \frac{1}{\varepsilon_0}\right), \tag{2.5}$$

where c is the speed of light, e the fundamental charge, ω_{LO} the angular frequency of the coupled LO-phonon, ε_∞ the optical and ε_0 the static dielectric constant. When the interaction is strong, i.e. $\alpha > 10$, the polarons are classified as *small* and are found e.g. in organic semiconductors. When the interaction is weaker, i.e. $\alpha \lesssim 10$, the polarons are classified as *large*. Polarons in $MAPbI_3$ are described as intermediate-large with $1.1 < \alpha < 2.7$. [Zhu15b, Fro17a] As a result of the dressing of the charge carriers, the mass of the polaron in higher compared to the effective mass of the band electron. The dressing also results in a reduced scattering of polarons and phonons.

2.1.3. Semiconductor devices

One of the most important applications of a semiconductor is a solar cell. In a solar cell, an incident photon generates an electron-hole pair, which is then separated and each of the charge carriers then drifts to the contacts, where the charge carriers can be harvested. Solar cells as well as the light-emitting diodes and semiconductor lasers use a junction of at least two differently doped semiconductors, the so called p-n junction.
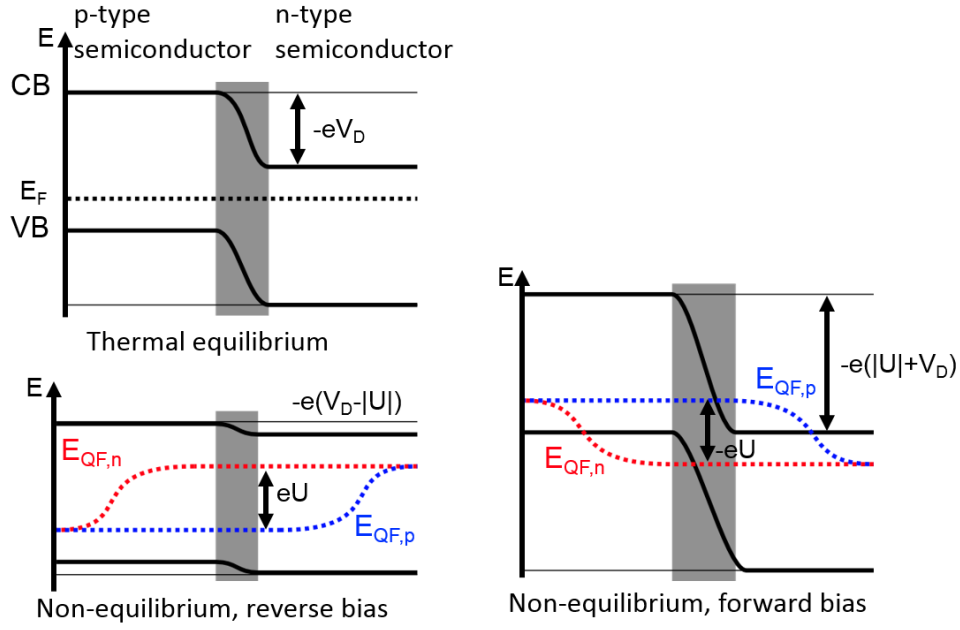
Figure 2.5.: Schematic illustration a p-n junction under thermal equilibrium with the resulting built-in potential V_D and under non-equilibrium conditions with reverse/forward bias $\pm U$. Under equilibrium conditions, the p- and n-type doped semiconductor align with respect to the common Fermi-energy E_F. Under non-equilibrium conditions, the Fermi level splits, resulting in the quasi-Fermi-levels $E_{QF,p}$ and $E_{QF,n}$. The gray area corresponds to the depletion region which expands under forward bias with respect to the equilibrium case and shrinks under reverse bias conditions.

Also established is p-i-n junction, where an intrinsic semiconductor layer is sandwiched between the n- and the p-type semiconductor. Once the n- and p-type semiconductors are connected (under equilibrium conditions, therefore with a common Fermi-energy), the excess charge carriers originating from doping close to the interface will diffuse to the oppositely doped semiconductor in order to minimize the concentration gradient of excess charge carriers. The diffusing electrons recombine with holes and leave ionized

acceptors and donors in the so called *depletion region*, thus creating an electric field (see figure 2.5, upper panel) at the interface. The electric field prevent prevents the diffusion of additional charge carriers after its establishment. This electric field is called the *built-in potential V_D* and can be calculated from the charge carrier densities in the p- and n-type semiconductors N_A and N_D. [Zeg11] In non-equilibrium conditions, e.g. under illumination or external bias *U*, the Fermi energies in the n-type and p-type semiconductor are not identical anymore, therefore a common E_F can not be used anymore. As a consequence, the carriers in the n- and p-type region need to be described with separate Fermi-Dirac distributions. Instead of a common E_F, quasi-Fermi-levels E_{QF} are used. The p-type region is described with $E_{QF,p}$, the n-type region with $E_{QF,n}$. The splitting of the quasi-Fermi-levels can be described with a potential difference $\Delta E_F = \pm eU$. Depending on the sign of ΔE_F, we can distinguish two different cases. For the case of $\Delta E_F > 0$, the sum of built-in and quasi-Fermi-level splitting potential difference is decreased, therefore lowering the energy barrier between the n- and p-type semiconductor. The corresponding depletion zone shrinks which allows thermally excited carriers to pass the junction (called reverse bias). For the case of forward bias, the sum of the potential difference of built-in and quasi-Fermi-level splitting is increased and therefore expands the depletion region [Zeg11, Iba09, Lei11] The potential difference between the quasi-Fermi-levels is also the ultimate limitation for the open-circuit voltage, one of the important parameters of a solar cell. The transition of the equilibrium to the non-equilibrium condition of the p-n junction requires the interaction of the semiconductor and electromagnetic radiation, i.e. light-matter interaction.

2.2. Light-matter interaction

The interaction of electromagnetic waves and matter leads to electronic (excitation of an electron to a higher energetic state), lattice (e.g. excitation of a phonon) or magnetic excitation (e.g. of spins) of a solid if the energy of the field is sufficient to excite the transition. The two most fundamental phenomena of light-matter-interaction, absorption and emission, can be explained most clearly using the simple case of an electronic two-level system. The two levels are named E_1 and E_2 with $E_2 > E_1$. If a photon with the energy E_2 - E_1 = hν interacts with the previously unexcited system, the photon is absorbed and its energy is transferred to an electron, which therefore is excited from E_1 to E_2. The probability of the system to absorb the photon $\frac{d}{dt}\rho_{12}$ can be described with the with spectral energy density ρ_ν and the so called *Einstein coefficient* of the absorption B_{12}: $\frac{d}{dt}\rho_{12} = B_{12}\rho_\nu$. If a photon with the energy E = hν interacts with the excited two level system, a photon with the energy E = hν is emitted in addition to the incoming photon. This process is called stimulated emission and is subsequently described with the

Einstein coefficient B_{21}. The system can also return to its ground state by the emission of a photon without the presence of an external electromagnetic field. The probability of the spontaneous emission can be described with the Einstein coefficient A_{21}. The spontaneous emission and absorption are proportional to each other with the pre-factor of the cubed frequency: $A_{21} \sim \nu^3 B_{21}$. In a two-level system, B_{21} and B_{12} are equal. [Dem08]

In the quantum mechanical description, the eigenstate of the two-level system can be written as $|\psi\rangle = c_0|0\rangle + c_1|1\rangle$, where $|0\rangle$ is the ground and $|1\rangle$ the excited state. For a specified state $|\psi\rangle$, the probability to find a the system in state $|\psi\rangle$ is defined via the integral $\langle\psi|\rho|\psi\rangle$, where ρ is the density matrix $\rho(t) = |\psi(t)\rangle\langle\psi(t)|$. In the density matrix, the diagonal elements are defined as the population (via the expectation value (probability) of an observable, which is the trace of the density matrix multiplied with the observable). The off-diagonal elements are defined as the polarization (phase which describes the temporal evolution of the coherent superpositions, i.e. the light-induced coupling of the states).

The probability of transition between states can be described using Fermi's golden rule:

$$\Gamma_{i\rightarrow j} = \frac{2\pi}{\hbar}|\langle j|\mathbf{M}|i\rangle|^2\rho, \tag{2.6}$$

where ρ is the density of the j-like states and $\mathbf{M}$ interaction Hamiltonian (time-independent perturbation potential). [CT09] To analyze which conditions need to be fulfilled in order for an electronic transition to be significantly probable, we use the Born-Oppenheimer approximation in order to simplify the wave function. In the Born-Oppenheimer approximation, the electronic wave function depends only parametrically on the nuclear coordinates. The simplified wave function $|\psi\rangle$ reads:

$$\psi = \psi_{\text{electron}}\psi_{\text{nucleus}}\psi_{\text{spin}},$$

where ψ_{electron}, ψ_{nucleus} and ψ_{spin} are the wave functions of the electrons, the nuclei and the spins, respectively. Under the assumption that the nuclei are not far displaced from their equilibrium positions during the electronic transition, the interaction Hamiltonian interacts only with the electronic wave function. The resulting transition probability between two states reads:

$$\Gamma_{i\rightarrow j} \simeq |\langle\psi_{\text{el,j}}|\mathbf{M}|\psi_{\text{el,i}}\rangle|^2|\langle\psi_{\text{nuc,j}}|\psi_{\text{nuc,i}}\rangle|^2|\langle\psi_{\text{spin,j}}|\psi_{\text{spin,i}}\rangle|^2. \tag{2.7}$$

If $\langle\psi_{\text{el,j}}|\mathbf{M}|\psi_{\text{el,i}}\rangle$ is $\neq 0$, a transition is dipole-allowed, if $\langle\psi_{\text{el,j}}|\mathbf{M}|\psi_{\text{el,i}}\rangle$ is $= 0$, a transition is dipole-forbidden. A dipole-allowed transition is coupled to a significant transition prob-

ability. In order to calculate the transition probability, we also utilize the proportionality of first term in equation 2.7 to the overlap of the electronic wave functions of the initial and the final state, i.e. largest transition dipole moment for electronic states which have the greatest spatial overlap. The spatial overlap of the nuclei at the initial and final states is also called the *Franck-Condon* factor: $|\langle\psi_{\mathrm{nuc,j}}|\psi_{\mathrm{nuc,i}}\rangle|^2$. The Franck-Condon factor is derived from the Franck-Condon principle, stating that during the electronic transition, the positions of the nuclei are preserved, resulting in a transition from the vibrational ground state in the lower electronic state to a vibrational state in the excited state, which resembles the initial state most and is visualized in figure 2.6. The spin factor, $|\langle\psi_{\mathrm{spin,j}}|\psi_{\mathrm{spin,i}}\rangle|$ is only non-zero if the spins of the initial and the final state are identical.[4]

Qualitatively, an electronic excitation results in a different charge distribution of a solid, which results in a reorganization of the nuclei, therefore a vibrational/lattice transition. In an energy-internuclear distance graph, the potential minima of the ground state and the excited state are shifted in energy and space due to the different equilibrium position of the nuclei in the excited state. In practice, the overlap of all of the initial and final (electronic, multiple vibrational and spin) states determines the transition probability. [Fri05]

Kasha's rule, which relies on the Franck-Condon principle, states that emission from an excited electronic state originates from the lowest vibrational state due the internal conversion, i.e. in the excited state the cascading energetic relaxation via different vibrational state happens on much faster timescale compared to electronic transitions back down to the ground state. [Dem08]

2.3. Solar cells

After the interaction of visible electromagnetic radiation and the two semiconductors in a p-n junction, charges are generated. The figure of merit of a solar cell is the power conversion efficiency (PCE, η), relating the ratio between incoming radiative power and harvested electric power. The PCE can be calculated with the following parameters:

$$\eta = \frac{\mathrm{V_{OC}\,J_{SC}\,FF}}{\mathrm{P_0}},$$

where V_{OC} is the open circuit voltage, J_{SC} is the short circuit current density, $\mathrm{P_0}$ is the incident light intensity (AM1.5G standard; solar spectrum on the earth surface with a zenith angle of 37° with an incident power density of 100 mW/cm²) and FF is the fill

---

[4]Spin-orbit coupling effects do allow spin-forbidden transitions, i.e. for phosphorescence.
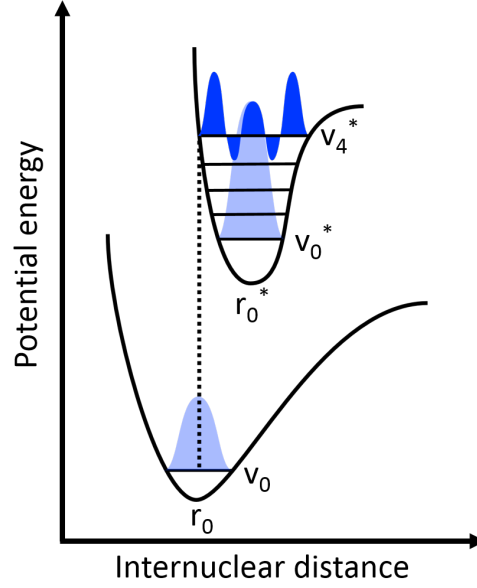
Figure 2.6.: Illustration of the Franck-Condon principle. Coupled to the electronic excitation, the excitation from the vibrational ground state occurs to the vibrational state in the excited electronic state, for which the spatially overlap of the wave functions is largest, in this case from the vibrational ground state v_0 to v_4^*. Adapted from [Fri05]

factor [Zeg11, Lei11]. The fill factor is the ratio of the theoretical available power defined by the product of V_{OC} and J_{SC}, and the measured power. The power conversion efficiency of single junction (i.e. one absorber material) solar cells is limited to 33.2 % for a band gap of 1.3 eV, the so called *Shockley-Queisser*-limit (SQ-limit) [Sho61]. If the incident photons have a lower energy than the band gap of the material, they can not be absorbed, therefore no current can be generated. For incident photons with a higher energy than the band gap, the excess energy is dissipated by heating the lattice and can not be used to increase the V_{OC}. The loss in current due to a small band gap and the loss in voltage due to energy dissipation are responsible for the major contribution of the SQ-limit. Another limitation arises from black-body radiation, which results in a temperature-dependent loss and thermodynamics (temperature difference between the sun and the solar cell). The SQ-limit does not include intrinsic losses due to non-radiative recombination. The highest efficiency of a single-junction solar cell without light concentration is a thin-film GaAs solar cell with an efficiency of 28.8 %, therefore reaching $\sim 87\%$ of the theoretical limit. [RN317, Sho61] Due to the band gap of ~ 1.6 eV for $CH_3NH_3PbI_3$, the maximum achievable efficiency is 31 %, the current best efficiency of a $CH_3NH_3PbI_3$-based device is 22.7%. [RN317, Sho61]

In order to overcome the SQ-limit, several concepts have previously been suggested, e.g. the generation of multiple carriers for a single high-energetic photon or the usage of

the hot carriers to generated additional voltage in a hot-carrier solar cell, however these concepts lack practical and relevant implementation yet. In order to utilize the below-band gap photons, multi-junction solar cells that consist of multiple stacked p-n junctions with different band gaps have been established. The current record efficiency of 46 % was reached with a four-junction solar cell and additional concentration of the sunlight. These solar cells are commonly of inorganic nature and manufactured using chemical vapor deposition. Another approach for multi-junction solar cells is the usage of band gap engineered halide perovskites.

2.3.1. Lead-halide perovskite solar cells

Solar cells, which use lead-halide perovskites as an absorber material, were introduced in 2009 and started their scientific breakthrough in 2012. Lead-halide perovskites combine a high absorption coefficient, high charge carrier mobility and a tunable band gap, which allows power conversion efficiencies exceeding 30%. [Koj09, Lee12]

2.3.1.1. Perovskite structure

The structure is based on the ABX_3-perovskite structure, derived from the mineral $CaTiO_3$. Specifically, the perovskite structure consist of corner-sharing octahedra, in the case of $CH_3NH_3PbI_3$, lead-iodide octahedron with iodine atoms at the corner and the lead-atom in the center of the octahedron. The cation, in general A, specifically methylammonium (MA, $CH_3NH_3^+$) is located in the cuboctahedral gap and surrounded by 8 octahedra (see figure 2.7). [Bre14]
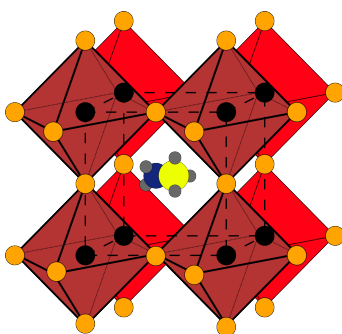

Figure 2.7.: Schematic illustration of the $CH_3NH_3PbI_3$ unit cell (dashed lines) for a cubic crystal structure. The lead atoms are shown in black, the iodide in orange, forming the octahedra (shown in red). The methylammonium cation in the cuboctahedral gap in shown in blue/yellow.

The cation can be exchanged for different molecular and atomic ions, e.g. formamidinium (FA, $CH(NH_2)_2^+$), Cs^+ or Rb^+. The stability of the three-dimensional perovskite structure is defined by the Goldschmidt's tolerance factor $t = r_A + r_X/\sqrt{2}(r_B + r_X)$, where r_A is the radius of the cation, r_B the radius of the B-cation and r_X the radius of the anion. [Sto13, Li17b] The dimensionality and the crystal structure depend on the value of the tolerance factor and the cation/anion-combination. Lead-halide perovskite with a tolerance factor between 0.8 and 1.0 will crystallize in a cubic structure whereas a tolerance factor between 0.7 and 0.8 will results in tetragonal and orthorhombic structures. $MAPbI_3$ has a tetragonal crystal structure at room temperature with fully randomized orientation of the MA-cation. Around 150 K, the material undergoes a phase transition to the orthorhombic structure and oriented MA-cations. Above 327 K, $MAPbI_3$ adapts a cubic structure. $FAPbI_3$ is cubic at room temperature and undergoes phase transition to a trigonal structure at 200 K and to an orthorhombic structure below 140 K. $FAPbI_3$ also has a non-perovskite phase at room temperature, $\delta-FAPbI_3$, it can be avoided when the films are annealed above 150 °C. [Bre14, Gra15b, Fro16b, Sto13, Wel15] For larger organic molecules such as ethylamine, the three-dimensional structure cannot be sustained and lower-dimensional perovskite structures form. [Wu15b, CB17]

2.3.1.2. Perovskite electronic structure and solar cells

The electronic band structure of the lead-halide perovskite around the band edges is dominated by the lead and iodine orbitals. In the tetragonal phase, the conduction band minima consists of Pb-6p orbitals, the valence band maximum of Pb-6s and I-5p orbitals. The contribution of the organic cations is small due to the large energy difference between the lowest unoccupied and the highest occupied level of the organic cation (the highest bands associated with the MA-cation are located ~ 6 eV below the top of the conduction band), which provides therefore primarily electrostatic compensation of the lead-iodide lattice. [Bre14, Dem16] The effective masses of electrons and holes are fairly similar and were experimentally and theoretically estimated to be $m_e^* \simeq 0.12 m_e$ and $m_h^* \simeq 0.15 m_e$. [Miy15, Fro17a] The density of states is dominated by the lead- and iodide orbitals. Including the substantial contribution of the spin-orbit coupling (SOC) due to the high atomic mass of the lead atoms, the band gap was calculated to be 1.54 eV at the Γ-point (see figure 2.8). [Dem16] The strong spin-orbit coupling in combination with broken inversion symmetry (due to the methylammonium cation) is the origin of another effect which affects the properties of the lead-halide perovskites substantially: Rashba-splitting. The Rashba-effect results in a lifting of the spin-degeneracy of the valence- and conduction bands, which can also be observed in figure 2.8. [Zhe15a]
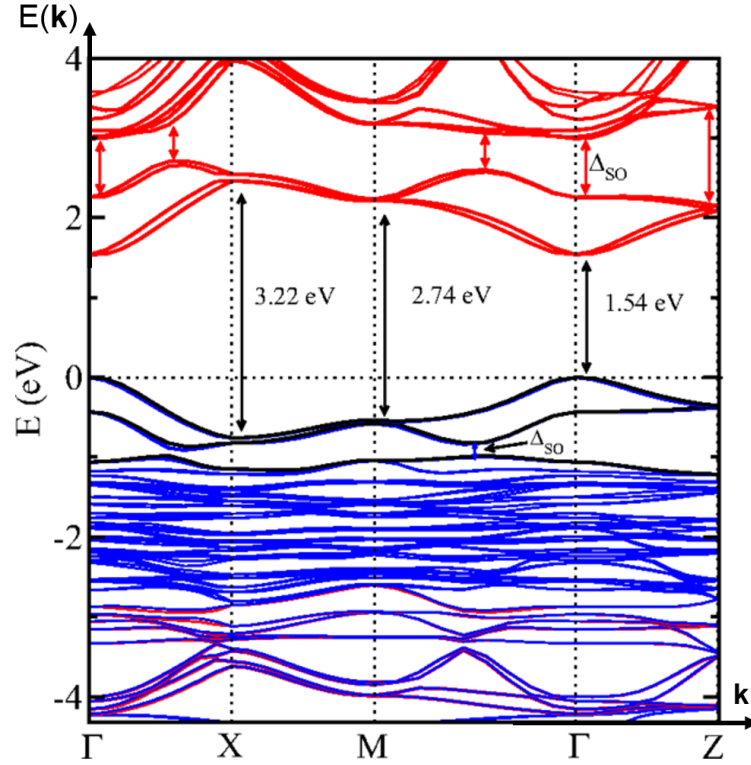
Figure 2.8.: Band structure of the tetragonal phase of MAPbI$_3$. The bands are color coded according to their orbital character, red depicts the Pb-p, black the Pb-s and blue the I-p orbitals. The red arrows indicate the SOC splitting in the conduction band, blue arrows in the valence band and indicate where the bands would be degenerate without the SOC. Due to the Rashba-splitting, the band minima at the Γ-point consist of two bands, which are slightly separated in the k-space. Adapted with permission from Demchenko *et al.*, Phys. Rev. B 94, 075206 (2016). Copyright 2016 American Physical Society.

The maximum of the valence band was found to be ring-shaped (oriented in the k$_x$, y-plane) rather than to be a point. [Nie17] The splitting of the bands, especially close to the band minima was observed indirectly via temperature-dependent time-resolved microwave conductivity measurements (indicating an energetic splitting of $\sim$ 50 meV between the direct and the indirect band gap) for MAPbI$_3$ [Hut17], which was verified by measurements by Niesner *et al.* [Nie17] A direct measurement of the Rashba-splitting using angle-resolved photoelectron spectroscopy of MAPbBr$_3$ in the orthorhombic phase suggests a energy difference of 160 meV. [Nie16b] The Rasbha-effect was suggested to be a possible origin of the exceptionally low electron-hole recombination in lead-halide perovskites. [deQ16a, Str17, CB17] It was proposed that the absorption of light is not affected of the Rashba-splitting as the energetic difference between the direct and indirect band gap is rather small. [Hut17] For the recombination of charge carriers it might play a

bigger role as the fundamental band gap becomes indirect. Another possible explanation for the low recombination rates is the predicted formation of polarons, which would slow down the recombination due to the local interaction of the lattice and the charge carrier (see chapter 4 for more details). [Zhu15b] The electronic structure itself could also be the explanation for low recombination rates due to the intrinsic defect tolerance. Trap states in $MAPbI_3$ (iodine interstitials and vacancies, MA vacancies) are mostly of shallow nature, i.e. located closely to the band edges. It was reported that the band structure does not change even for a moderate non-stoichiometric lead-iodide ratio due to the self-compensation of point defects (traps) and due to the light-induced annihilation of defects. [Yam15, Mos16, Str17, Ste16] The iodine-based defects have low formation energy and are highly mobile, which is positive in terms of defect tolerance but is also an intrinsic source of significant non-radiative recombination. The non-radiative recombination ultimately limits the performance of lead-halide perovskite devices. This performance limitation can e.g. be observed by the non-unity internal photoluminescence quantum yield (PLQY) (ratio between incident to re-emitted photons) even for single crystals. [deQ16b, deQ16a, Str17] Under the influence of an external field or under illumination, these defects migrate to the interfaces of the perovskite film. Ion migration is commonly assigned as the origin of the hysteresis of current-voltage-measurements, which is commonly observed when the scans from V_{OC} to J_{SC} are compared to the scan from J_{SC} to V_{OC}. [Sna14]. Maximum power point tracking (keeping the voltage permanently at the highest power output of the solar power) can be used to measure the actual, stabilized performance of the solar cell. The intrinsic instability due to the ion migration remains a major challenge in terms of device stability. [CB17] Another limitation arises from phase-instability and phase separation of the use cation/anion combinations. While the first solar cells used $MAPbI_3$ or $MAPbI_3(Cl)$ as absorber materials, state of the art devices use a combination of $FAPbI_3$ (to increase the J_{SC}) and $MAPbBr_3$ (to increase the V_{OC}) and additional cations such as Cs or Rb to maximize the performance. [CB17] Without the addition of the inorganic cations, $FAPbI_3$ shows a second-order phase transition of the non-perovskite phase of $FAPbI_3$. Due to the low formation energy of halide interstitials and vacancies and the thermodynamically-favored phase separation, domains with primary iodide- and bromine-based perovskites form and reduce the beneficial effect of the halide combination. Due to lattice management as a result of the smaller inorganic cations, triple- or quadruple-cation perovskite show neither the phase instability of the $FAPbI_3$ nor the halide phase segregation. [CB17] For perovskite solar cells with an stabilized efficiency of above 20%, two device architectures have been reported: a distributed heterojunction (usually with an electron-transport layer) with an additional capping layer of perovskite and a planar heterojunction (illustrated in the left panel of figure 2.9). In contrast to the model of the well-defined p-n-junction, the operating mechanism of lead-halide perovskite solar cell is

more complicated as controlled doping was not successfully achieved yet. For the sake of comparison, a perovskite layer sandwiched between two charge-selective contacts (charge selectivity is obtained by choosing materials with appropriate band alignment for electron or hole extraction) is best approximated with a p-i-n junction. After the absorption of a photon with an energy above the band gap of ~ 1.6 eV for MAPbI$_3$, excitons (correlated electron-hole pairs) are formed and split subsequently. The transport of the then free carrier in the perovskite layer is diffusion-limited. [Her16b, Ric16] Once a carrier reaches the energetically preferred interface, the carrier is extracted due to the electric field in the depletion zone and drifts through the selective transport layer to the contact, where it is extracted.
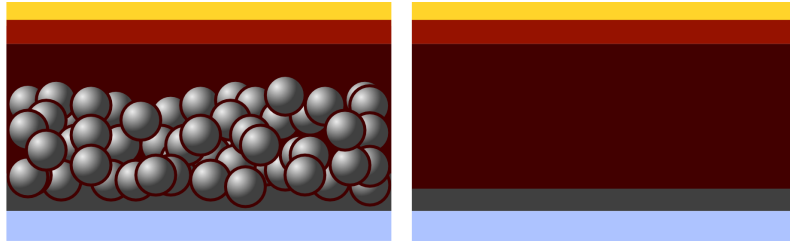

Figure 2.9.: Scheme of the two most commonly used device architectures, left the distributed heterojunction, right the planar heterojunction. Both architectures employ a glass substrate with a transparent conducting oxide (TCO) on top (shown in light blue) and a gold top contact. Charge selectivity is obtained by a compact electron-selective (gray) in between the perovskite layer (brown) and the TCO and hole-selective layer (red) on top of the perovskite layer. In case of the distributed heterojunction, an additional mesoporous layer of the electron-selective layer in which perovskite is infiltrated, whereas the planar heterojunction lacks this mesoporous layer. Adapted from [Bre13]

Two major challenges have been identified in order to bring the long time stabilized efficiency above 20 %: long-term-stability and enhancing of the V$_{OC}$ towards the radiative limit:

- While the J$_{SC}$ is close to the theoretical maximum, the V$_{OC}$ can still be improved; evident by the low external PLQY. The maximum V$_{OC}$ can be estimated by the thermodynamic highest feasible (see SQ-limit) V$_{OC}^{max}$ and the external quantum efficiency of the LED (in principle equivalent to a solar cell, except that charges are injected in order to generate light rather than vice-versa) η_{LED}. The open-circuit voltage reads: V$_{OC} = V_{OC}^{max} - k_B T/e|\ln[\eta_{LED}]|$. [Str17] For a reported η_{LED} of $\sim$ 0.04, which result in a max. V$_{OC}$ of 1.36 V (of which 1.24 V has been obtained to date). [Sal16] A high radiative lifetime in combination with a high external PLQY (> 0.4) was achieved by passivation of the perovskite layer. [deQ16a, Bre17a]

- In addition to the optimization of the perovskite itself, recombination at the interface to the selective contact is also responsible for the limited V_{OC}. In case of the usage of common organic hole conductors, it has been found that non-radiative recombination is enhanced due to unbalanced charge extraction at the perovskite hole-conductor interface, requiring different hole-conducting materials which do not rely on doping to achieve high V_{OC} (see below). [Ber14, Sto17] An additional tunneling layer in between the perovskite and the selective contacts was also found to be beneficial in order to increase both the V_{OC} and the stability of the device. [Sto17, Wan16]

- The stability under working conditions is currently the biggest challenge among perovskite devices. Standard selective contacts, like TiO_2 or Spiro-OMeTAD, require multiple dopants to utilize their fully potential and are unstable under working conditions (internal electric fields, elevated temperatures, UV radiation). [CB17] For the electron-transport layer, $La:BaSnO_3$ (also a perovskite) or self-assembled monolayer of C_{60} were used to enhance the stability while keeping efficiencies high. [Hou17, Shi17b] For the hole-conducting layer, inorganic CuSCN or the small molecule PTAA, which do not require any doping and show good long-term stability were utilized. [Aro17, Sto17] In order to reduce the impact of ion-migration, iodide has been introduced in the precursor solution, resulting in increased V_{OC} and enhanced PLQY, and reaching the highest published efficiency of 22.1%. [Yan17a]

2.4. Ultrafast lasers and nonlinear optics

2.4.1. Pulse propagation

The investigation of the charge generation, thermalization and recombination in lead-iodide perovskites requires laser pulses, which are short in comparison to the investigated phenomena, i.e. generally occur on sub-picosecond (ps) timescales. These timescale are beyond the technical capabilities even of the best electronics. Instead, specific types of lasers are used, some with a large gain bandwidth in order to generate pulses in the low femtosecond (fs) range. In order to derive the fundamentals leading to the formation of short pulses, a closer look at the propagation of electromagnetic waves, nonlinear optics and dispersion is required.

Starting from the relevant Maxwell equations, which read $\nabla \times \mathbf{E} = -\partial \mathbf{B}/\partial t$ and $\nabla \cdot \mathbf{E} = \rho/\varepsilon_0$, the material equation $\mathbf{D} = \varepsilon_0 \mathbf{E} + \mathbf{P}$ one obtains the linear wave equation $\Delta \mathbf{E} - (c^{-2}\,\partial \mathbf{E}/\partial t^2) = 0$, where c is the speed of light, $\boldsymbol{E}$ the electric field vector, $\boldsymbol{P}$ the

polarization and ε_0 the dielectric constant. We can rewrite the linear wave equation to:

$$\Delta \mathbf{E} - \frac{1}{c^2}\frac{\partial^2}{\partial t^2}\mathbf{E} = -\mu_0 \frac{\partial^2}{\partial t^2}\mathbf{P}$$

In order to access the nonlinear case, we Taylor-expand the polarization $\boldsymbol{P}$, which is connected with the electric field $\boldsymbol{E}$ via the electric susceptibility as follows:

$$\mathbf{P} = \varepsilon_0 \sum_i \chi^{(i)}\mathbf{E}^i \tag{2.8}$$

$$= \varepsilon_0 \left[\chi^{(1)}_{ij}\mathbf{E}_j + \chi^{(2)}_{ijk}\mathbf{E}_j\mathbf{E}_k + \chi^{(3)}_{ijkl}\mathbf{E}_j\mathbf{E}_k\mathbf{E}_l + ... \right], \tag{2.9}$$

where $\chi^{(i)}$ is a tensor of rank i+1. The first-order susceptibility $\chi^{(1)}$ is connected to the linear refractive index n via $n = \sqrt{1 + \chi^{(1)}}$. Utilizing the separation of the polarization in components linear to the electric field and the nonlinear terms, can rewrite the wave equation:

$$\Delta \mathbf{E} - \frac{1}{c^2}\frac{\partial^2}{\partial t^2}\mathbf{E} = -\mu_0 \left(\frac{\partial^2}{\partial t^2}\mathbf{P}_l + \frac{\partial^2}{\partial t^2}\mathbf{P}_{nl} \right), \tag{2.10}$$

where $\mathbf{P}_l$ is the linear polarization (the medium response i.e. for refraction, diffraction or dispersion) and $\mathbf{P}_{nl}$ the nonlinear polarization, which consists of the non-linear terms of the polarization introduced in formula 2.8. The right side of equation 2.10 acts as source-term of waves in linear and nonlinear optics. [Boy08, Die06]

2.4.2. Ultrashort pulses

An ultrashort laser pulse is ideally explained with a time-dependent electric field consisting of a linear wave (propagating in z-direction and electric field perpendicular to the propagation direction) and a time-dependent envelope function, A(t):

$$E(t) = A(t)e^{i(\varphi_0(t)+\omega_c t)}. \tag{2.11}$$

Here ω_c is the central frequency and $\varphi_0(t)$ the carrier envelope phase (phase difference between the electric field centered at the peak of A(t) and the actual peak of the electric field modulated with A(t)), schematically shown in figure 2.10. The frequency width of the laser pulse and the corresponding pulse duration are coupled via the Heisenberg uncertainty principles, stating that $\hbar/2 \leq \Delta E \Delta t$. For a Gaussian pulse the time-bandwidth product is $\Delta\nu\Delta t \simeq 0.44$. [Kel17] For a transform-limited pulse, i.e. with $\Delta\nu\Delta t = 0.44$, from a Ti:sapphire laser ($\nu_c = 374$ THz) with a 1 ps pulse, the frequency bandwidth (FWHM) is 0.44 THz, for a 4 fs pulse (representing a single cycle of visible light) 110

THz. So far, we have assumed that the phase of the laser pulse in equation 2.11 depends only on time, but generally speaking the phase is also dependent on the frequency, originating in the frequency dependence of the dielectric function $\varepsilon(\omega)$: $\varphi_0(\omega, t)$.
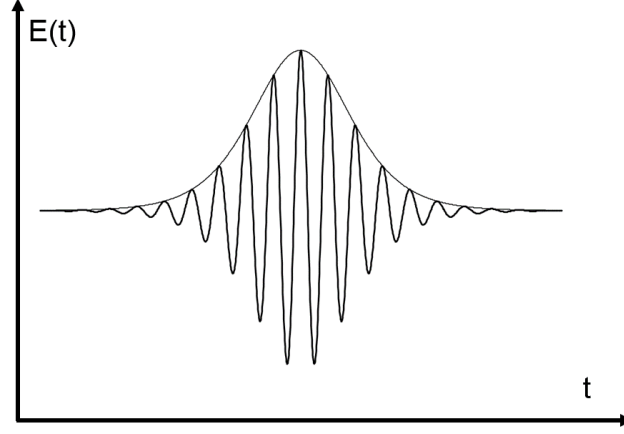

Figure 2.10.: Scheme of an ultrafast laser pulse, where the amplitude of electric field follows the envelope function. Here, $\varphi_0(t) = 0$ as the maximum of the electric field is centered at the maximum of the envelope function. Adapted from [Bre10].

To account for the frequency-dependence of the phase, we Taylor-expand the phase around the central frequency ω_c:

$$\varphi(\omega) = \varphi_0 + (\omega - \omega_0)\left(\frac{d\varphi(\omega)}{d\omega}\right)_{\omega=\omega_0} + \frac{1}{2!}(\omega - \omega_0)^2\left(\frac{d^2\varphi(\omega)}{d\omega^2}\right)_{\omega=\omega_0}$$

$$+ \frac{1}{3!}(\omega - \omega_0)^3\left(\frac{d^3\varphi(\omega)}{d\omega^3}\right)_{\omega=\omega_0} + \cdots$$

The first term φ_0 describes the absolute phase offset to ω_0, $\left(\frac{d\varphi(\omega)}{d\omega}\right)_{\omega=\omega_0}$ the group delay (frequency-dependent delay of the phase). The second order term $\left(\frac{d^2\varphi(\omega)}{d\omega^2}\right)_{\omega=\omega_0}$ represents the group delay dispersion (GDD), resulting in a frequency-dependent group delay. For GDD > 0, one speaks of positive (normal) dispersion (i.e. blue trailing red), for GDD < 0 of negative (anomalous) dispersion (red trailing blue). The two different dispersion regimes are illustrated in figure 2.11. When a transform-limited pulse travels through an optical element with a group delay dispersion $\neq 0$, different spectral components will travel with different propagation velocities, which results in temporal stretching of the pulse (also called a *chirped* pulse). In order to account for the different propagation velocities and to generate transform-limited pulses, dispersion management is required.

The chirp can be reduced with geometrical-arranged prism or grating pair, which is set in a way that (in case of normal dispersion) the blue travel a shorter way in space compared to red in order to compress the pulse towards the transform-limit. For pulses shorter than 100 fs, not only the second-order terms are important but also the higher terms of the Taylor expansion, especially the third-order dispersion (TOD). If $\left(\frac{d^3\varphi(\omega)}{d\omega^3}\right)_{\omega=\omega_0} > \tau_p^3$, where τ_p is the pulse duration, compensation of the TOD is required as well. [Kel17].
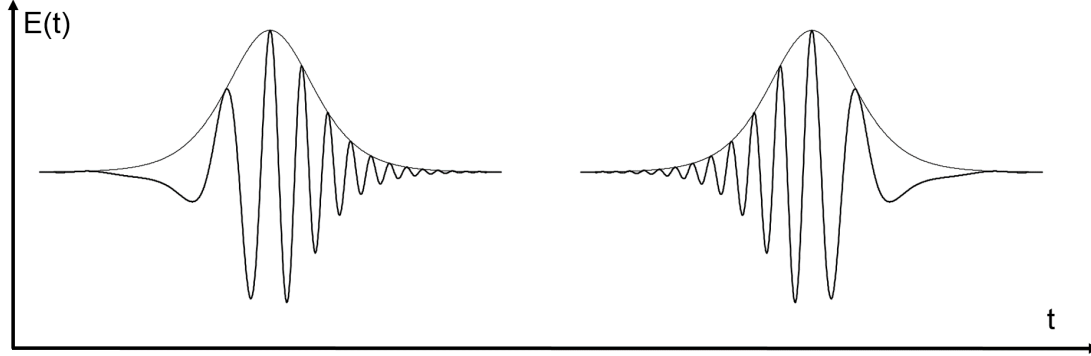

Figure 2.11.: Scheme of an positive and negative dispersed laser pulses. In the left pulse, the low frequencies trail the high frequencies, therefore it is negatively dispersed. In the right pulse, the high frequencies trail the low ones, representing positive dispersion. Adapted from [Bre10].

2.4.3. Modelocking

In order to achieve lasing, a gain medium, which allows population inversion and a resonator are required. A resonator with a defined length L allows a standing wave only for certain frequencies, called *resonator modes*. The frequency separation of the longitudinal resonator modes is $\Delta\nu = c/2L$ and corresponding spacing in the time domain $\Delta t = L/c$. Depending on the gain bandwidth of the laser crystal and resonator configuration, either a single mode or multiple modes can be supported. [Kel17] The electric field of coupled modes can be described as follows:

$$E(t) \sim E_0(t)\frac{\sin\left(m\pi t/\Delta t\right)}{\sin\left(\pi t/\Delta t\right)},$$

where m is the number of coupled modes. [Die06, Kel17] For $m = 1$, one achieves a wave with single frequency, i.e. cw-operation (continuous wave).
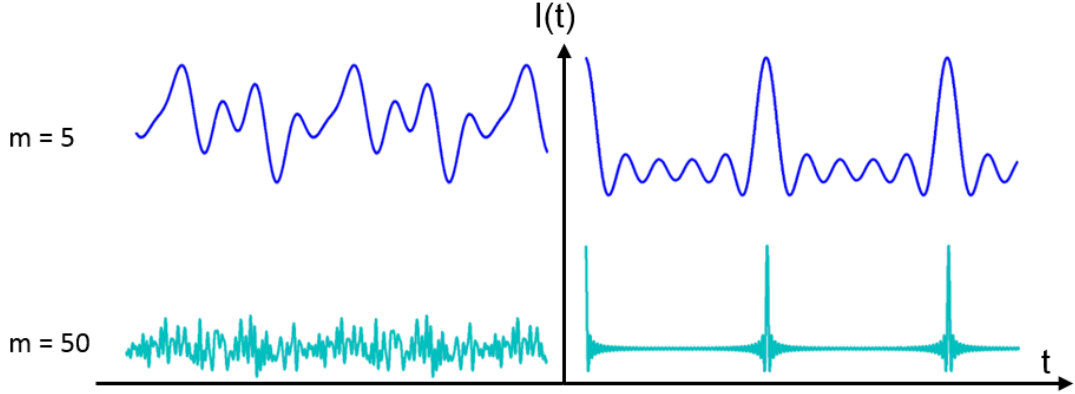
Figure 2.12.: Schematic visualization of unlocked (left) and locked modes (right) for m = 5 (top) or m = 50 (bottom). Adapted with permission from [Etz14].

If the resonator and the gain medium support a large number of modes, the output in the case of non-coupled modes will initially be noise due to lacking phase relation of the individual modes, but for coupled or locked modes, the output will consist of short pulses (see figure 2.12). [Kel17] Femtosecond pulses require fast modelocking beyond the capability of electronic circuits (active mode-locking), which is why passive mode-locking is utilized. Passive mode-locking uses a saturable absorber or, in the case of a Ti:sapphire laser, an intensity-dependent self-focus-effect called Kerr-lens. The Kerr lens is based on a nonlinear effect, self-focusing (origination from the Kerr effect, where the refractive index becomes intensity dependent: $n = n_0 + n_2 I(t)$). If the Kerr lens is combined with an aperture, which blocks the low-intensity fraction of the propagating modes, an intensity-dependent switch is created. Only the high-intensity modes are focused due to the Kerr-effect and pass the switch. Due to the diffraction induced by an aperture, the intensity dependent switch is realized with a spatially inhomogeneous overlap of the pump and laser beam in the laser crystal. [Kel17]

2.4.4. Nonlinear frequency conversion

In order access wavelengths beyond the fundamental wavelength of the laser system, two processes are important: supercontinuum generation and optical parametric amplification. Both nonlinear processes require high power, usually provided by chirped-pulse amplification of the laser pulse. In order to prevent strong nonlinear processes during the amplification, the laser pulse is initially stretched to reduce the peak power ($P_p \sim 1/\tau_p$). After amplification of the pulse, the stretched pulse is compressed using e.g. a grating compressor to a similar or shorter pulse length than the initial pulse.

For the second-order nonlinear process, which involves the nonlinear polarization $P_i^{NL} = \varepsilon_0 \chi_{i,j,k}^{(2)}$ (see equation 2.8), two interacting electric fields are involved, E_j and E_k with frequencies ω_j and ω_k. The nonlinear polarization (equation 2.10) acts as a source-term of radiation, gives rise to a number of effects, such as the second-harmonic generation ($\omega = 2\omega_{j,k}$), sum-frequency generation ($\omega = \omega_j + \omega_j$), difference-frequency generation ($\omega = \omega_j - \omega_j$) and optical rectification (quasi DC/low-frequency: $\omega_{l=j,k} = \omega_l - \omega_l = 0$). For optical parametric processes, a special (inverse) case of the sum-frequency generation, a high power pump beam with the frequency ω_p and a low power signal beam with a frequency of ω_s are mixed in a nonlinear crystal, where the signal beam is parametrically amplified and the idler beam with frequency ω_i is generated. The signal beam is a spectral fraction of a supercontinuum generated before the parametric amplification. For parametric processes, energy and momentum need to be conversed (phase-matching condition).

$$\hbar\omega_p = \hbar\omega_s + \hbar\omega_p \quad \text{with} \quad \omega_p > \omega_s \geq \omega_i \quad \text{and}$$
$$\hbar\mathbf{k}_p = \hbar\mathbf{k}_s + \hbar\mathbf{k}_p.$$

Here $\mathbf{k}_p$, $\mathbf{k}_s$ and $\mathbf{k}_i$ are the wave vectors of the pump-, signal- and idler-beam. The phase matching condition $\Delta k = 0$ cannot be fulfilled in an isotropic crystal with normal dispersion ($k = \omega n(\omega)$), which is why birefringent crystal are used to achieve phase matching. In birefringent crystals the ordinary (polarization perpendicular to the optical axis) refractive index n_o can be larger than the extraordinary (polarization in the direction of the optical axis) refractive index n_e, thus the phase matching condition can be fulfilled. Phase-matching is achieved via adjustment of the angle between $\boldsymbol{k}$ and the optical axis of the birefringent crystal. [Cer03] For short pulses, an additional limitation arises of the different chirp acquired in the crystal, often limiting the feasible length of the nonlinear crystal.

For the generation of a supercontinuum, an intense laser pulse is focused in a nonlinear crystal and a supercontinuum is generated due to the self-phase modulation. For a short laser pulse with high intensity, the nonlinear refractive index ($n_2 = (2\pi/n_0)^2 \chi^{(3)}(\omega; \omega, \omega, -\omega)$, where $\chi^{(3)}$ is the third-order nonlinear susceptibility) results in an additional phase shift (so called self-phase modulation, SPM), which can be described as: $\Delta\varphi = \omega/c n_2 I(t) L$, where L is the interaction distance of the laser in the nonlinear medium. From the SPM, we can calculate the spectral broadening:

$$\Delta\omega(t) = \frac{\omega}{c} n_2 L \frac{\partial I}{\partial t}. \tag{2.12}$$

Due to the derivative of the intensity, the leading and trailing parts of the pulse will generate additional frequencies, in one case at higher frequencies compared to the central frequency (blue side of the spectrum) and in the other case at the lower frequencies (red side of the spectrum). The self-phase modulation is enhanced due to the Kerr-effect induced self-focusing of the laser pulse. The generation of a supercontinuum is ultimately limited by self-focusing. The self-focusing does lead to a break-up of the laser pulse in multiple filaments, which is coupled to damage of the crystal due multi-photon absorption and the local generation of a plasma. [Die06]

2.5. Charge generation and recombination in lead-iodide perovskites

The photophysical processes after the generation of charge carriers can be separated in two groups of processes: the initial relaxation and the recombination on a timescale of a few femto-/picoseconds and nano- to microseconds, respectively.

The absorption of above band-gap photons results in the generation of correlated electron hole pairs. Theoretical calculations indicate the highest transition probabilities around Γ- and M-point (see figure 2.8) and slightly lower transition probabilities from lower-energetic band in comparison to the valence band maximum (VBM) and to band higher-energetic than the conduction band minimum (CBM) [Eve14, Kaw15, Her16b]. Due to the low exciton binding energy ($E_B \leq k_B T$), free carriers are the intrinsic charge carriers at room temperature, although weakly bound Wannier-Mott excitons can be observed on a sub-ps timescale or at low temperatures. An estimation for the splitting time of excitons to free carrier at ambient conditions was reported by Ghosh *et al.* with ~ 20 fs. [Gho17, Her16b] For non-resonant excitation, i.e. for carrier generated off the band minima, the carriers will form a non-thermal distribution. The non-thermal distribution undergoes thermalization into a Maxwell-Boltzmann distribution in $t < 100$ fs predominantly due to carrier-carrier scattering. [Her16b, Ric17] Once the carrier are thermalized, they can be described with an effective carrier temperature T_c, which can reach up to 2000 K before cooling to the lattice temperature T_l. [Yan15] If T_c is higher than T_l, one speaks about *hot* carriers. The cooling of hot carriers in $CH_3NH_3PbI_3$ is a prime example of the polar-optical phonon interaction (also called Fröhlich-interaction). Due to the polar nature of the lattice, the Fröhlich-interaction between the photogenerated charge carriers and the lead-iodide sub-lattice is the dominant carrier-phonon-interaction on a ps timescale. The cooling of carriers can be separated in two different regimes: within the first ps, the majority of the carrier cools through LO-phonon emission (see also chapter 4), presumably in the $\Gamma-$valley. [Yan15] Specifically, the Fröhlich-interaction is due to the

Coulomb interaction between electron and out-of-phase displacement of the lead-iodide system induced by LO-phonon. Another fraction of carriers cools slower, in the order of a few tens to hundred ps. The mechanism depends on the carrier density: for low carrier density ($\leq 5 \cdot 10^{17}/cm^3$), a small fraction of the total carriers (in the order of a few percent, see section 5.1) cools within ~ 100 ps and reaches the band edges. The long excited state lifetimes originate most likely from slow cooling of carriers at the M-point (combination of large momentum mismatch and energy difference). Alternative explanations include carrier population present in a valence/conduction bands around the Γ-point, which require an intraband transition to cool to the band edges or from a reduced density of states 0.3 eV above the band minima. [Bre17b, Cha16, Nie16c, Dem16]
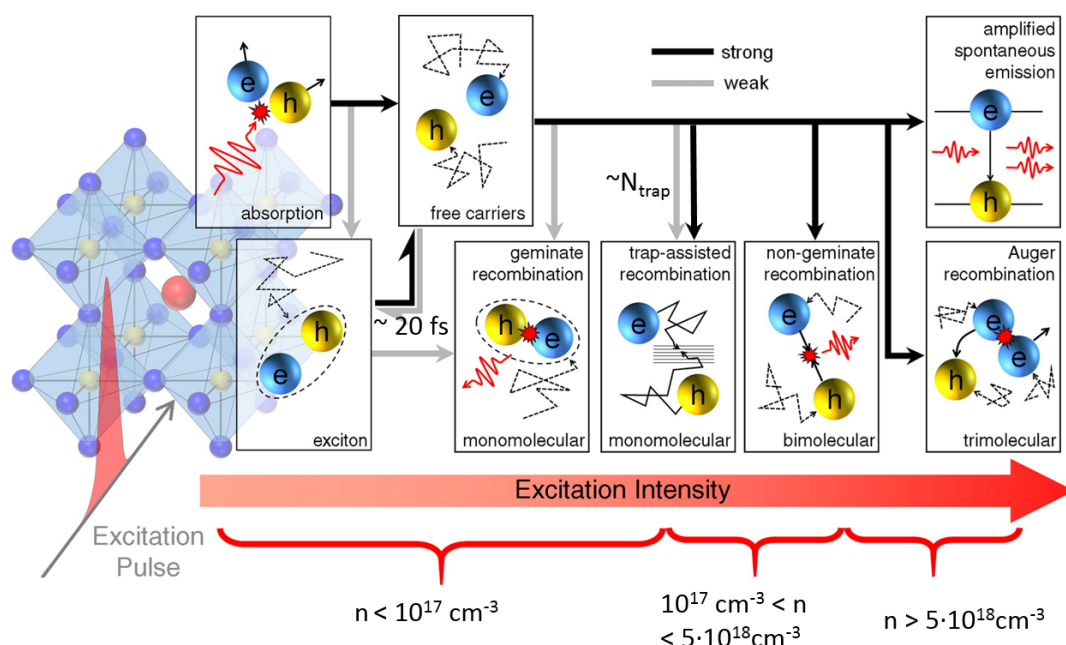

Figure 2.13.: Schematic overview of the photophysical processes related to the generation and recombination of charge carriers in $CH_3NH_3PbI_3$. The carrier density n is relevant for the fraction of excitons and free carriers after the generation of charges and for the type of recombination. Adapted with permission from Acc. Chem. Res., 2016, 49 (2), pp 294-302, Copyright (2017) American Chemical society.

For high charge carrier densities ($\geq 5 \cdot 10^{17}/cm^3$), the slow cooling originates from a hot phonon bottleneck. Due to the high carrier and LO-phonon (due to the carrier cooling) densities in combination with an effective suppression of the decay of optical into acoustic

phonons[5], the energy cannot be thermalized to the lattice. Subsequently, LO-phonons reheat charge carriers, thus slowing down the cooling. [Pri15, Yan15, Fu17] Another contribution to the slow cooling arises from carrier-phonon-interaction: Auger-heating. Here, the excess energy resulting from the recombination of an electron-hole pair is non-radiatively transferred to a third charge carrier. The third carrier undergoes intraband excitation due to the absorption of LO-phonons, which slows the cooling of hot carriers even further. [Fu17] Subsequent or in parallel to the carrier cooling, the formation of polarons has been proposed (see also chapter 4). Briefly, a charge carrier polarizes the lattice around it, which results in a larger effective mass and reduced scattering with optical phonons, which is one hypothesis to explain the long hot and cooled carrier lifetimes.

Subsequently to the cooling of carriers, charge carriers recombine (see figure 2.13). For lead-iodide perovskites, there are three different regimes of carrier recombination which depend on the initial carrier density:

- At low carrier density ($n < 10^{17}/cm^3$), trap-assisted recombination dominates, i.e. a charge carrier is trapped and recombines either non-radiatively or is annihilated by a charge carrier of the opposite kind. The radiative trap-assisted recombination occurs with a relatively long timescale (ns - μs) as the charge carrier is localized in the trap and requires the opposite charge to be in the vicinity of the trap in order to recombine, which is less probable at low charge carrier densities. Whether trap-assisted recombination can be observed is highly dependent on the trap density of the perovskite, which is related to the preparation (see also chapter 6). In the experiment, trap-assisted recombination can be identified from a linear decay of the luminescence intensity in a semilog plot.

- For an intermediate carrier density ($10^{17}/cm^3 \leq n < 5 \cdot 10^{18}/cm^3$), bimolecular recombination occurs, i.e. the recombination of (uncorrelated) free charge carriers. The bimolecular recombination rate is exceptionally low. In addition to the previously mentioned mechanisms (polaron formation, indirect character of the band gap), preferential location of electrons and holes in different regions of the perovskite unit cell was also proposed as a consequence of the composition of the band minima. [Her16b, Amb18] In the experiment, bimolecular recombination can be identified from a quadratic decay of the luminescence intensity in a semilog plot.

- For high charge carrier densities ($n \geq 5 \cdot 10^{18}/cm^3$), Auger recombination (three-particle-interaction; transfer of the recombination energy to a third carrier under conversation of energy and momentum) is the dominant recombination mechanism.

---

[5]Multiple mechanism were proposed in order to explain the suppressed decay of the optical into acoustical phonons, for more details publication [Fu17] is referred, the ultralow thermal conductivity does certainly play an important role as well. [Pis14]

Similar to the bimolecular, the Auger recombination can be identified from a non-linear decay of the luminescence intensity in a semilog plot, however in contrast to bimolecular recombination but only within the first few nanoseconds.

2.6. Time-resolved THz spectroscopy

In order to study not only optical (interband) transitions and coupled effects, e.g. carrier generation and recombination, but also the material properties in relation to charge carriers, such as the mobility, charged quasi-particles such as polarons or phonons themselves, electromagnetic waves in the frequency region of a few to 100 meV are required. This spectral region is characterized by frequencies of the electromagnetic field that lay in the THz range (0.1 to 100 THz, 0.4 to 40 meV, 3 mm to 3 μm wavelength, 4.64K to 464K). THz radiation also provides a measurement of the photoconductivity of a semiconductor/metal in a contact-free manner. [Ulb11] As mentioned in section 2.4.4, optical rectification is a second-order nonlinear effect, which is one way to generate electric fields in the THz-region. In order for the first term of the nonlinear polarization to be non-zero, $\chi^{(2)}$ cannot be zero which excludes inversion-symmetric materials as a choice for optical rectification. Non inversion-symmetric materials, such as Zinc telluride (ZnTe) or Gallium phosphide (GaP), are commonly used. [Kel17] A good visualization of the optical rectification is difference-frequency generation between the different frequency components contained within the bandwidth of a short laser pulse. The achievable bandwidth of the rectified pulse is therefore directly correlated to the properties of the generating pulse. The far field of the rectified pulse or the electromagnetic THz-pulse, which is later used for the THz spectroscopy can be derived via the second time-derivative of the polarization: $\mathrm{E_{THz}} \sim \partial^2 P(t)/\partial t^2$. [Kel17]

As for the parametric processes, phase-matching is important but satisfied for GaP and ZnTe when excited at 800 nm due to the equivalence of group velocity of the generating pulse and the phase velocity of the THz-pulse. [Kel17, Ulb11] For detection of the THz pulse, electro-optical sampling which is based on the Pockels-effect, can be used. The Pockels effect describes the electric-field induced birefringence in a material. For the case of the detection of THz pulse, this field is the THz-field itself. The electro-optical sampling combines the THz-induced Pockels effect with an additional laser pulse of which the polarization is rotated. This approach provides a measurement both the phase and the amplitude of the THz-field instead of only the intensity. The measurement of the electric field allows to reconstruct the complex dielectric function $\varepsilon(\omega) = \varepsilon_1(\omega) + i\varepsilon_2(\omega)$ (ε_1: phase shift and ε_2 : amplitude change due to absorption or gain, see figure 3.8). From the dielectric function, the complex refractive index $\mathrm{n}(\omega) \simeq \sqrt{\varepsilon(\omega)}$ and the conductivity $\sigma(\omega) \simeq -i\varepsilon_0\varepsilon(\omega)$ can be derived. The complex dielectric function and related quantities

(conductivity, refractive index) can be extracted from the pump-induced change of the electric field $\Delta E(t_p, \omega)$ compared to the reference measurement (unpumped sample) and subsequent Fourier-transformation of the electric fields.

The time-resolution of the electro-optical sampling is experimentally limited by the pulse duration of the probe pulse and is usually achieved by sampling the probe pulse with respect to the THz field. [Ulb11]
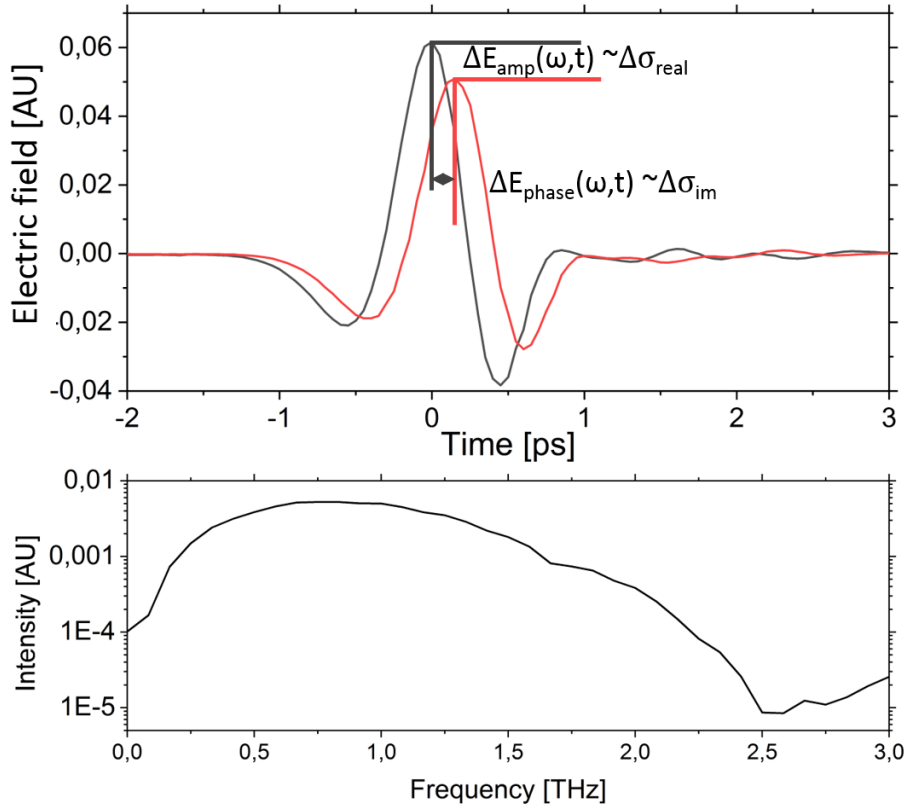

Figure 2.14.: The electric field of a THz-pulse before (black) and after interaction with a semiconductor (red) is shown in the upper panel. Due to the interaction with the semiconductor, an the amplitude- ($\Delta E_{\mathrm{amp}}(\omega, t)$) and phase offset ($\Delta E_{\mathrm{phase}}(\omega, t)$) can be observed. $\Delta E_{\mathrm{amp}}(\omega, t)$ is related to the change of the real component of the photoconductivity, $\Delta\sigma_{\mathrm{real}}$, $\Delta E_{\mathrm{phase}}(\omega, t)$ to the change of the imaginary component of the photoconductivity, $\Delta\sigma_{\mathrm{im}}$. The spectrum of the unperturbed pulse (black) is shown in the lower panel, obtained by fast Fourier transformation.

Under the assumption that the layer of material under study is much thinner than the wavelength of the terahertz pulse ($d \ll \lambda$, thin-film approximation) and weak excitation

(so carrier-carrier interaction can be mostly neglected), the ratio of the electric field of an excited ($E_p(t_p, \omega) = E_{\text{ref}}(\omega) + \Delta E(t_p, \omega)$) and unexcited sample ($E_{\text{ref}}(\omega)$) provides the means to calculate the frequency-resolved photoconductivity of the sample. The ratio can be calculated via the Fresnel coefficients (transmission/reflection of a multi-layer system, at least of (non-conductive) substrate and sample):

$$\frac{E_p(t_p, \omega)}{E_p(t_p, \omega) - \Delta E(t_p, \omega)} = \frac{n+1}{n+1+Z_0 \, d \, \sigma_p(t_p, \omega)}, \tag{2.13}$$

where Z_0 is the impedance of the free space (377 Ω), n the index of refraction of the substrate in the THz region.[6] Equation 2.13 is valid under the assumption that the sample is measured in air/vacuum. [Ulb11, Jep11]. The complex photoconductivity can be easily evaluated based on equation 2.13 [Jep11] :

$$\sigma_p(t_p, \omega) = -\frac{n+1}{Z_0 d} \frac{\Delta E(t_p, \omega)}{E_p(t_p, \omega)}.$$

2.6.1. Drude model of conductivity

The mechanism of the photoconductivity can be explained within the framework of the Drude conductivity model, which is based on a semiclassical model of charge transport (inelastic scattering due to carrier-phonon and carrier with a characteristic scattering time τ_s between two scattering event). Under the influence of an electric field E(t), charges follow the equation of motion:

$$\frac{d^2 \boldsymbol{r}}{dt^2} + \Gamma \frac{d \boldsymbol{r}}{dt} = -\frac{e}{m_e^*} \mathbf{E}(t),$$

where $\boldsymbol{r}$ is the ensemble average displacement of the charge carriers and Γ the scattering rate ($1/\tau_s$). The equation of motion can be solved for a given carrier density N for the dielectric function or the so-called Drude-conductivity:

$$\varepsilon_D(\omega) = \varepsilon_\infty - \frac{Ne^2}{\varepsilon_0 m_e^*} \left(\frac{1}{\omega^2 + i\Gamma\omega} \right) \tag{2.14}$$

$$\sigma_D(\omega) = \frac{Ne^2 \tau_s}{m_e^*} \left(\frac{1}{1 - i\omega\tau_s} \right), \tag{2.15}$$

where ε_∞ is the high frequency dielectric constant. The Drude response of the conductivity has a resonance with a bandwidth of Γ and amplitude of $Ne^2/\varepsilon_0 m_e^*$. [Ulb11] For the case of a scattering rate much higher than the THz frequency range, the real component of the photoconductivity will essentially be flat and finite, whereas the imaginary component

---

[6]The equation is also valid for carrier distribution following Beer's law with small error < 5 %.

is negligible (or, equivalently, the dielectric response is purely imaginary in this case). For this case, the scattering time and the charge carrier density cannot be independently determined.

3. Experimental Methods

3.1. Perovskite film deposition

The perovskite films used in this thesis were prepared using spin-coating and subsequent thermal annealing in a glove box (Mecaplex/Glovebox Systemtechnik: $O_2 < 5$ ppm, $H_2O < 1$ ppm or Glovebox Systemtechnik $H_2O < 10$ ppm). Two different approaches were preferentially used:

- Single-step deposition using an anti-solvent, discussed in chapter 4.

- Single step deposition from a dimethylformamide (DMF) solution containing $PbCl_2$ and CH_3NH_3, discussed in section 5.10.

Common polar solvents for the precursor solution are DMF, dimethyl sulfoxide (DMSO) and γ-Butyrolactone (GBL), which dissolve the precursor salts. The precursor salts are from the cations (CH_3NH_3 (MA), $CH(NH_2)_2$ (FA)) and anions (PbI_2, $PbCl_2$, $PbBr_2$). The precursor solutions are dropped on a substrate and spin-coated, where the solvent partially evaporates and the nucleation occurs. After the spin-coating, samples were thermally annealed. During spin-coating, heterogeneous (Volmer-Weber-like) crystallization occurs from nucleation sites, such as the substrate-solution interface or crystalline seeds. [Zhe15b, Pet17] The formed crystallites coalesce during the subsequent annealing to minimize the total surface energy (Ostwald-ripening). [Str15a]

A number of different precursors were used throughout the completion of this thesis and were found to influence the charge carrier recombination and phase segregation quite drastically. As an example, a comparison of different purities of lead-iodide (99 and 99.999 %) purchased from Sigma Aldrich is shown in figure 3.1. Using lead-iodide of higher purity leads to a significant improvement of the photoluminescence lifetime from 1.5 to 12 ns due to reduced impurity-induced trap-density. However, in combination with mixed anions (for both, mixing with $PbBr_2$ and $PbCl_2$, respectively), which were used in order to stabilize the perovskite phase of $FAPbI_3$, phase separation between the perovskite ($MA_{0.8}FA_{0.2}PbI_{3-x}Cl_x$), PbI_2 and the non-perovskite $FAPbI_3$ occurred when high-purity PbI_2 was used, but not for the case of 99 % purity (due to the higher density of precipitation seeds). The purity of the lead-iodide precursor is defined with respect

to other metals rather than different lead-compounds, such as lead-acetate, lead-sulfide, and lead-sulfate.[1] These impurities likely explain the strong variation of the properties of perovskite films in this thesis.
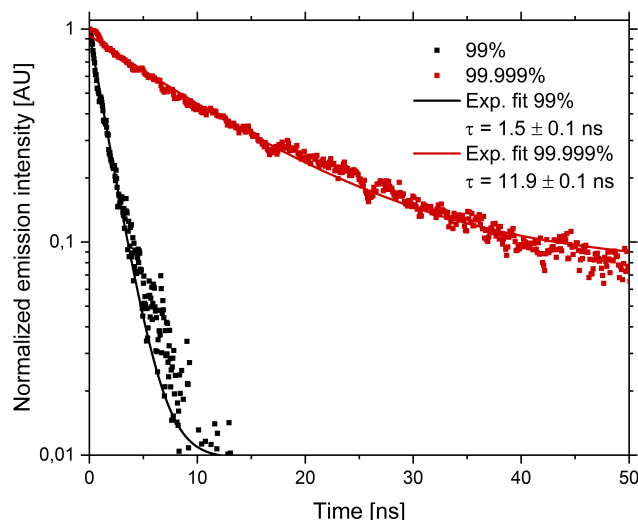

Figure 3.1.: Comparison of the decay of the photoluminescence for $MA_{0.8}FA_{0.2}PbI_3$ perovskite films prepared with 99 and 99.999% lead-iodide. The samples were excited with a 150 fs pulse with a photon energy of 3.1 eV, a repetition rate of 1 kHz and a fluence of 1 $\mu J/cm^2$. The photoluminescence signal of the film prepared with the 99% purity PbI_2 decays on a timescale of less than 10 ns, whereas emission from the perovskite film prepared with 99.999 % PbI_2 decays on a much slower timescale. The lifetimes obtained by fitting the decays to exponential functions are 1.5 and 12 ns, respectively.

3.1.1. Solvent-engineering

For the solvent-engineering deposition, an equimolar solution of cations [CH_3NH_3 (Solaronix, Dyesol) and/or $CH(NH_2)_2$(Dyesol)] and lead-halide anions [PbI_2 (Sigma Aldrich, Alfa Aesar), $PbBr_2$ (Sigma Aldrich, 99.999%) and $PbCl_2$ (Sigma Aldrich, 99.999%)] in anhydrous [DMF, DMSO (Sigma Aldrich)] or regular-grade solvents [GBL, 1-Methyl-2-pyrrolidinone (NMP, Sigma Aldrich)] was prepared under a pure nitrogen atmosphere. Depending on the desired application, either $MAPbI_3$, $FAPbI_3$, $MA_{0.8}FA_{0.2}PbI_3$, $MA_{0.2}FA_{0.8}PbI_3$, $MA_{0.8}FA_{0.2}PbI_{3-x}Cl_x$ or $MA_{0.8}FA_{0.2}PbI_{2.55}Br_{0.45}$ was prepared. The solution was kept on a hotplate at 60 °C until the salts were dissolved and kept at 60 °C

---

[1] Based on the analysis done by Alexander Klasen (MPIP, Mainz), private communication

prior to deposition. The solution (50 μl for 1 cm^2 substrate, 150 μl for 1 inch^2) was dispersed on the substrate from the edges towards the center. The samples were spun for 10 s at 1000 rpm (slow acceleration) and for 30 s at 4000 rpm. After 20 s total spinning time, 100 μl of anhydrous chlorobenzene (CB, Sigma Aldrich) was dropped within a few seconds on the spinning sample. After the spin-coating, the samples were thermally annealed in a nitrogen atmosphere at 100 °C for all the compounds except FAPbI$_3$ and 150 °C for FAPbI$_3$.

The mechanism of the crystallization depends on the used solvents and anti-solvents. For the case of DMF, such as in chapter 4, using CB during the spin-coating will result in a supersaturation of the precursor solution and therefore initiate the crystallization. The time at which the anti-solvent is dropped is critical: if it occurs too early, the layer of solution is still too thick, therefore resulting in isolated large crystals, which do not form a continuous film. If it occurs too late, the crystallization will occur from the DMF-PbI$_2$-network, which results in rod-like structures and therefore also in non-complete surface coverage. [Str15a, Xia14a, Guo15]

For the case of DMSO solution, the anti-solvent induces rapid crystallization of an intermediate MA-PbI$_2$-DMSO-phase. The intermediate phase is much more stable compared to the PbI$_2$-DMF-intermediate due to the complex bond between the DMSO and the PbI$_2$. The formation of this intermediate phase decelerates the crystallization of the perovskite. [Jeo14]

3.1.2. Single-step deposition from PbCl$_2$

The single-step deposition without the usage of an anti-solvent uses a non-stoichiometric solution of 3:1 MAI:PbCl$_2$. The salts are dissolved in anhydrous DMF (40 wt%) and kept at 60 °C prior to deposition. The solution is then dropped on the substrate and spin-coated for 45-60 s at 2000 rpm. After the spin-coating, the samples are kept at room temperature for 30 minutes before annealing at 100 °C for 60 minutes under nitrogen atmosphere. The films show drastically improved photophysical properties in comparison to MAPbI$_3$.[Str13, Bre17b] Since the band gap of the perovskite prepared from MAI and PbCl$_2$ is nearly identical compared to MAPbI$_3$ one speaks of doped MAPbI$_3$, MAPbI$_3$(Cl). Studies show only traces of chloride in the final film, mostly near the substrate-film interface. [Pet17] The determined location of the chloride in the proximity of the substrate leads to the assumption that MAPbCl$_3$ nucleates the crystallization process and acts as a seeding layer/template for the growth of large MAPbI$_3$(Cl) crystals via ion-exchange. The excess MA promotes the growth of large grains and evaporates subsequently as MACl during the annealing. [Wil14, Sak16, Pet17]

3.1.3. Methylamine-treatment

Methylamine (MA, CH_3NH_2) treatment was used as a post-processing procedure to improve the surface coverage of a perovskite film. Two different approaches were used in order to perform the treatment. In the first approach, MA in ethanol (33 wt%, Sigma Aldrich) was filled into a crystallizer under a nitrogen atmosphere. Subsequently, the perovskite film was positioned over the crystallizer within 2 cm from the solution/nitrogen interface. Upon exposure to the MA, the dark perovskite films became colorless. Following the solid-gas interaction, the perovskite film was removed from the top of the crystallizer and exposed to a gentle nitrogen flow until the film turned dark again. The samples were placed on a hotplate at 60 °C for > 15 minutes to ensure complete removal of the MA (evaporation temperature - 6°C). The second method, more sophisticated, involves the usage of a reactor as shown in figure 3.2. Via the two ports on the left side, MA (Linde group, $\geq$99%[2]) and nitrogen with a controlled partial pressure can be delivered into the reactor. Prior to use, the reactor and the tubes were flushed with nitrogen to ensure a humidity-free system. The samples were placed on angled posts, shown beneath the reactor in figure 3.2.
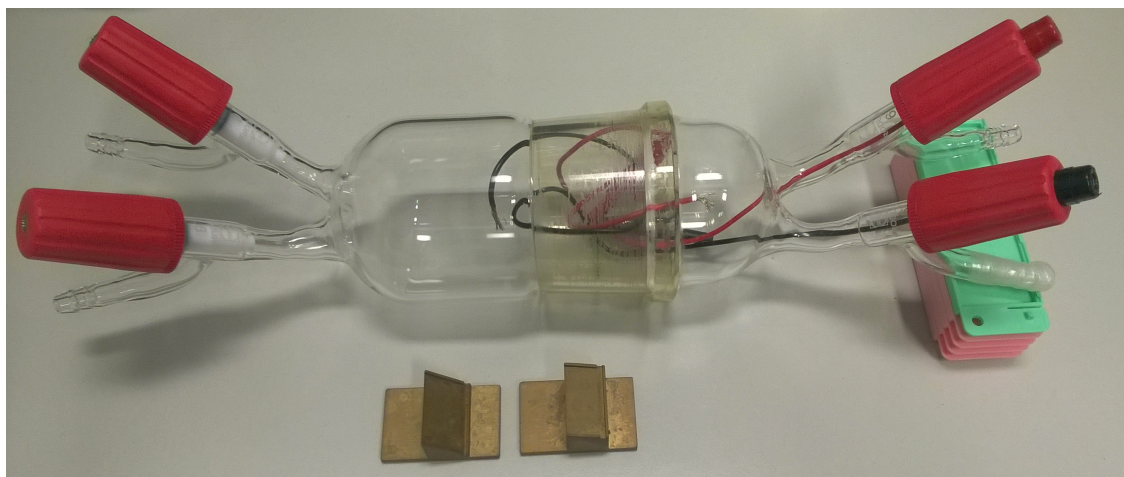

Figure 3.2.: Reaction chamber used for the MA-treatment. In the front of the chamber, the angled posts for the substrates are shown.

Typically, the samples were placed on a holder with an angle of 45° with respect to the horizontal plane and exposed to methylamine for 10 s. The partial pressure and valve opening time were selected in a way that results in a bleaching of the sample in about

---

[2]The purity is defined with respect to different amines, such as $CH_3CH_2NH_2$ or $(CH_3)_2NH$, which have boiling points below room temperature and small enough to allow the uptake into the perovskite. These amines may remain in the perovskite after the treatment and form low-dimensional crystallites (see section **??**) that act as trap states.

1 s. After the exposure, the reactor was flushed with nitrogen for at least 30 s followed by closing all access valves in order to retain the nitrogen atmosphere. For experimental purposes, the angled posts were placed on a Peltier-element, which allowed in-situ cooling and heating between 0 and 95 °C.

3.1.4. Film preparation

Fused silica substrates (Präzisions Glas & Optik GmbH, LG Optical) were cleaned using 2% soap solution in water (Hellmanex), acetone and isopropanol (Sigma Aldrich) for 10 minutes each with subsequent rinsing with the succeeding solvent in an ultrasonic bath (Bandelin Sonorex). After the cleaning, the samples were rinsed with ethanol (Absolut, VWR) and dried with nitrogen. The samples were then plasma-cleaned (Technics Plasma GmbH, 200G) for 20 minutes under 0.2 mbar Ar/O_2 atmosphere with a power of 300 W. The samples were then transferred into a glovebox, where the films were prepared within 15 minutes following the plasma treatment.

3.2. Perovskite film characterization

In order to characterize perovskite films, a number of optical techniques were used. In the context of solution-processed semiconductors, optical characterization tools, including UV/VIS and transient absorption spectroscopy, provide the ability to measure the steady-state and time-resolved properties of lead-iodide perovskite without the need of electrical contacts.

3.2.1. UV-VIS absorption spectroscopy

Absorption measurements ranging from 350 nm to 900 nm were performed using an UV/VIS spectrometer (Perkin-Elmer Lambda 900, scheme shown in figure 3.3) using either a Deuterium or (UV-grade) Tungsten halogen lamp as light source. The absorption was measured using a Peltier-cooled PbS detector (NIR) or a photomultiplier (UV/VIS). Spectral selectivity was ensured using a double monochromator (holographic gratings with 1440 lines/nm (VIS/NIR) and 360 lines/mm (UV)), resulting in a spectral resolution of max. 0.1 nm (UV/VIS) or 0.4 nm (NIR). The absorption of the substrate was measured before the actual measurement of the film. In order to account for potential scattering effects of the sample, the transmitted light was captured using a Teflon-coated integrating sphere. The quantity measured is the absorbance A of the film, which is related to the transmission via the formula T: $A = -\log_{10}(T)$. UV/VIS absorption measurements

are used to obtain the optical band gap of a material, which can be estimated via the so-called *Tauc* plot. In order to draw the Tauc plot, a linear fit is used in the onset of the absorption. The band gap E_G can be estimated using the absorption coefficient $\alpha(E)$ and the absorbance A: $\alpha(E) = A\sqrt{E - E_G}$.
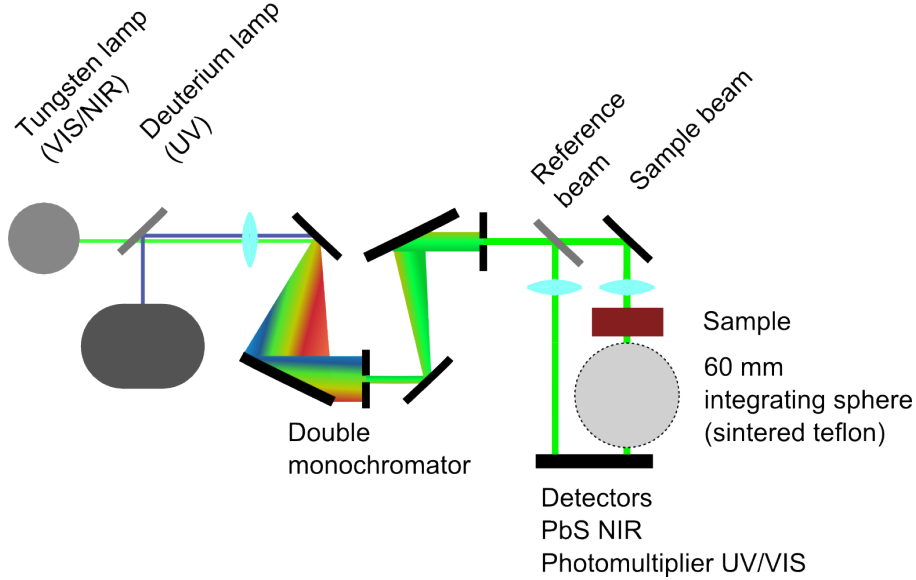

Figure 3.3.: Simplified scheme of the spectrally-resolved UV/VIS/NIR setup. A Deuterium lamp provides radiation in the UV range ($\lambda < 380$ nm), a Tungsten halogen lamp radiation in the VIS/NIR spectral range (380 nm $\leq \lambda \leq$ 900 nm). A double monochromator provides wavelength selection. The transmission through the sample is collected using an integrating (Ulbricht) sphere to account for scattering effects of rough films and analyzed either using a PbS (NIR) detector or a photomultiplier. Reference spectra of a blank substrate ensure the correct measurement of the material absorption.

3.2.2. Photoluminescence spectroscopy

Time-resolved photoluminescence was used to monitor the emissive properties of lead-iodide perovskites. The sample is excited by the frequency-doubled (BBO) output of the Ti:sapphire laser system either with a repetition rate of 80 MHz or 1 kHz and a pulse duration of <150 fs, the photoluminescence is detected with a Hamamatsu streak camera system. The emission of the sample is spatially dispersed by a grating and then collected by a photocathode, which converts the photons to electrons. The number of electrons is proportional to the intensity of the incident luminescence. The electron pass parallel high-voltage electrodes, where a time-dependent electric field spreads the electrons perpendicular to both, the direction of dispersion and the propagation direction. The

time-dependent electric field deflects the photogenerated electrons according to the photon arrival time at the photocathode. The electrons are thus spread in two dimensions and are subsequently multiplied to enhance the signal then reconverted into photons due to the interaction with a phosphorescent screen. The photons are detected with a 2D CCD camera. Depending on the required time resolution, two different modules could be used: either a fast one (80 MHz, instrument response $\sim$ 20 ps) or a slow one (1 kHz, instrument response > 50 ps).
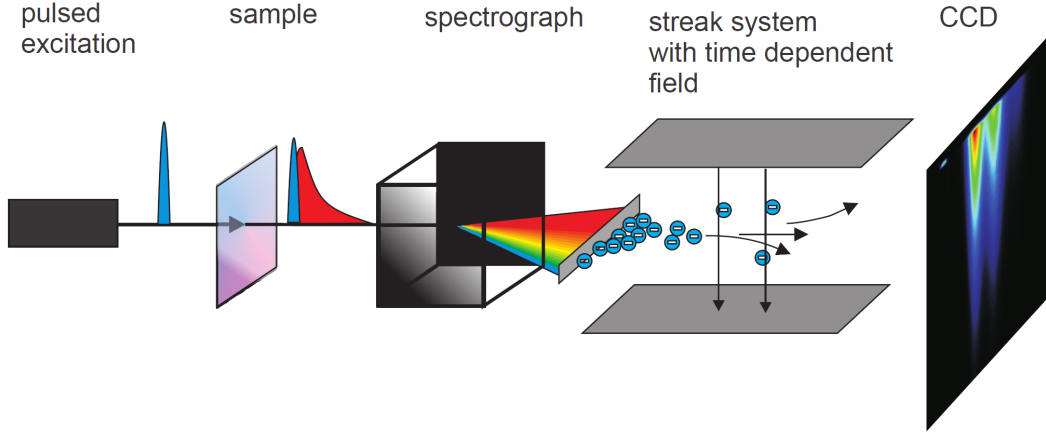

Figure 3.4.: Schematic of the time-resolved photoluminescence setup. The sample is excited from a pulsed laser source. The pump photons interact with the sample where the photoluminescence is generated. The photoluminescence is spectrally dispersed in the grating spectrometer after which electrons are generated in a photocathode. The time resolution is provided by a synchronized fast-sweeping electric field. The electrons are converted to photons at a phosphorescent screen and detected with a CCD camera. From [Etz14]

3.2.3. Transient absorption spectroscopy

Transient absorption spectroscopy (TAS) was used to probe not only emissive species but also populations of photo-excited carriers. The measured quantity in the pump/probe measurement is the relative change in transmission $\Delta T/T$, which is calculated as follows:

$$\frac{\Delta T}{T} = \frac{T_{\text{pump on}} - T_{\text{pump off}}}{T_{\text{pump off}}}.$$

Here $T_{\text{pump on}}$ is the transmission of the sample under pump and $T_{\text{pump off}}$ the transmission of the sample without pump. In a typical experiment, a spectrally narrow but intense

pump beam excites the sample. After a defined time delay, a spectrally broad but weak[3] probe pulse interacts with the excited sample. The probe pulse is spectrally analyzed for every defined time delay. A typical spectrum is shown in figure 3.5.
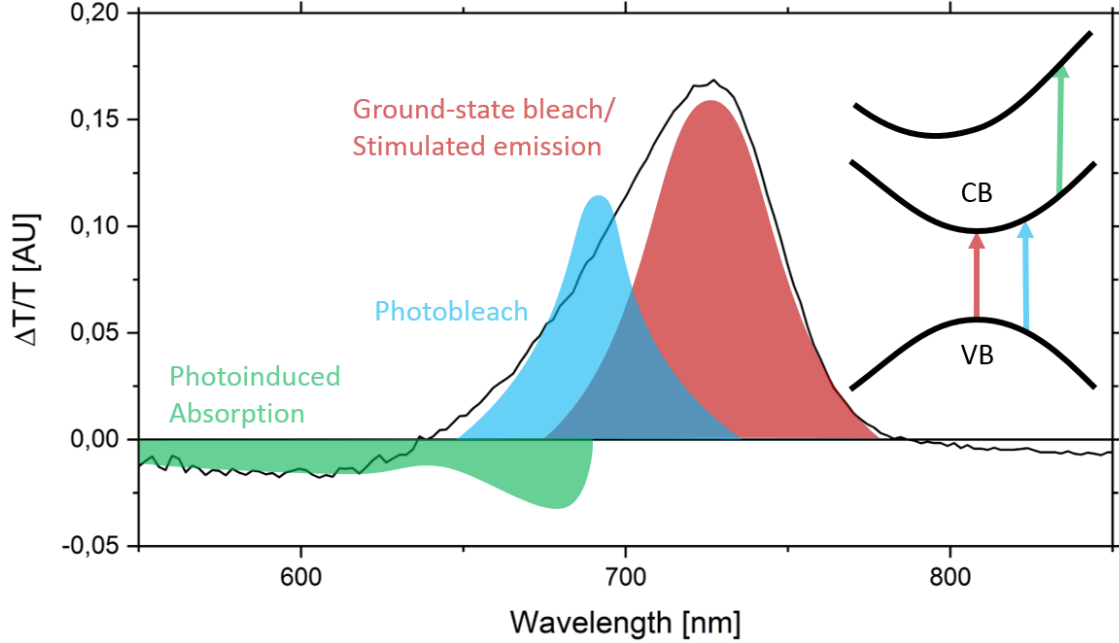

Figure 3.5.: Different signal contributions to the total differential transmission $\Delta T/T$ in transient absorption measurements. The measured signal (black line) can be reconstructed from the ground-state bleach (red, positive $\Delta T/T$), a photobleach (red, positive $\Delta T/T$) and photoinduced absorption (green, negative $\Delta T/T$). The corresponding transitions are schematically shown on the right-hand side.

The overall TA signal consists of multiple components, some of which can enhance the differential transmission $\Delta T/T$, such as the ground-state bleach (GSB) or photobleach (PB), and some of which reduce the differential transmission, a photoinduced absorption (PIA):

- The positive differential transmission of the GSB can be explained by the reduced population of the ground state after the interaction with the pump. The pump excites carriers from the valence to the conduction band (compare figure 3.5, red spectrum/arrow). Probing the wavelength region corresponding to the energetic difference of the band edges will result in an enhanced differential transmission

---

[3]A low-intensity probe pulse is especially important for transient absorption spectroscopy of lead-iodide perovskites as the band gap is energetically close to the fundamental emission of a Ti:sapphire laser, which is often used to generate the spectrally broad probe pulse, see also Sum *et al.* [Sum16].

($\Delta T/T > 0$), as a significant fraction of the carriers was excited and therefore the transition which corresponds to the ground state is *bleached*.

- A photobleach is comparable to the ground state bleach, but originates from states with a higher energy difference than the optical band gap [Sum16], consequently the differential transmission $\Delta T/T > 0$.

- Another spectral component which enhances the differential transmission is the stimulated emission. For the case of stimulated emission, the pump excites the sample; the following probe photon stimulates the emission, resulting in an apparently higher transmission. Due to the small Stokes shift between the absorption and emission of lead-iodide perovskites, the spectral component of the stimulated emission is nearly identical to the ground-state bleach.

- Excited state absorption or photoinduced absorption results in $\Delta T/T < 0$ and occurs if the probe pulse interacts with carriers which were already excited from the pump pulse, such as the interband transition between two conduction bands (compare figure 3.5 and section 2.3.1.2).

The total differential transmission can be derived from the sum of all the spectral contributions, weighted by the transition cross-section $\sigma_{i \to j}$ for a given sample thickness d:

$$\frac{\Delta T}{T}(\lambda, t) = \sum_{i,j} \sigma_{i \to j}(\lambda, t) \Delta N_i(\lambda, t) d.$$

Here ΔN_i is change of population in the state i due to the interaction with the pump pulse.

The transient absorption setup is seeded by the output of a Ti:sapphire laser (Coherent Libra HE), delivering 3.5 mJ of 80 fs pulses at 1 kHz centered at 800 nm. The output of the laser system is split and used to seed two optical parametric amplifiers (OPA), namely OPA 1 and OPA 2 (Coherent OPerA Solo). OPA 1 is used to generate the pump pulses between 290 and 2600 nm. The output of the OPA 1 can be attenuated using an automatized neutral density filter wheel (Thorlabs). The pump beam is guided via a variable (0 - 8 ns) delay line using a mechanical stage and two broadband retroreflectors (Newport) and a diffuser to the sample mounted in a home-built high-vacuum cryostat. The pump pulse is chopped at 500 Hz. The output of the OPA 2 at 1300 nm is focused onto a thin sapphire crystal to generate the supercontinuum (3 mm, c-cut α-Al$_2$O$_3$, compare section 2.4.4). Spectral tunability and stability of the supercontinuum is ensured using a neutral density filter wheel (NDFW) in combination with a pinhole, which allow control of the pulse energy and the beam shape. Careful adjustment resulted in the ideal case in a supercontinuum between 550 and 1100 nm and high stability over 72+h. The supercontinuum interacts with the pumped/unpumped sample is spectrally resolved

using an 150 lines/mm grating spectrometer (Princeton Instruments Acton SP2150) and analyzed using a silicon linear array detector (Ingenieurbüro Stresing).
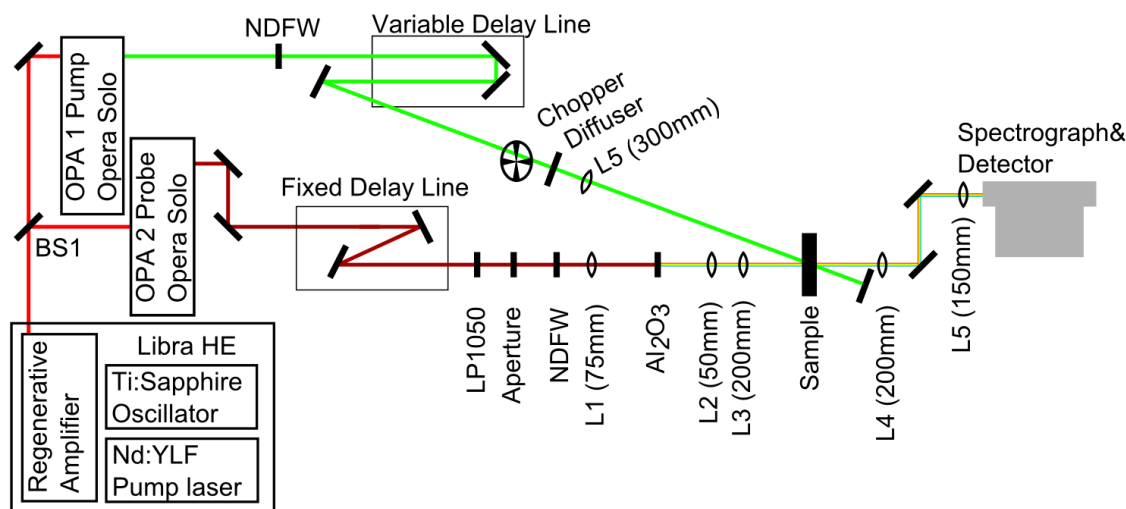

Figure 3.6.: A Ti:sapphire laser system generates pulses at 800 nm, which are used to seed two OPA's (pump in the visible spectral range, probe at 1300 nm). The output of the pump OPA is variably attenuated in a neutral density filter wheel (NDFW), variably delayed with respect to the probe pulse and chopped at 500 Hz before hitting the sample. The output of the probe OPA 2 is used to generate a supercontinuum centered at 1300 nm, which probes the pump-induced transmission change in the sample. The probe beam is spectrally dispersed in a grating spectrometer and detected with a CCD camera.

Data obtained from the TA measurements are two-dimensional matrices with axis of time and wavelength/energy. Spectra are obtained by averaging over a minor range[4], kinetics by averaging over a spectral region. The raw data still contains the chirp caused by transmissive optical elements, such as the lenses used to focus the probe beam, cryostat-windows and sample, and are corrected using a home-built Matlab-script[5], visualized in figure 3.7.

3.2.4. Time-resolved THz spectroscopy

The time-resolved THz experiments are based on a Ti:sapphire laser system (Newport Solice Ace, 800 nm, 40 fs, 1 kHz). The output of the laser system is split into two components;

---

[4]E.g. between 1 and 1.5 ps
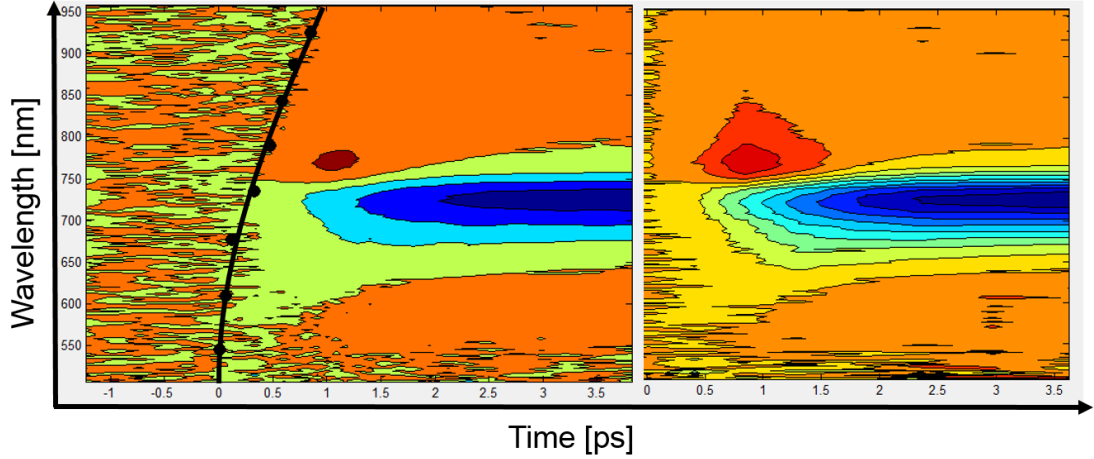[5]Written by Fabian Etzold, Ian Howard *et al.*

Figure 3.7.: Illustration of the chirp correction. Left is the raw data with the fitted chirp (along the dots), the chirp-corrected data is shown in the right-hand side panel .

one seeds an OPA (TOPAS prime NIR-UV/VIS) in order to obtain wavelength-tunable pump pulses. The remaining power is used to seed the THz generation and detection scheme. The overall setup is shown in figure 3.8. The 800 nm beam is split into three different parts: pump beam, THz generation and detection beam. For the pump beam, frequency-doubling in 100 μm thick BiB_3O_6 (BiBO) was found to be optional. The pump beam is guided via a variable delay line (maximum delay: 1.5 ns) to the sample. The pump beam is chopped at 500 Hz and scattered/absorbed by foam[6] after interaction with the sample. The 800 nm pulses are used to generate ∼1 ps long THz pulses in a 1 mm ZnTe crystal. THz pulses generated in this way present a spectrum that ranges from 0.5 to 2.5 THz (see figure 2.14). The THz pulses are guided by parabolic mirrors to the sample, which is mounted in a cryostat. After the interaction with the sample, the THz pulses are re-collimated and then focused onto a second ZnTe crystal for electro-optical sampling. The detection beam is delayed with another delay stage in order to allow sampling of the THz-pulse. The sampling and THz-probe pulses are overlapped in the second ZnTe crystal. Due to the Pockels-effect in the crystal, the polarization of the sampling beam changes. A quarter wave-plate is used to change the polarization from linear to elliptical, which is then separated into vertical and horizontal polarization components by a Wollaston prism. Two balanced photodiodes are used to detect the relative intensity of the two polarization components. The intensity of the signal is acquired using lock-in detection; the modulation is obtained by chopping the THz-generation and/or the pump beam. The differential output of the diodes is set to zero via the quarter wave-plate in

---

[6]Absorbing UV/VIS/NIR light, but transmitting THz in order to prevent THz generation in the seconds ZnTe crystal.

case the THz-field is absent; therefore, the measured signal is proportional to the field strength of the THz-pulse. In order to reduce the absorption of the THz pulse by water vapour, the pump-probe setup was continuously flushed with dry nitrogen.
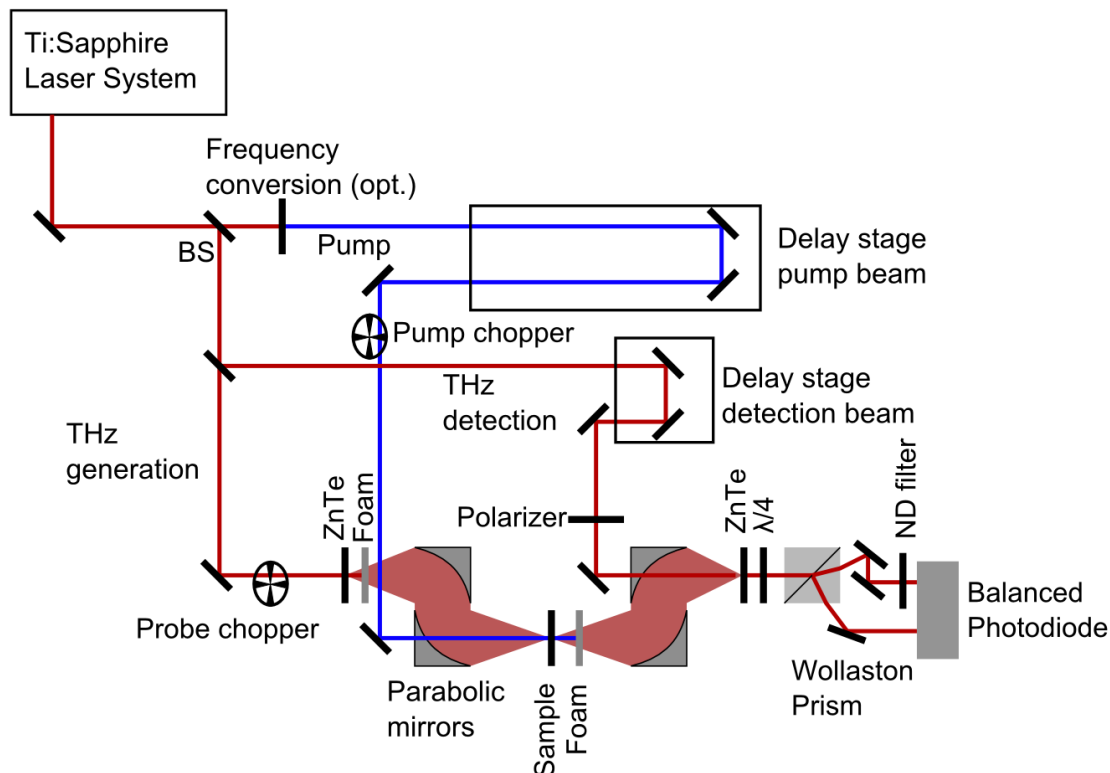

Figure 3.8.: Scheme of the time-resolved THz setup. The output of the Ti:sapphire laser system is split into three components: the pump beam, the THz generation beam, and the THz detection beam. The pump beam can be frequency converted, e.g. via an OPA or a nonlinear crystal, and is delayed using a delay stage with respect to the THz generation beam. A different fraction of the laser output is used to generate THz via optical rectification in a ZnTe crystal. The THz pulses are collimated and focused using a pair of parabolic mirrors. Foam is used to scatter/absorb the remaining pump and laser beam. The detection beam is also variably delayed with respect to the generation in order to allow sampling of the THz pulse via electro-optical sampling in the second ZnTe crystal. The polarization of the detection beam is rotated due to the Pockels effect. The quarter wave plate and the Wollaston prism are used to balance the diodes when no THz pulse is present. The different polarization components are detected with balanced photodiodes.

In a typical measurement, e.g. in order to obtain the time-resolved real photoconductivity, the peak of the THz-pulse is determined via scanning the delay of the detection beam

while the generation beam was chopped at 500 Hz. The obtained peak time is then fixed, and the pump-probe time delay is scanned while the pump is chopped at 500 Hz. For frequency-resolved photoconductivity measurements, it is required to scan both, the pump and the detection stages. The dual scanning allows sampling the THz-pulse for a defined pump-generation delay.

4. Quantifying Polaron Formation and Charge Carrier Cooling in Lead-Iodide Perovskites

This chapter is based on the submitted manuscript entitled "Quantifying Polaron Formation and Charge Carrier Cooling in Lead-Iodide Perovskites". This work is a collaboration between Ivan Ivanov from the Max Planck Institute for Polymer Research Mainz (Germany) and the Department of Chemistry of the Columbia University (United States).

4.1. Abstract

Notwithstanding the success of lead-halide perovskites in emerging solar energy conversion technologies, many of the fundamental photophysical phenomena in this material remain debated. Here, we study the initial steps following photogeneration of free charge carriers in lead-iodide perovskites, and quantify timescales of charge carrier cooling and polaron formation, as a function of temperature and charge carrier excess energy. We find, using terahertz time-domain spectroscopy (THz-TDS), that the observed femtosecond rise in the photoconductivity can be described very well using a simple model of sequential charge carrier cooling and polaron formation. For excitation above the bandgap, the carrier cooling time is strongly dependent on the charge carrier excess energy and lattice temperature, with cooling rates varying between 3 and 6 meV/fs. The polaron is formed within 400 fs for both $CH_3NH_3PbI_3$ (MAPbI$_3$) and $CH(NH_2)_2PbI_3$ (FAPbI$_3$), and its formation time is independent of temperature between 160 and 295 K. The very similar dynamics observed for the two perovskites points to the critical role of the inorganic lattice, rather than the organic cations, for polaron formation and cooling.

4.2. Introduction

The astonishing rise of lead-halide perovskite in the world of optoelectronic devices began only a few years ago. [Lee12, Koj09] In the short period of time, the technol-

ogy has advanced so fast that the power conversion efficiency of lead-halide perovskite-based devices now rivals established technologies like CdTe and multicrystalline silicon. [RN317, Yan17a, Aro17] The success of the material can be traced to low charge carrier recombination rates, ambipolar charge transport, strong optical absorption and its solution processability. [Tre17, Str15b, CB17] The current debate about the origin of the low recombination rates in lead-halide perovskite suggests multiple possibilities: a direct/-indirect character of the band structure due to the Rashba-effect, charge separation due to ferroelectric effects and the formation of polarons. The Rashba-effect results in a small lateral shift in the k-space between the conduction band minimum and the valence band maximum and therefore in an indirect bandgap, which could explain the slow charge carrier recombination. [Hut17, Yu16, Zhe15a, Zhe15a, Eti16, Nie16b] Also under intense debate are ferroelectric properties in perovskites, which could allow spatial separation of electrons and holes in the lattice. [Fro16b, Her16a, Kut14, Anu17, Rak17] Finally, it has been proposed that polaron formation allows reduced scattering of charge carriers with phonons, other carriers or charged defects, resulting in low recombination rates. [Zhu15b, Wol17, Bon17, Miy17b, Fro17b, Fro17a, Zhu16] The concept of the polaron has also been put forward to explain the moderate mobility of charge carriers in lead-halide perovskites. [Fro17b, Fro17a, Che16, Fey55, Fey62] Polarons form in polar semiconductors due to the interaction of charge carriers and phonons and are especially important in soft and polar crystals. [Zhu15b, Bon17, Lan48] The formation of the polarons is energetically preferred compared to a bare charge carrier resulting in efficient screening of its electric field and occurs with a characteristic timescale in the order of ~100 fs. [Miy17b, Fro17b, Lan48, Iva17, Bok16] Within conventional polaron theory, the strength of electron-phonon interaction is expressed by the dimensionless Fröhlich coupling constant α,

$$\alpha = \frac{e^2}{\hbar c}\sqrt{\frac{m_e^* c}{2\hbar\omega_{LO}}}\left(\frac{1}{\varepsilon_\infty} - \frac{1}{\varepsilon_0}\right). \tag{4.1}$$

Here, c is the speed of light, $\hbar$ the reduced Planck constant, e the fundamental charge, m_e^* effective mass (or band mass) of the charge carrier, ω_{LO} the angular frequency of the coupled LO-phonon, ε_∞ the optical and ε_0 the static dielectric constant. [Bok16] Depending on the electron-phonon coupling strength, polarons may be described as small or large and can be distinguished by e.g. temperature-dependent transport measurements. [Zhu15b, Fro17b, Fro17a, Wri16, Mil15] For lead-halide perovskite, α has been calculated to lie between 1.1 and 2.7, establishing the polaron as intermediate-to-large, which is supported by the increased mobility at lower temperatures. [Yu16, Fro17b, Fro17a, Sen16, Miy17a] In addition to the origin of long lifetimes of the photogenerated carriers, polarons has also been invoked to account

for the discrepancy between predicted high mobility (> 1000 cm^2/Vs, due to small effective mass of charger carriers) and the measured lower (< 100 cm^2/Vs) one. [Wol17, Fro17b, Fro17a, Che16, Fey55, Fey62] A number of spectroscopic methods have been used to observe polaron behavior, but the formation has so far only been reported for bromine-based perovskite. [Miy17b] In contrast, and numerous publications have reported carrier cooling at high ($> 10^{18}$ cm^{-3}) and low ($< 10^{18}$ cm^{-3}) charge carrier densities. For high charge carrier densities, a hot phonon bottleneck can slow down the cooling of carriers. [Pri15, Yan15, Dob17, Fu17] For low charge carrier densities, long hot carrier lifetimes have been reported as well, with the mechanism debated: both intervalley scattering between a side valley at the M-point with a band gap of ~ 2.5 eV and the Γ-Valley, and the ultralow thermal conductivity of lead-halide perovskites have been proposed to play an important role in accounting for long-lived hot carriers. [Fro17b, Zhu16, Bre17b, Nie16c, Cha16, App17a, Pis14, Yan17b, Wu17, Mos17]

Here, we present the first estimation of the polaron formation time in the two most common single organic cation lead-iodide perovskites, CH$_3$NH$_3$PbI$_3$ (MAPbI$_3$) and CH(NH$_2$)$_2$PbI$_3$ (FAPbI$_3$), and in parallel quantify charge carrier cooling. Given its sensitivity to the mobile charge carriers and its high ($\sim$250 fs) time resolution, terahertz time-domain spectroscopy (THz-TDS) is an ideal method to investigate the initial dynamics of the conductivity of the photo-excited charge carriers (so called photoconductivity) with respect to the formation of polarons and the initial charge carrier cooling. The equilibration of the conductivity after the photoexcitation must reflect cooling of hot carriers and polaron formation. We observe a temperature- and excess energy-dependent sub-picosecond rise of the photoconductivity. Polaron formation is observed to be temperature-independent, while carrier cooling is both temperature- and excess energy-dependent. The combined data can be well described by a model assuming sequential cooling and polaron formation. We find initial charge carrier cooling rates between 3 meV/fs at 160 K and 6 meV/fs at 295 K. Our results are consistent with polaron formation subsequent to cooling on timescales of 400 $\pm$ 20 fs for FAPbI$_3$ and 390 $\pm$ 10 fs for MAPbI$_3$.

4.3. Results and discussion

To study the carrier cooling and polaron formation, we record the time-resolved photoconductivity of perovskite samples prepared by solvent-engineering with the most common cations, methylammonium and formamidinium, MAPbI$_3$ and FAPbI$_3$. The samples were kept under vacuum conditions, the temperature was varied between 160 and 295 K using a liquid nitrogen cryostat and the pump wavelength was selected between resonant to the

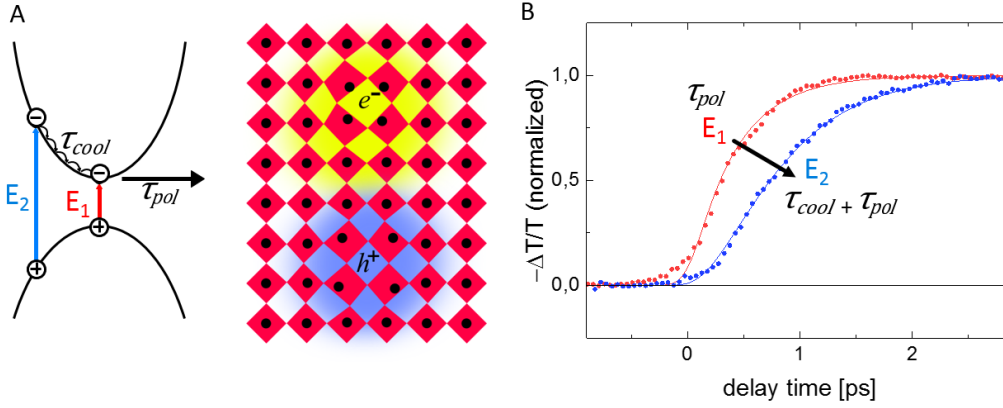bandgap (800 nm, no excess energy) and 400 nm (excess energy ~1.5 eV).

Figure 4.1.: Illustration of the effects of polaron formation and carrier cooling on the measured time-dependent photoconductivity. Panel (A) shows a scheme of the polaron formation and carrier cooling: For resonant excitation with the frequency E_1 (in red), a polaron will be formed due to the interaction of the electron and the lead-halide lattice with a characteristic timescale of τ_{pol}. For above band gap excitation with light with photon energy E_2 (in blue), the carriers cool with timescale of τ_{cool}, prior to polaron formation. The effect of the resonant and above band gap excitation is illustrated in (B). For resonant excitation (800 nm, 1.55 eV), the photoconductivity rises faster compared to the above band gap excitation (400 nm, 3.1 eV) due to the occurrence of both carrier cooling and polaron formation.

THz spectroscopy measures the complex-valued photoconductivity, which is correlated to the mobility and the effective mass of charge carriers by: $\sigma \sim Ne^2\tau_{scat}/m_e^*$, where, e is the fundamental charge, m_e^* effective mass (or band mass) of the charge carrier, N is the charge carrier density and τ_{scat} the scattering time .[Ulb11] Within the frequency window (0.5-2.2 THz), the photoconductivity reveals no significant frequency-dependence (figure 4.4A), indicating that the carrier scattering time is less than ~20 fs. As such, we can simply plot the photoconductivity at the peak of the terahertz pulse to follow the dynamics. In order to investigate the effects on the photoconductivity rise of (i) excess energy and (ii) temperature (in the temperature range over which the crystal structure is tetragonal), we systematically varied both parameters. A scheme with the effects of polaron formation and the carrier cooling for the case of FAPbI$_3$ at 160K is shown in figure 4.1. The photoconductivity increases during the first ~1.5 ps after photoexcitation (figure 4.1B, E_1 in red) to a quasi-steady-state photoconductivity, showing no decay on ~100 ps timescales (figure 4.6). Within the Drude conductivity picture, the delayed rise

of the photoconductivity due to polaron formation upon on-gap excitation can be explained by a decrease in the carrier scattering rate upon polaron formation. The dressing of carriers with phonons, i.e. polaron formation, will also result in an increased effective mass by 20 - 45%, which should reduce the conductivity proportionally. [Fro17a] This relatively small increase of the effective mass is apparently more than compensated by the reduction of carrier-optical phonon-scattering. The additional delay in the rise of the photoconductivity upon above-gap excitation due to carrier cooling can be understood by noting that excitation above the bandgap in the Γ-valley will result in an enhanced effective mass due to the nonparabolicity of the bands away from the band extrema. [Dem16, Her16b] The most relevant results for both $FAPbI_3$ and $MAPbI_3$ are shown in figure 4.2. Low-fluence optical excitation (5.6 $\mu J/cm^2$) was used to prevent significant electron-hole and Auger recombination, which is reflected in the near-constant photoconductivity over the first 100 ps (figure 4.6). [Her16b, Sum14] We measured the instrument response function (IRF) using a thin layer of TiO_2 and 320 nm optical excitation, resulting in an IRF of Gaussian shape with FWHM of 250 fs (for a more detailed discussion see figure 4.7). Clearly, the observed rise of the photoconductivity in the perovskites is appreciably slower than the instrument response function, even for band-edge excitation, which we attribute to a finite polaron formation time. For excitation without excess energy (see figure 4.2A, B), the photoconductivity rise is independent of temperature (160 - 295 K), occurring within $\sim$1.5 ps for $FAPbI_3$ and $MAPbI_3$. Notable differences can be observed for the rise time of the photoconductivity for both increasing excess energy (see figure 4.2C, D) and temperature (figure 4.2E, F), respectively. The rise of the photoconductivity increases for both, higher excess energy (shorter excitation wavelength) and lower temperature, respectively. The rise in the photoconductivity is unlikely to be limited by the generation of free carriers, which has been reported to occur on timescales most likely smaller than 100 fs, only limited by the rapid thermalization of carriers. [Yan15, Nie16c, Pon17, Sav14, Pon14, Gho17, Mon17, VC15, Yin14b] In order to quantify the rise dynamics before reaching the equilibrium photoconductivity (constant carrier number, scattering time and effective mass), we propose a model with two distinct, sequential contributions to the rise of the photoconductivity: carrier cooling and polaron formation, i.e. the model assumes carrier cooling occurs prior to polaron formation.

We use a three-level system in which the relevant populations are named N_{hot}, N_{cold} and N_{pol} (the number of hot, cooled carriers and polarons) and time scales τ_{cool} and τ_{pol} (relaxation between N_{hot} and N_{cold} and N_{cold} and N_{pol}, respectively.) For band-edge excitation, the carriers are directly excited to N_{cold}; for excitation with excess energy to N_{hot}.

Thereby we obtain the following rate equations:

$$\frac{dN_{hot}}{dt} = -\frac{1}{\tau_{cool}} N_{hot} \qquad (4.2)$$

$$\frac{dN_{cold}(t)}{dt} = \frac{1}{\tau_{cool}} N_{hot} - \frac{1}{\tau_{pol}} N_{cold}(t) \qquad (4.3)$$

$$\frac{dN_{pol}(t)}{dt} = \frac{1}{\tau_{pol}} N_{cold}(t). \qquad (4.4)$$

With a fraction n excited to the *hot* state, the initial conditions read:

$$N_{hot}(t = 0) = n \qquad (4.5)$$

$$N_{cold}(t = 0) = N_{pol}(t = 0) = 0 \qquad (4.6)$$

$$N_{hot} + N_{cold} + N_{pol} = 1. \qquad (4.7)$$

Solving the rate equations, we obtain, for the time-dependent polaron population

$$dN_{pol}(t) = n \left[\frac{1}{\tau_{cool} - \tau_{pol}} \left(\tau_{pol} \exp\left(-\frac{t}{\tau_{pol}} \right) - \tau_{cool} \exp\left(-\frac{t}{\tau_{cool}} \right) \right) + 1 \right]. \qquad (4.8)$$

The polaron formation time τ_{pol} can be inferred directly from experiments with near-zero excess energy of the charge carriers (band edge excitation), and is found to be temperature independent, amounting to 400 ± 20 fs for both FAPbI$_3$ and MAPbI$_3$ (lines in figures 4.3 A and B) . The temperature independence of polaron formation can be explained by the Debye temperatures of < 140 K in the tetragonal phases of both materials, which means that phonons below a frequency 3.3 THz are thermally excited, including LO phonon modes responsible for the polaron formation. [Fro17a, Wri16, DI14a, Fen14] In contrast, the cooling time τ_{cool} is temperature- and excess-energy dependent due to the temperature-dependent phonon emission probability. [Mil15, Ulb11, Zeg11, Hen04] figures 4.2 C-F show the substantial influence of the excess energy and the temperature on the rise time of the photoconductivity. These traces are in agreement with previous studies of time-resolved photoconductivity in lead-halide perovskite, reporting photoconductivity rise times of 300 fs and upward. [Pon17, VC15, PJ16] In order to quantify the cooling of carriers, we extract average cooling times (table 4.2) from the global fitting within the assumption of linear dependence on the excess energy. At room temperature, the range of the cooling time ranges between 39 fs (700 nm excitation) and 275 fs (400 nm excitation) for FAPbI$_3$ and 30 fs (700 nm excitation) and 316 fs (400 nm excitation) for MAPbI$_3$. For lower temperatures, the cooling time increases compared to the room temperature measurement. Cooling rates derived from the cooling times are summarized in Table 1, revealing faster cooling (see figure 4.3B) at elevated temperatures for both FAPbI3 and MAPbI$_3$, with somewhat higher rates for the former. We stress here the limitations

of the sequential cooling and polaron formation model, as it excludes the possibility of simultaneous polaron formation and cooling and the formation and cooling of hot polarons. Our model is also insensitive to variations in the density of states near the band-edges, which will likely affect the cooling rates. [Nie16c, Dem16, Kaw15, End16a] Nonetheless, the good description of the data provided by this simple model lends some credence to the assumptions.
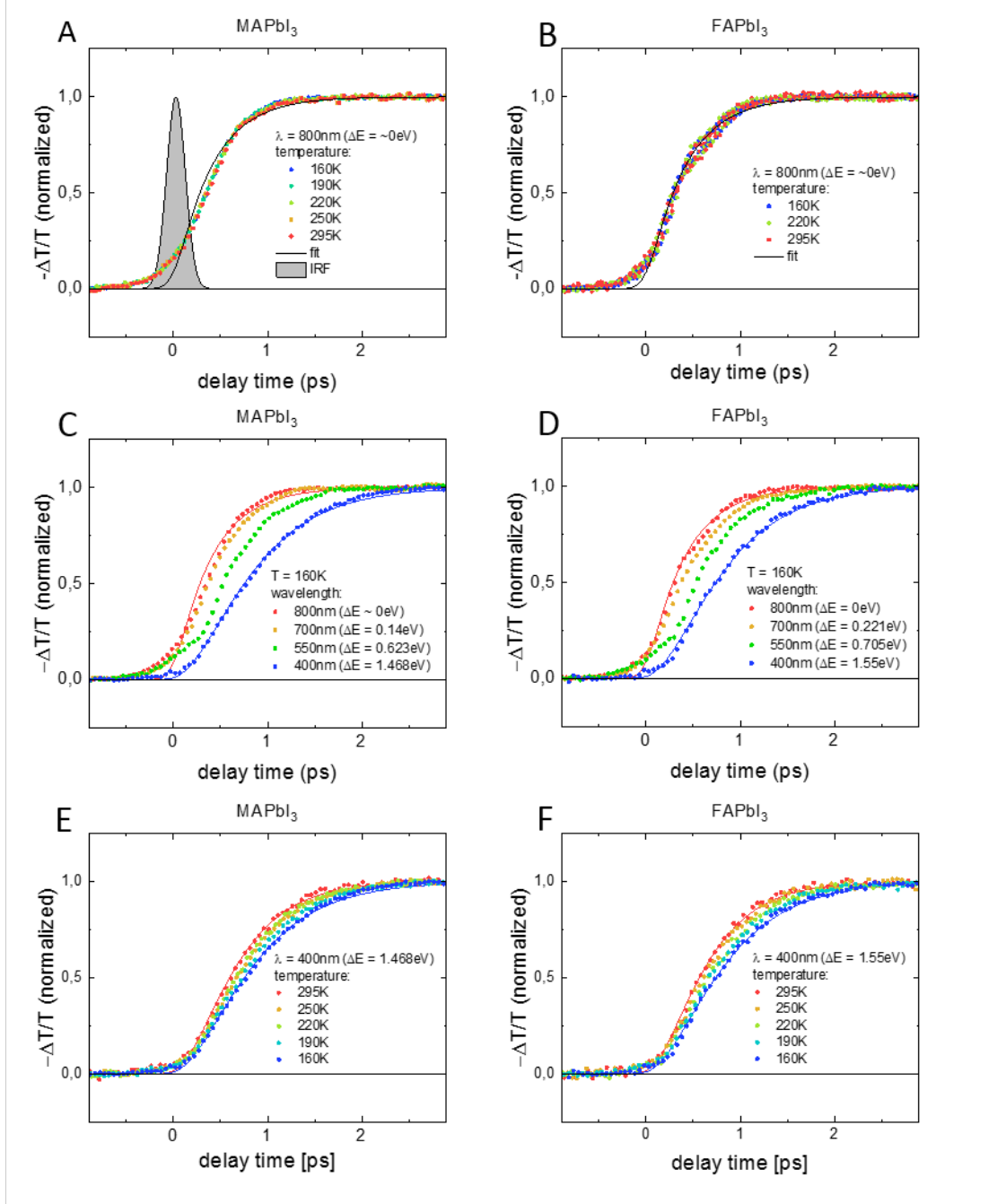
Figure 4.2.: Time-resolved THz photoconductivity measurements. (A) shows the temperature-independent rise of the photoconductivity of MAPbI$_3$ for temperatures between 160 and 295 K after excitation at 800 nm. (B) The same measurement as (A), but for FAPbI$_3$. The Gaussian fit of the instrument response function is shown in grey. In all figures, the solid lines show the fits obtained from the rate equations discussed in the text. The zero time is obtained from the convolution of the data and the instrument response function. The deviation of the fits to the measured data is attributed to non-exponential contribution to the rise of the photoconductivity and different excitation pulse duration for the individual pump wavelength. (C) shows the evolution of the (normalized) photoconductivity rise dynamics with different excess energies in photo-generated carriers in MAPbI$_3$ at 160 K by excitation between 400 nm (blue, high excess energy) and 800 nm (red, no excess energy). (D) The same measurement as (A), but for FAPbI$_3$. The rise of the photoconductivity is slower for shorter pump wavelength/higher excess energy for both FAPbI$_3$ and MAPbI$_3$, respectively. (E) and (F) show the temperature-dependent rise of the photoconductivity for temperatures between 160 and 295 K after excitation at 400 nm, E for MAPbI$_3$ and F for FAPbI$_3$, respectively. For both, FAPbI$_3$ and MAPbI$_3$, respectively, a lower temperature results in a slower rise of the photoconductivity.

T [K]	FAPbI$_3$ [meV/fs]	MAPbI$_3$ [meV/fs]
160	3,23 ± 0,08	2,90 ± 0,08
190	3,82 ± 0,13	3,30 ± 0,11
220	4,14 ± 0,14	3,87 ± 0,15
250	4,99 ± 0,23	3,76 ± 0,14
295	5,63 ± 0,28	4,63 ± 0,22

Table 4.1.: Average cooling rates obtained from the temperature- and excess-energy dependent rise of the photoconductivity.

Both the formation of polarons and the cooling of hot carriers rely on electron-phonon-coupling. Polaron formation is enabled by the interaction of the LO-phonon with charge carriers. [Zhu15b, Bon17, Fro17b, Fro17a, Sen16] As LO phonon modes are already excited due to thermal excitation and the initial charge carrier thermalization, a fully quantum-mechanical treatment is not required, instead we can estimate the timescale of the polaron formation simply from the LO phonon oscillation period, ω_{LO}^{-1}. [Fro17b, Bet04, Bet02] Sendner *et al.* have reported frequencies of 2.75 and 3.6 THz for MAPbI$_3$, Wright *et al.* 6.3 THz for MAPbI$_3$ and 4.6 THz for FAPbI$_3$ and Frost *et al.* 2.25 THz. Assuming that polaron formation requires ∼1 cycle of the relevant phonon frequency, these frequencies result in approximate timescales for the polaron formation between 180 and 450 fs, which is consistent with our inferred polaron formation time of 400 fs. [Fro17b, Wri16, Sen16]

Miyata *et al.* recently reported excess-energy independent polaron formation times of $\sim$ 300 fs for MAPbBr$_3$ and $\sim$ 700 fs for CsPbBr$_3$ based on the decay of a signal measured with transient reflectance, which can be associated with the band-gap renormalization observed at higher fluences, concurrently occurring with decay of transient birefringence. [Miy17b]
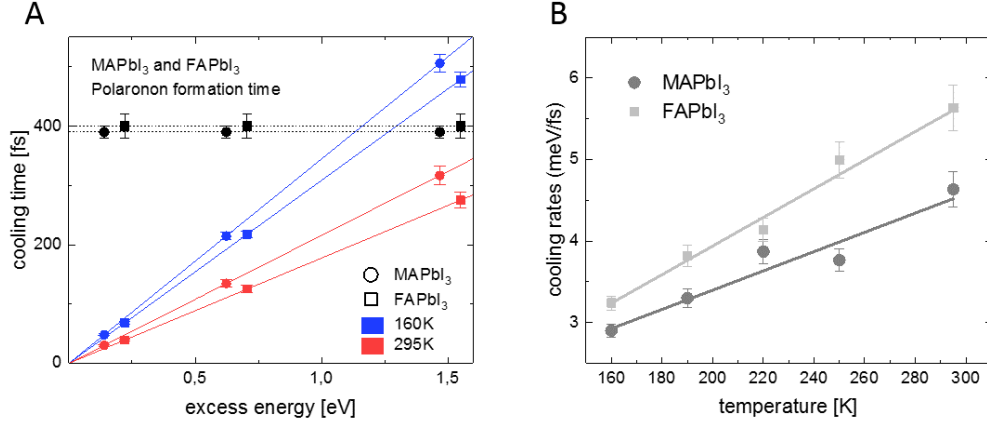

Figure 4.3.: Results of the fitting of the photoconductivity using the three-level system for both FAPbI$_3$ and MAPbI$_3$, respectively. (A) shows the cooling time obtained from the fitting for excess energies corresponding to pump wavelength of 700, 550 and 400 nm. For higher excess energy/shorter excitation wavelength, a longer cooling time is observed. For comparison, the polaron formation time of 400 ± 20 fs for FAPbI$_3$ and 390 ± 10 fs for MAPbI$_3$ is also shown. Lines are to guide the eye. (B) shows the extracted cooling rate in meV/fs. Both FAPbI$_3$ and MAPbI$_3$, share an increase of the cooling rate with increasing temperature. The slope of the temperature-dependent cooling rate is slightly steeper for FAPbI$_3$ compared to MAPbI$_3$.

We note that Price *et al.* reported that for transient absorption measurement, the same feature vanishes with reduced excess energy and might, therefore, be also related to cooling of carriers. [Pri15] Monahan *et al.* observed a rise time of $\sim$300 fs and a long-living coherent phonon TO-phonon population in two-dimensional electronic spectroscopy. [Mon17] Although the formation of the polaron is associated with the higher frequency LO phonon, coherent (and virtual) phonons, which appear on a shorter timescale than their inverse frequency were reported to accompany the dressing of charge with phonons in order to form a polaron. [Bet04] Valverdez-Chavez *et al.* found a sub-ps reduction of the mobility using broadband photoconductivity measurements in reflection, which could also be associated with the formation of polarons, at, however, substantially higher carrier densities. [VC15] Changing the lattice and carrier temperature (i.e. the

excess energy thus the pump wavelength) does not alter the formation of the polaron, but is expected to influence carrier cooling due to the reduced probability of emitting phonons at reduced temperatures. The temperature-dependent blue-shift of the absorption edge is on the order of 0.1 eV between 295 and 160 K and will slightly reduce the total excess (pump) energy. [DI14a] Thereby, we did not account for this blue-shift as the expected impact on the cooling times is insignificant. The influence of the carrier excess energy was, in agreement with our measurements, also observed by Yang *et al.*, who found that increasing the pump energy from 2.1 to 3.1 eV is correlated with an increase the cooling time. [Yan15] The mechanism of the cooling was determined to be LO-phonon emission. Niesner *et al.* measured time-resolved two-photon photoelectron spectroscopy of MAPbI$_3$ at 190 K and reported cooling time of 280 fs for electrons with an excess energy of 0.5 eV, which is comparable to our measurements (see figure 4.2C for an estimate of the cooling time at 190 K for a total excess energy for electrons and holes of 1 eV) and was recently confirmed by Fu *et al.* [Fu17, Nie16c] Niesner *et al.* propose that the formation of polarons, the reduced scattering with optical phonons and the ultralow thermal conductivity are responsible for the long lifetime of hot carriers, which were also independently reported by Bretschneider *et al.* [Fro17b, Miy17a, Bre17b] The differentiation and connection between the initial thermalization in the side valley around the M-point, polaron formation, intervalley-scattering and the role of optical-phonon scattering is not straightforward and is also not possible based on our measurements due to the small contribution from the conductivity for heavy carriers/polarons at the M-point. The much higher average cooling rates extracted from our measurements in comparison with values predicted by Frost *et al.* (at room temperature: ∼5 meV/fs vs. ∼0.1 meV/fs) is possibly related to initial thermalization of charge carriers and carrier-carrier scattering, photoinduced changes in the dielectric function and inelastic carrier-phonon scattering within ∼120 fs. [Miy17b, Fro17b, Pri15, Ric17, Bal97]

Interestingly, the frequency-resolved conductivity of FAPbI$_3$ and MAPbI$_3$, show a temperature dependence very similar to that of the cooling rates: the photoconductivity and the corresponding scattering times, increase almost linearly by a factor of ∼2 when the temperature is lowered from 295 to 160 K (see ESI for a detailed discussion). For steady-state charge carrier scattering, this temperature dependence has previously been interpreted as scattering with acoustic phonons; the observation of the very similar temperature dependence for the cooling rate, which must involve a LO phonon emission, seems to indicate that scattering may also optical, rather than acoustic, phonons, as also supported by the conclusions by Yang *et al.* [Fro17a, Che16, Wri16, Yan15, Man17, Zha17a] Guo *et al.* reported long-range ballistic transport of carriers, but the rise, rather than decay, of the initial photoconductivity

prove that the conductivity of the hot carriers is lower than that of the cold carriers and therefore are inconsistent with long-range ballistic transport prior to cooling. [Guo17, Kue10] The overall almost identical results for MAPbI$_3$ and FAPbI$_3$ supports the proposition that the polaron behavior of charge carriers in lead-iodide perovskites originates from the coupling of the charge carriers to the lead-halide lattice rather than to the organic cations. [Bon17, Miy17b, Zhu16, Che16, Iva17, Yan15, Zhu17] This proposition is in line with the relevant optical phonons involving predominantly lead-halide lattice motion, and being quite similar for both materials (see also figure 4.4A). Indeed, the cation-lattice interaction was recently concluded to be not significantly different for MAPbI$_3$ and FAPbI$_3$. [Fab17] However, the role of hydrogen bonds between the organic cations and the lattice, the rotation of the cations itself with the almost identical timescales of cation rotation and carrier-phonon interaction and the connection to polaron formation and initial carrier cooling are important question to be answered in order to fully elucidate the fundamental photophysical phenomena in lead-halide perovskite solar cells. [Bok16, Fab17, Sel17, Bak15]

4.4. Conclusion

We report the initial charge carrier dynamics of the two most prominent lead-iodide perovskites, FAPbI$_3$ and MAPbI$_3$ between 160 and 295 K. We find that the increase of photoconductivity can be described well using a simple model, in which the initial carrier cooling and polaron formation take place sequentially. For the polaron formation, we find temperature-independent times of 400 ± 20 fs for both FAPbI$_3$ and MAPbI$_3$, which, to the best of our knowledge, is the first report for these particular materials. For the cooling time of the thermalized carriers in the Γ-valley before polaron formation, we extract average rates, 5.6 ± 0.3 meV/fs for FAPbI$_3$ and 4.6 ± 0.2 meV/fs for MAPbI$_3$ at room temperature. Additionally, the cooling rates are temperature-dependent (changing by factor of $\sim$1.8 from 295 to 160 K), which is measured under non-equilibrium conditions during the rise of the photoconductivity. We attribute the temperature-dependence of the photoconductivity to optical phonon scattering, which is therefore also the limiting processes for carrier cooling and the mobility/band-like transport of the (intermediate) polaron.

4.5. Acknowledgments

4.6. Supporting Information

Perovskite film deposition

Fused silica samples (Präzisions Glas & Optik GmbH, Germany) were cleaned in an ultrasonic bath with 2% Hellmanex solution, acetone, isopropanol and a final rinse of ethanol. Prior to spin-coating of the organic films, the substrates were plasma etched for 20 min in oxygen plasma. The perovskite samples were prepared in a nitrogen-filled glovebox with an oxygen level of < 1 ppm. A 1.2 M solution of MAI or FAI (Dyesol) and PbI2 (99.9985 % purity, Alfa Aesar) in anhydrous DMF (Sigma Aldrich) was spin-coated on fused silica for 10 s at 1000 rpm and 30 at 4000 rpm. After 20s, 100 μl of in anhydrous chlorobenzene (Sigma Aldrich) were dropped on the spinning sample to initiate the crystallization. MAPbI$_3$ samples were annealed at 100 °C for 30 minutes, FAPbI$_3$ at 150 °C for 20 minutes. The samples were stored overnight prior to analysis. Time-resolved THz measurements were performed under high vacuum conditions without any exposure to ambient conditions. All chemicals were used as received.

Time-resolved THz measurements

Experiments were performed using a regenerative amplified, mode-locked Ti:sapphire based femtosecond laser system (Newport Solice Ace, 800 nm, 40 fs, 1 kHz). A fraction of the laser output was used to generate ∼1 ps THz pulses in 1mm ZnTe crystal between 0.5 and 2.5 THz. The samples were either pumped with the fundamental laser output, frequency doubled (100 μm BiB$_3$O$_6$) or with 550 and 700 nm pulses generated with a TOPAS prime NIR-UV/VIS. The pump pulses were delayed with respect to the THz probe pulse, the polarization of the pump and probe is parallel. The pump beam was chopped at 500 Hz using a mechanical chopper. The samples were cooled using a Janis VPF-700s cryostat.

Characterization

X-ray diffraction measurements were carried out on a Philips PW 1820 Diffractometer with Cu-K$_\alpha$ radiation ($\lambda = 1.5418$ Å) under dry nitrogen flow. UV/VIS measurements were performed using a Perkin Elmer UV/VIS/NIR spectrometer (Lambda 900) in a 150 mm integrating sphere with a spectral resolution of 1 nm.

Fitting procedure

In order to fit our model to the measured data we first convoluted the analytical expression for the polaron population N$_{pol}$ (t) with the instrument response function (IRF), which is Gaussian function with FWHM $w = \sim 250$ fs and was measured experimentally as explained in the main text). The convolution was performed in Wolfram Mathematica. The resulting equation that we fit to the measured data:

$$
\begin{aligned}
N_{pol}(t) = 1 &+ \mathrm{Erf}\left[\sqrt{a}t\right] \\
&- \frac{\exp\left(\frac{1-4a\tau_{cool}t}{4a\tau_{cool}^2}\right)\tau_{cool}\,\mathrm{Erfc}\left[\frac{1-2a\tau_{cool}t}{2\sqrt{a}\tau_{cool}}\right]}{\tau_{cool} - \tau_{pol}} \\
&+ \frac{\exp\left(\frac{1-4a\tau_{pol}t}{4a\tau_{pol}^2}\right)\tau_{pol}\,\mathrm{Erfc}\left[\frac{1-2a\tau_{pol}t}{2\sqrt{a}\tau_{pol}}\right]}{\tau_{cool} - \tau_{pol}}
\end{aligned}
$$

where $a = 4\ln 2/w^2$ and w is the FWHM of the IRF, Erf the error function and Erfc the complementary error function.

Frequency-resolved photoconductivity measurements

In order to identify the relevant scattering mechanism, we use the Fourier transformation of measured THz signals to analyse the frequency-resolved conductivity of FAPbI$_3$ and MAPbI$_3$. figure 4.3A displays the frequency-resolved photoconductivity of MAPbI$_3$ for 160, 220 and 295 K measured between 0.5 and 2.2 THz after excitation at 400 nm. The real part of the photoconductivity is nearly flat, except of two dips in the response around 1 and 2 THz, the imaginary part is close to zero. For decreasing temperature, the magnitude of the photoconductivity increases, from 295 to 160 K around a factor of 2 in agreement with previously published studied. [Hut17, Mil15, Sav14, Weh14b, Oga14] The flat real component of the photoconductivity together with almost zero imaginary component of the photoconductivity (within our frequency range) is the signature of very short scattering time of charge carriers in the order of a few femtoseconds. The extracted photoconductivity spectra could be pictured as the Drude-like conductivity model overlapped

with two phonon modes at ~1 and ~2 THz. [Mil15, Weh14b] The phonon modes appear in the spectra due absorption of the THz pulse and the use of the thin film approximation for conductivity extraction which is fairly simplistic approach. [La15] To investigate these phonon modes, we performed THz-TDS without excitation at room temperature of both, FAPbI$_3$ and MAPbI$_3$, respectively (see figure 4.3A, lower panel). Using a standard Lorentz oscillator model, we are able fit the peaks of the frequency-resolved real conductivity. For MAPbI$_3$, we find relevant modes at 0.96 ± 0.01 and 1.89 ± 0.01 THz. For FAPbI$_3$, we find modes at 1.01 ± 0.02 and 1.94 ± 0.02 THz. The extracted frequencies agree with published values of the TO phonons and can be assigned to the Pb-I-Pb rocking mode (0.9 THz) and the Pb-I stretching mode (1.9 THz). [Miy17b, Iva17, Sen16, Mon17, Weh14b] The former phonon mode was also found to be related to the polaron formation by Miyata *et al.* [Miy17b] They proposed that a missing electron (hole) in the lattice is energetically stabilized (itself a signature of a polaron) due to structural relaxation of the lead-halide sub-lattice. Here, e is the fundamental charge, m_e^* effective mass (or band mass) of the charge carrier, N is the charge carrier density, ω the angular frequency of external field and τ_{scat} the scattering time. At room temperature, we obtain scattering time of 7.4 ± 1.7 fs for MAPbI$_3$ pumped at 400 nm and 4.5 ± 2.6 fs for MAPbI$_3$ pumped at 800 nm. In figure 4.4B, we show the ratio of the scattering times normalized to the scattering time at room temperature probed 2 ps after the photoexcitation for two different pump wavelengths (400 and 700 nm, corresponding to small and large excess energy) for both, FAPbI$_3$ and MAPbI$_3$, respectively. From 300 to 160 K, the photoconductivity and the scattering time increase for all the cases almost linearly. The increase of the scattering time is between a factor of 1.75 for FAPbI$_3$ pumped with 400 nm and 2 for MAPbI$_3$ when pumped with 700 nm. We can fit the frequency-resolved conductivity using the Drude model, which allows us to extract the scattering times:

$$\sigma_D = \frac{1}{1 - i\omega\tau_{scat}} \frac{Ne^2\tau_{scat}}{m_e^*}.$$

The conductivity is related to the temperature with a factor of $T^{-1.2}$. In addition to the influence of optical phonon scattering and the Rashba-effect, further scenarios were proposed to explain the temperature-dependent conductivity. La-o-vorakiat *et al.* proposed the influence of increasing disorder, especially with lower temperature close to the tetragonal-orthorhombic phase transition. [La15] Zhang *et al.* suggested the temperature dependence of the dielectric function as the origin of the derivation from T-1.5-dependence of the photoconductivity to the temperature. [Zha17a] Based on the derived scattering time, an effective free carrier mass of 0.15 m$_e$, the estimated carrier density of 10^{18} cm^{-3}, we estimate an upper boundary for the mobility of 78 cm^2/Vs.
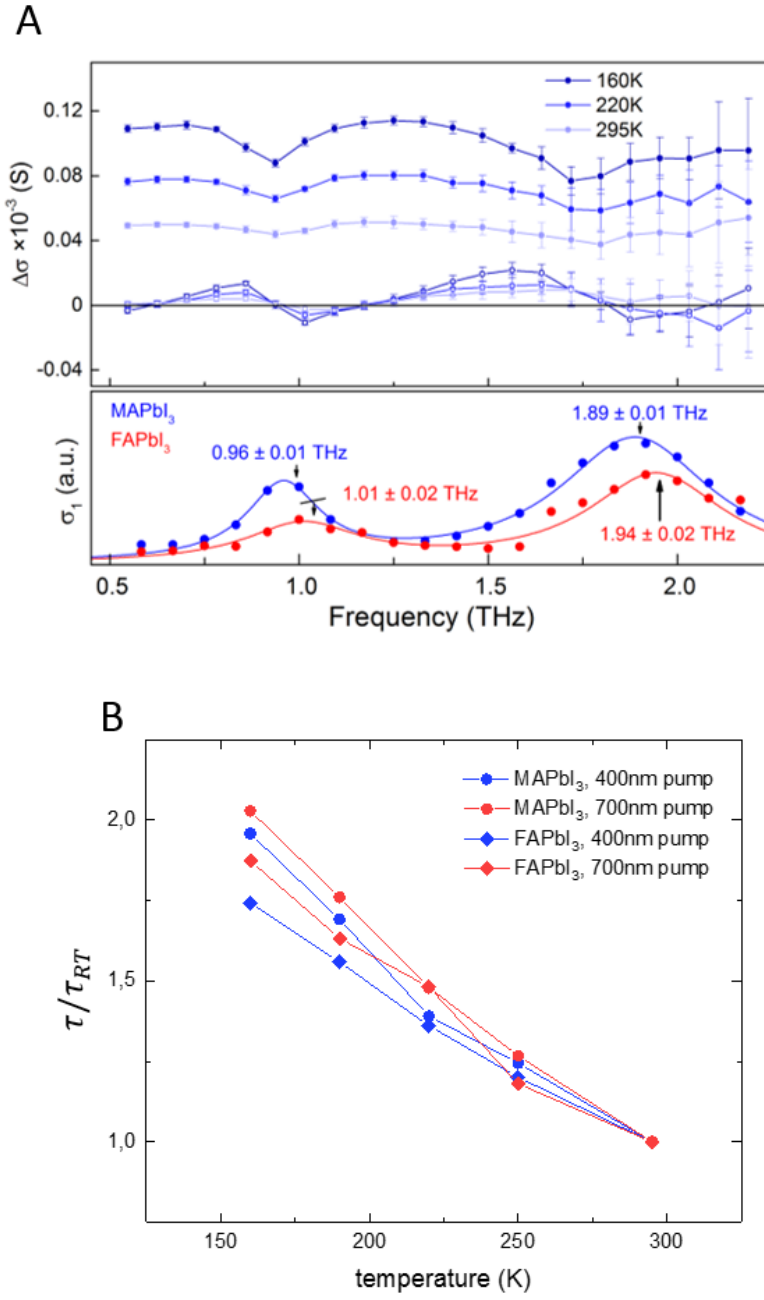
Figure 4.4.: Frequency-resolved THz time-domain spectroscopy data. (A) shows the transient frequency-resolved conductivity of MAPbI$_3$ measured at 160, 220 and 295 K between 0.5 and 2.2 THz after excitation at 400 nm. The data are recorded 2 ps after the photoexcitation. The steady-state real conductivity (full circles) is essentially flat with superimposed phonon modes around 1 and 1.8 THz (see lower panel), while the imaginary part (open circles) of the conductivity remains close to 0. The magnitude of the real conductivity increases by a factor of ~2 for decreasing the temperature from 295 to 160 K. The lower panel shows the frequency-resolved real conductivity of FAPbI$_3$ (red) and MAPbI$_3$ (blue) between 0.5 and 2.2 THz without excitation. The real conductivity of MAPbI$_3$ (blue) shows two peaks around 0.96 and 1.89 THz, using fitting with a Lorentzian functions. The real conductivity of FAPbI$_3$ (red) shows two peaks at 1.01 and 1.94 THz. (B) shows the temperature-dependent relative change of the scattering times τ_{scat} for temperatures between 160 and 295 K normalized to the scattering time at room temperature (see ESI). Both FAPbI$_3$ and MAPbI$_3$ show longer scattering times for lower temperatures, and the ratio of the scattering times varies between 1.75 for FAPbI$_3$ pumped at 400 nm and 2 for MAPbI$_3$ pumped at 700 nm.
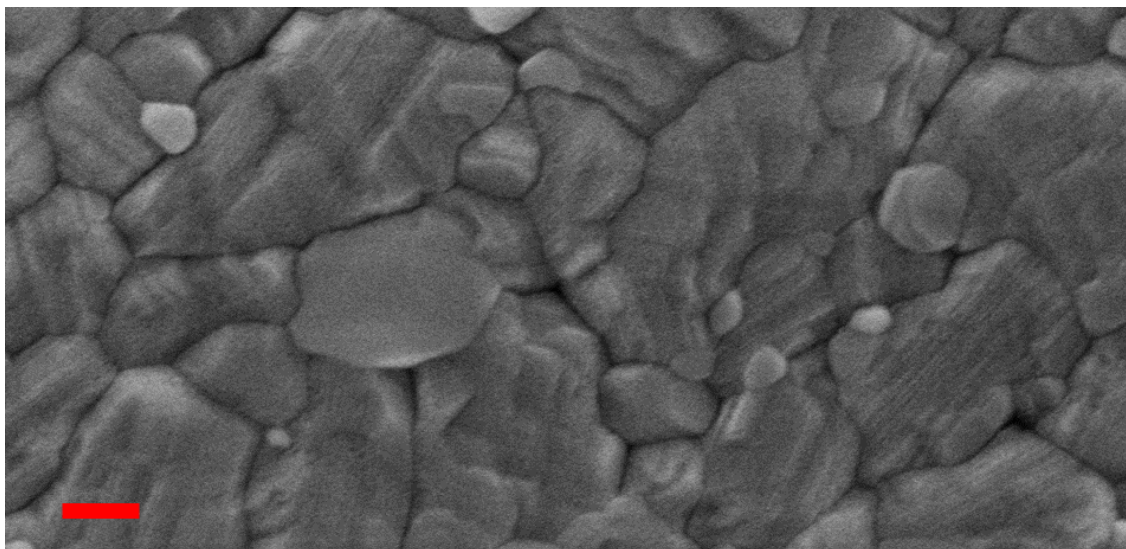

Figure 4.5.: Scanning electron microscopy image of a FAPbI$_3$ film, the scale bar is 200 nm.
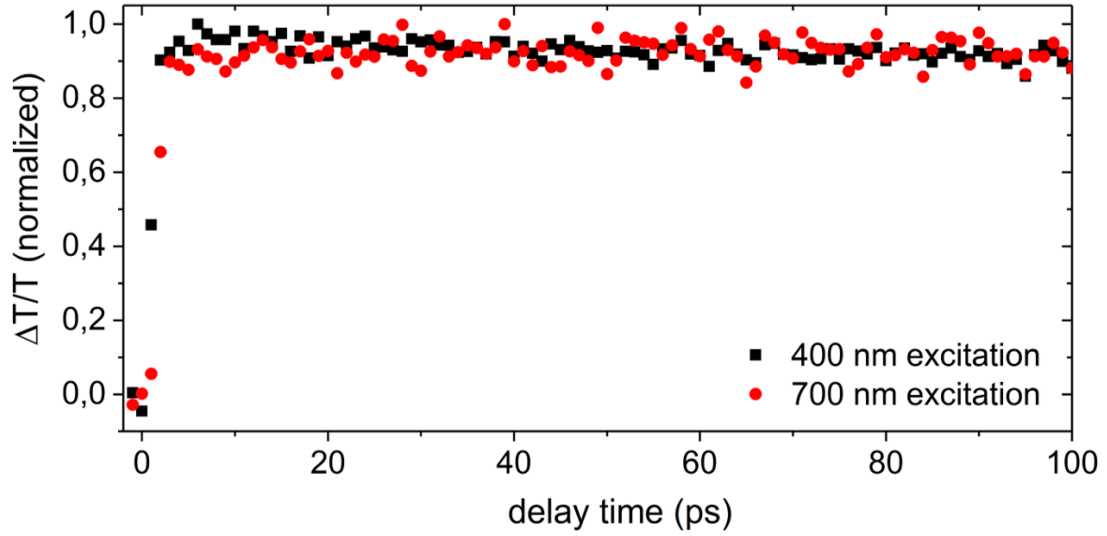
Figure 4.6.: Time-resolved photoconductivity measurements of MAPbI$_3$ at room temperature after excitation at 400 nm (black) and 700 nm (red). The photoconductivity increases within a few ps to the (normalized) maximum and does not decay significantly in the time window of 100 ps.
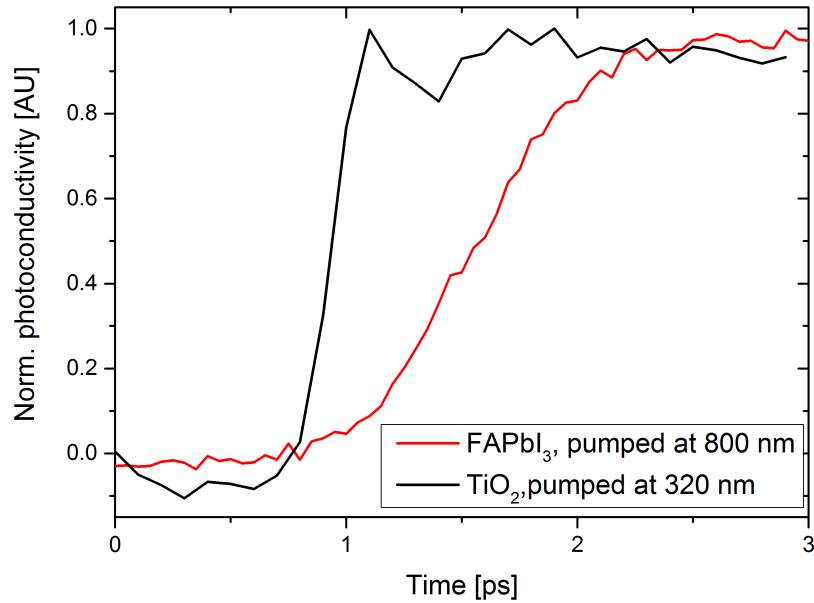

Figure 4.7.: Comparison of the rise of the photoconductivity for FAPbI$_3$ (red) and TiO2 (black). The photoconductivity of TiO$_2$ after excitation at 320 nm rises within 0.3 ps and was therefore used for the instrument response function. The photoconductivity of FAPbI$_3$ after excitation at 800 nm (resonant to the band gap) rises much slower, reaching its maximum after 1.5 ps.
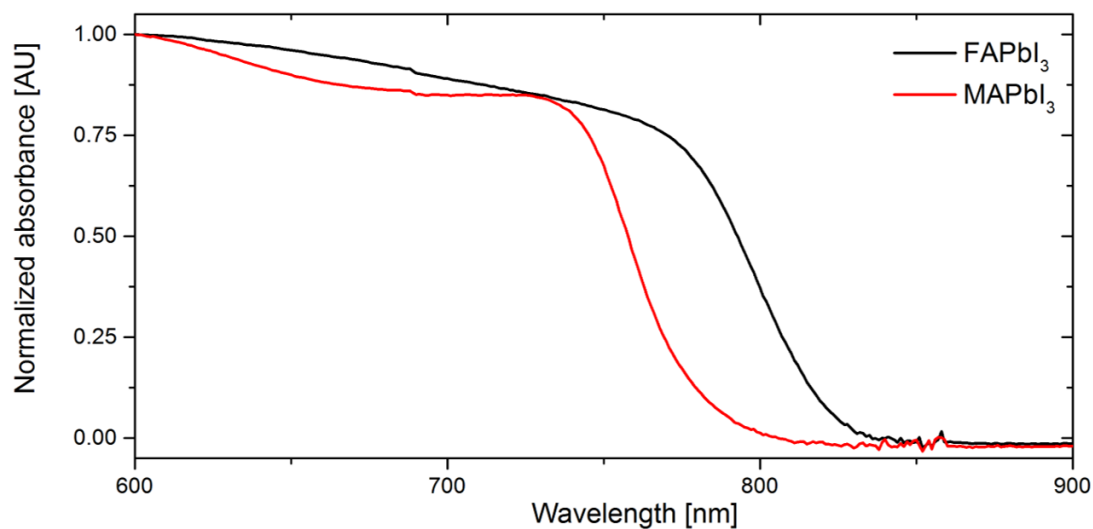
Figure 4.8.: Normalized UV/VIS Absorption measurements of MAPbI$_3$ (red) and FAPbI$_3$ (black). The samples of MAPbI$_3$ and FAPbI$_3$ show the characteristic increase of the absorbance for a wavelength shorter than the one which corresponds to the bandgap; 781 nm (1.58 eV) for MAPbI$_3$ and 824 nm (1.5 eV) for FAPbI$_3$.
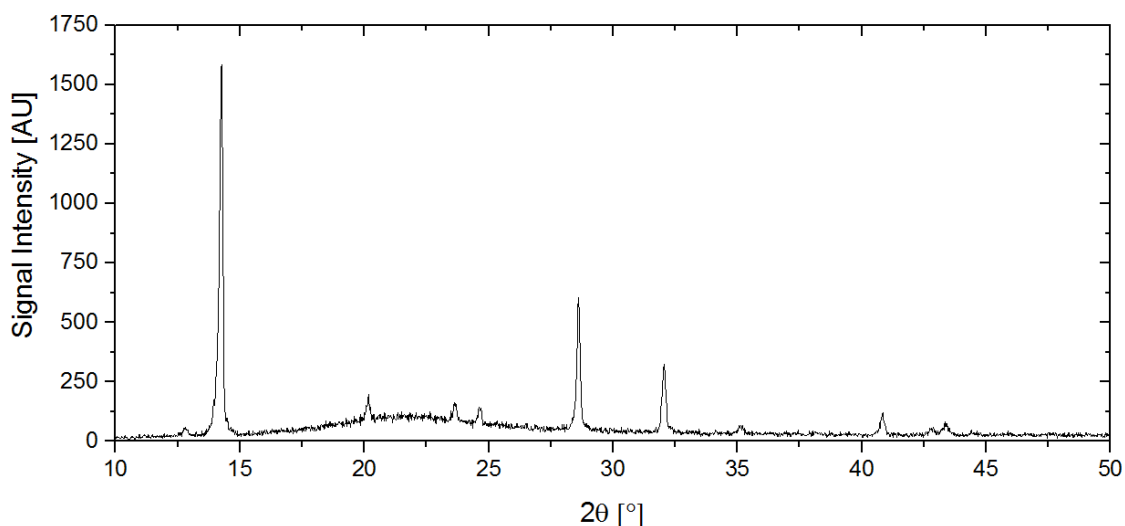

Figure 4.9.: X-Ray diffraction measurement of a MAPbI$_3$ film. The film shows peak at 14.26 and 28.5° which are associated with the 110 and 220 crystal orientation. The peak at 12.8° indicates trace amounts of lead-iodide in the sample.
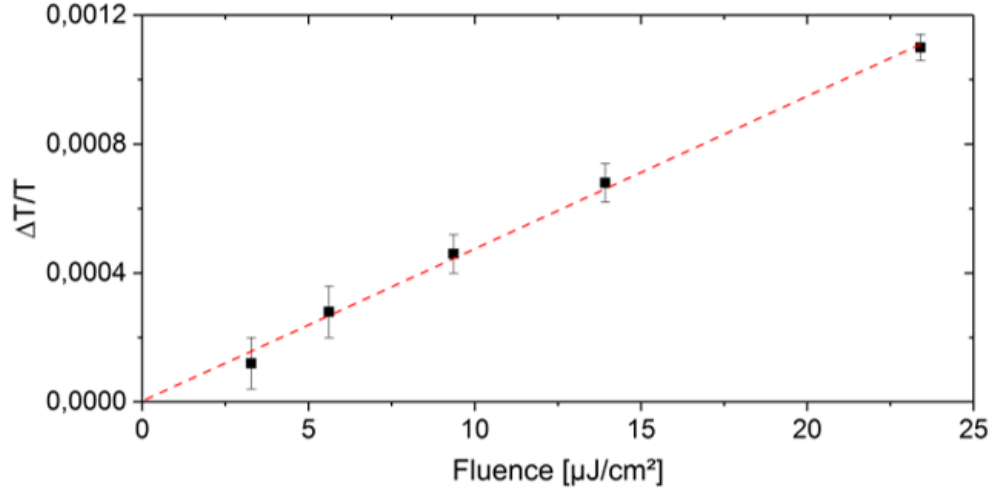
Figure 4.10.: Correlation of the signal of the photoconductivity measured 5 ps after the excitation for different pump power. The signal increases nearly linearly with the pump power; the measurements in the manuscript were taken at 5.6 μJ/cm^2. The line is to guide the eye.

Table 4.2.: Cooling times for FAPbI$_3$and MAPbI$_3$ obtained from the cooling rates, for different temperatures and excitation wavelengths.

FAPbI$_3$, T [K]	τ_{cool}, 700 nm [fs]	τ_{cool}, 550 nm [fs]	τ_{cool}, 400 nm [fs]
160	68$\pm$ 2	217$\pm$ 6	478$\pm$ 14
190	57$\pm$ 2	184$\pm$ 7	405$\pm$ 15
220	53$\pm$ 2	170$\pm$ 7	374$\pm$ 14
250	44$\pm$ 2	141$\pm$ 7	310$\pm$ 16
295	39$\pm$ 2	125$\pm$ 7	275$\pm$ 15

MAPbI$_3$, T [K]	τ_{cool}, 700 nm [fs]	τ_{cool}, 550 nm [fs]	τ_{cool}, 400 nm [fs]
160	48$\pm$2	214$\pm$8	506$\pm$19
190	42$\pm$2	188$\pm$9	445$\pm$20
220	36$\pm$2	160$\pm$8	379$\pm$20
250	37$\pm$2	165$\pm$8	389$\pm$20
295	30$\pm$2	134$\pm$9	316$\pm$20

5. Long Hot Carrier Lifetimes in Lead-Halide Perovskite Films

5.1. Trap-free hot carrier relaxation in lead-halide perovskite films

This following article was published in the Journal of Physical Chemistry C and is reprinted with permission from J. Phys. Chem. C, 2017, 121 (21), pp 11201 11206, Copyright (2017) American Chemical society.

5.1.1. Abstract

Photovoltaic devices that employ lead-halide perovskites as photoactive materials exhibit power conversion efficiencies of 22 %. One of the potential routes to go beyond the current efficiencies is to extract charge carriers that carry excess energy, that is, non-relaxed or *hot* carriers, before relaxation to the band minima is completed. Lead-halide perovskites have been demonstrated to exhibit hot-carrier relaxation times exceeding 100 picoseconds for both single- and polycrystalline samples. Here, we demonstrate, using a combined time-resolved photoluminescence and transient absorption study supported by basic modeling of the dynamics, that the decay of the high-energy part of the photoluminescence occurs on a timescale ($\sim$ 100 ps) very similar to the repopulation of the band minima when excited with a photon energy larger than 2.6 eV. The similarity between the two timescales indicates that the depopulation of hot states occurs without transient trapping of electrons or holes.

5.1.2. Introduction

Since organic-inorganic lead-halide perovskites were proposed for solar cell applications by Kojima *et al.* in 2009, the scientific community has witnessed great progress of both, device performance and fundamental understanding of the photophysical processes following

their photoexcitation. [Koj09, Lee12, Her16b, Str15b, Zha16b, Li17b, Bre14] However, although perovskite-based solar cells have now exceeded power conversion efficiencies of 21.5 %, some of their fundamental physical properties such as the nature of the band-gap and occurrence of ferroelectricity, are still under debate. [Sal16, Hut17, Aza16, Cho17, Her16a, Kut14, Tre17] Intense research has also been dedicated to study non-relaxed, hot, carriers in $CH_3NH_3PbI_3$ (MAPbI$_3$). In principle, reducing the losses associated with thermalization of hot carriers could allow the solar cell efficiency to surpass the Shockley-Queisser limit. In fact, if hot carriers could be extracted prior to their relaxation and recombination, then the maximum obtainable power conversion efficiency could theoretically be as high as 44%. [Gre03, Nie16c] For MAPbI$_3$, long-lived (≥ 50 ps) hot carriers have been reported in two pump fluence-dependent regimes: at high ($> 10^{18}$ cm^{-3}) charge carrier densities a *hot-phonon bottleneck* was observed that slows down cooling of hot carriers. The hot-phonon bottleneck originates from charge carrier reheating due to reabsorption of phonons. [Pri15, Yan15] At lower ($\leq 10^{17}$ cm^{-3}) charge carrier densities, high-energy photoluminescence originates from carriers that carry a large excess energy of up to 0.25 eV. This effect has been attributed to carrier screening resulting from the reorientation of the polar cations in the perovskite lattice. [Nie16c, Zhu16] Niesner *et al.* have reported a rise of the integrated signal intensity in time-resolved two-photon photoelectron (2-PPE) spectroscopy for more than 60 ps attributed to photoelectrons close to the conduction band minimum, in conjunction with a simultaneous decay of the intensity of high-energy photoelectrons. Manser and Flender *et al.* have observed a two-component decay of a population of hot carriers at ~2.5 eV using transient absorption spectroscopy. The fast, sub-ps component of this decay was attributed to relaxation of hot holes towards the band-minima. [Xin13] The slow component with a lifetime of ~50 ps was interpreted as slow thermalization of carriers from the M- to the Γ-point in the energy band structure of MAPbI$_3$. [Xin13, Fle15, Kaw15, Man14, Leg16, Ana16, Ama14, Guo17] Here, we investigate hot carrier dynamics in solution-processed polycrystalline MAPbI$_3$(Cl) perovskite films with lower excess energy (≤ 0.15 eV) by time-resolved photoluminescence (PL) and transient absorption (TA) spectroscopy. We find high-energy photoluminescence in solution-processed MAPbI$_3$(Cl) exhibiting a relaxation rate of 0.16 meV/ps for excess energies exceeding 0.15 eV when excited at 3.1 eV. We infer lifetime of 94 ± 13 ps for the spectrally-integrated fraction of the photoluminescence above energies of 1.7 eV. From TA experiments, the signal of the ground-state bleach (GSB) is observed to peak at 100 ± 5 ps when excited above 2.6 eV. The similarity of the timescales clearly indicates that the hot carrier thermalization occurs without transient trapping of charge carriers.

5.1.3. Methods

The perovskite samples were prepared in a nitrogen-filled glovebox with an oxygen level of < 1ppm. A 40 wt% solution of MAI (prepared following Lee *et al.*, see [Lee12]) and $PbCl_2$ (99.999% purity, Sigma Aldrich; dehydrated under high vacuum conditions) in anhydrous DMF (Sigma Aldrich) was spin-coated on fused silica for 60 s at 2000 rpm with a molar ration of 3:1 $MAI:PbCl_2$. After a room temperature annealing for 30 minutes, the samples were annealed at 100 °C for 60 minutes. The samples thickness (422 ± 26 nm) was measured using a KLA Tencor P16+ step profiler at six different positions of the sample. The samples were stored overnight prior to analysis. Transient absorption and photoluminescence measurements were performed under high vacuum conditions without any exposure to ambient conditions at 291 K. Time-resolved photoluminescence was measured with a C5680 Hamamatsu streak camera system following excitation at 400 nm from a frequency-doubled mode-locked titanium:sapphire amplifier (Coherent LIBRA HE, 3.5 mJ, 100 fs), either with a repetition rate of 1 kHz (10 ns time window; instrument response function 81 ps) or with a repetition rate of 80 MHz (2 ns time window; instrument response function 16 ps). Transient absorption experiments were carried out with a home-built pump-probe setup. The output of a titanium:sapphire amplifier was used to seed two independent optical parametric amplifiers (Coherent OPerA Solo), of which one was used to generate a pump pulse. The second OPA was used generate a seed pulse for supercontinuum generation, which served as the broadband probe pulse. For supercontinuum generation in the range of 550 - 1000 nm, a 1300 nm pulse was focused into a 3 mm c-cut sapphire crystal. Time resolution was obtained by delaying the pump pulses on a motorized delay stage between 300 fs and 8 ns with respect to the probe pulse. The transmission spectrum of the probe pulses was measured with a linear silicon photodiode array and successive probe pulses were used to determine the change in transmission induced by the pump pulse. Data collection and analysis were performed with home-built readout electronics and a LabView-based data acquisition and analysis software. UV/VIS measurements were performed using a Perkin Elmer UV/VIS/NIR spectrometer (Lambda 900) in a 150 mm integrating sphere with a spectral resolution of 1 nm. Scanning electron microscopy images were measured using a Zeiss LEO Gemini 1530.

5.1.4. Results and discussion

To investigate the dynamics of hot carriers in $MAPbI_3(Cl)$, we studied both the radiative recombination (via PL spectroscopy) and population dynamics of excited states (using TA spectroscopy).
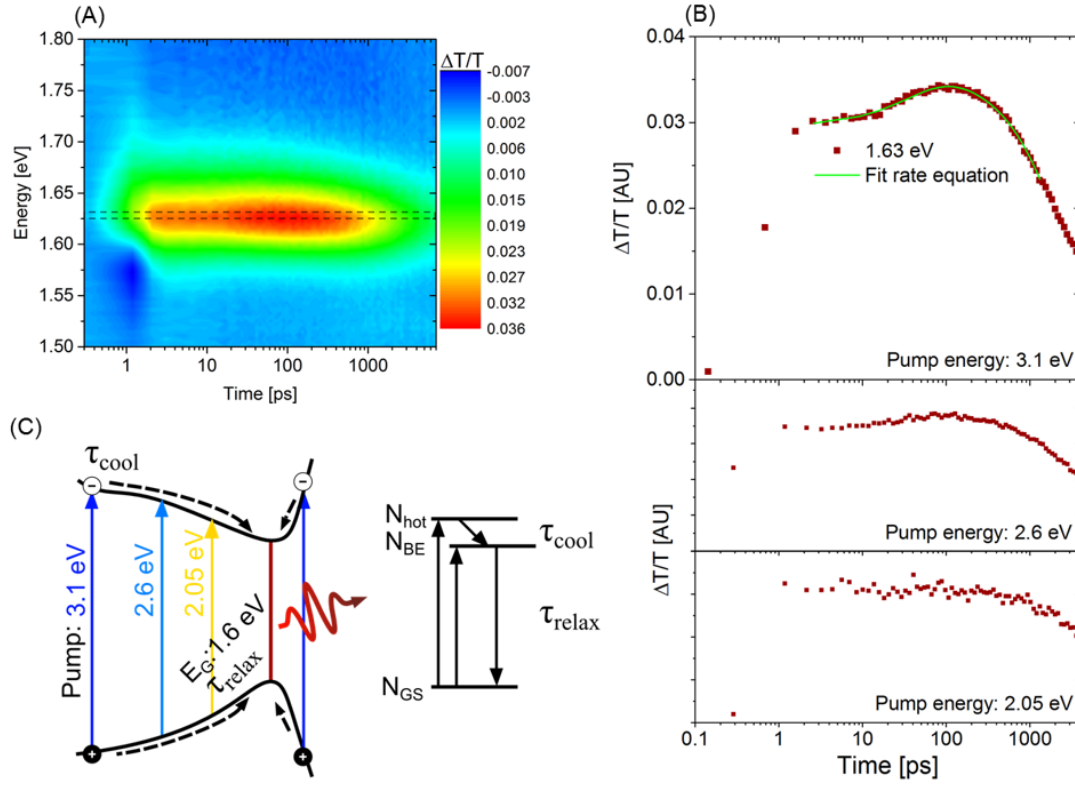
Figure 5.1.: Ps-ns transient absorption measurements on $MAPbI_3(Cl)$ films after excitation with a $\sim$150 fs pulse with a fluence of $2.5 \pm 0.25\ \mu J/cm^2$. (A) shows a contour plot of the transient absorption data after excitation at 3.1 eV. (B) shows the kinetics of the GSB probed at 1.63 ± 0.01 eV (brown, as indicated by the dashed box in (A)) for different pump photon energies. For a pump photon energy of 3.1 eV the maximum of the bleach increases by 11 % on a timescale of 100 ± 5 ps (upper panel). The fit obtained from the rate equation is shown in green (fitting parameters in the SI). For a pump photon energy of 2.6 eV (middle panel), the bleach increases similar to the case of excitation at 3.1 eV. For a pump photon energy of 2.05 eV (lower panel), no further growth of the bleach can be observed, the bleach remains flat for ~ 200 ps. (C) shows a scheme of the energy levels relevant to understand the TA measurements and the simplified three-level model used for the rate equations. The populations of the three energy levels (ground state, band edges and hot states) are denoted as N_{GS}, N_{BE} and N_{hot}; their respective lifetimes are τ_{relax} and τ_{cool}.

The samples were prepared by spin-coating MAI and $PbCl_2$ from solution in DMF on fused silica and subsequent thermal annealing in a nitrogen-filled glovebox. The preparation results in polycrystalline films with micrometer-sized crystals (compare figure 5.4) with a thickness of ~ 420 nm. Both, transient absorption and photoluminescence measurements were performed under high dynamic vacuum conditions ($p < 5\ 10^{-6}$ mbar) at 291 K. The occurrence of long-lived hot carriers was investigated using TA measurements

with excitation at 3.1, 2.6 and 2.05 eV with low (2.5 ± 0.25 μJ/cm^2) fluence. Fig. 5.1, (A) shows a false color two-dimensional map of TA measurement after excitation at 3.1 eV obtained at a fluence of 2.5 μJ/cm^2.

The broad feature centered at 1.63 eV is commonly assigned to the ground-state bleach (GSB) related to the transition between the valence band (VB) maximum and the conduction band (CB) minimum at the Γ-point in the energy band diagram. [Her16b, Gao16] The derivative-like feature between 1.5 and 1.6 eV at 1 ps, partially overlapping with the GSB, was previously assigned to photoinduced reflectivity changes. [Pri15] The high-energy tail above 1.7 eV, which exhibits a sub-ps lifetime, can be associated with a population of hot carriers. [Yan15, Pri15, Xin13] Kinetics extracted from the two-dimensional plot are shown in figure 5.1, (B). The integrated signal (probed at 1.63 ± 0.01 eV) rises within the instrument response time of ~1 ps to an amplitude of 0.03. Furthermore, the signal subsequently increases to a value of 0.034 within 100 ± 5 ps. The dynamics of the GSB after excitation at 2.6 eV show a similar trend. These results indicate that excitation at 3.1 eV and 2.6 eV leads to electrons and holes populating energetically high-lying states far from the VB maximum and CB minimum, as illustrated in figure 5.1, C. Relaxation from these high-lying states to the Γ-point leads to a rise in the TA signal at 1.63 eV. For excitation at 2.05 eV, the GSB signal does not show a subsequent increase but rather stays constant before the population decays. In order to quantify the energy-dependent kinetics of the GSB we approximate the kinetics using a simple three-level system, also shown in figure 5.1 1(C). The pump excites charge carriers from the ground to the excited states; an electron-hole pair is generated. We implemented the sub-ps carrier thermalization resulting in direct population of the band-edge state, N_{BE}. A fraction of the carriers does not undergo immediate thermalization, but forms a hot population, N_{hot}, relaxing to the band-edge state with a cooling time, τ. The band edge population, N_{BE} decays back to the ground state N_{GS} with a lifetime τ_{relax}. Neglecting the depletion of the hot state by hot PL, the resulting rate equations read:

$$\frac{dN_{GS}}{dt} = N_{BE}(t) \tag{5.1}$$

$$\frac{dN_{BE}}{dt} = \frac{1}{\tau_{cool}}N_{hot}(t) - \frac{1}{\tau_{relax}}N_{BE}(t) \tag{5.2}$$

$$\frac{dN_{hot}}{dt} = -\frac{1}{\tau_{cool}}N_{hot}(t) \tag{5.3}$$

$$1 = N_{BS}(t) + N_{BE}(t) + N_{hot}(t) \tag{5.4}$$

The GSB TA signal ΔT/T is proportional to $(1 - (N_{GS}(t) - N_{BE}(t)))$. Immediately after excitation, the initial conditions are $N_{hot}(t = 0) = \delta$ and $N_{hot}(t = 0) = \gamma$, with

$\gamma, \delta \ll 1$. The values for $\gamma, \delta, \tau_{relax}$ and τ_{cool} were adjusted to provide best description of the data between 2.5 and 1000 ps. The result is shown in figure 5.1, (B); the kinetics of the population of the band edges and hot population are shown in figure 5.5. The fit follows the bleach signal probed at 1.63 eV, peaking at 108 ps. Fitting to the rate equations resulted in a cooling time of the hot population of 40 ± 2 ps. For a fluence of 12.5 μJ/cm^2, the lifetime of the bleach bands is reduced as expected for fast non-geminate recombination due to the high initial charge carrier density (see figure 5.6). For a fluence of 39 μJ/cm^2, we observed signatures of a hot-phonon bottleneck (see figure 5.7) in agreement with previous results published measurements by Yang and Price *et al.*, confirming the equivalence of our results to previously published data. [Pri15, Yan15] In addition to the investigation of the population of excited states, which is accessible by TA spectroscopy, the radiative recombination of charge carriers was measured by time-resolved photoluminescence spectroscopy using the Streak Camera technique. Figure 5.2, (A) shows a false color two-dimensional plot of the photoluminescence measured over a time-window of 10 ns on a logarithmic intensity scale. The PL response is dominated by the band-edge emission centered at 1.59 eV. In addition to the band-edge emission, a high-energy tail is present between 1.7 and 1.85 eV. This tail of the PL does not originate from high signal intensities at short time scales, as evident from different normalized spectra (see figure 5.8, (B)). The high-energy tail appears to originate from photoluminescence of hot charge carriers, in agreement with previous reports by Zhu and Niesner *et al.* [Nie16c, Zhu16] To analyze the excess energy of the states from which the high-energy photon emission occurs, we performed a spectral deconvolution based on a global fit of the spectra between - 50 and 2500 ps relative to the maximum emission signal intensity. This procedure allows extraction of the excess energy with an effective carrier temperature, k$_B$T$_e$, based on the model proposed by Zhu *et al.* [Zhu16] After the initial charge carrier generation, the effective carrier temperature (compare figure 5.2, B) rises to 1780 ± 43 K, equivalent to an excess energy of 153 ± 4 meV. The initial decay of ~ 60 meV within 300 ps can be attributed to the decay of the high-energy photoluminescence. The relaxation rate for this decay is 0.16 ± 0.01 meV/ps, which is comparable to the values previously observed by Niesner *et al.* [Nie16c] For an estimate of the lifetime of the high energy photoluminescence, we compared the spectrally integrated total photoluminescence signal amplitude to the fraction of the photoluminescence signal above 1.7 eV (compare figure 5.8, C). We fit the signal decay with a single exponential function and obtained lifetime of 94 ± 13 ps. For the photoluminescence signal probed at 1.7 eV (see figure 5.8, D), we obtained a lifetime of 117 ± 10 ps.

For comparison, the fast decay of the initial *hot* effective carrier temperatures k$_B$T$_e$ has a half-life of $\sim$140 ps. It should be noted that the amount of excess energy also depends
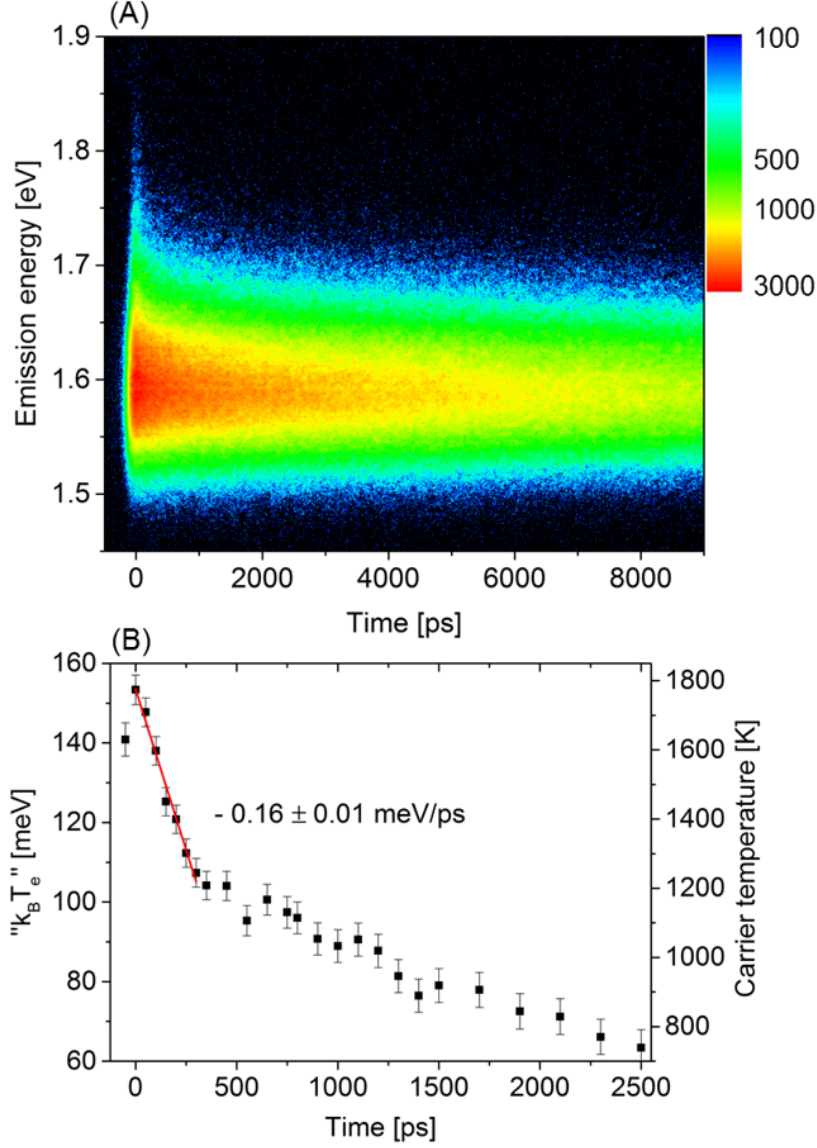
Figure 5.2.: Time-resolved photoluminescence measurements on MAPbI$_3$(Cl) films after excitation with a 100 fs pulse at 3.1 eV with a fluence of 2.5 μJ/cm^2. (A) shows the photoluminescence contour plot. The high energy tail is associated with the recombination of non-relaxed, *hot*, charge carriers visible at early timescales. (B) shows the temporal evolution (carrier cooling) of the excess energy/effective carrier temperatures k$_B$T$_e$ obtained from a global fit of the data according to a model proposed by Zhu19. The lifetime of the initial fast decay was approximated by a linear fit (red solid line) with a slope of -0.16 $\pm$ 0.01 meV/ps.

on the position of the quasi Fermi levels. This increases the uncertainty of the value we determine, but not necessarily for the dynamics of the decay of the excess energy. [Nie16c, Kaw15, End16b] The very similar timescales of the decay of the high-energy

photoluminescence ($\sim$ 100 - 140 ps) and the bleach signal reaching completion ($\sim$ 100 ps, with a $\sim$ 40 ps rise time) point to both effects sharing the same physical origin. The appearance of the ground state population virtually in parallel with the decay of the high-energy photoluminescence, points to direct relaxation from high-energy states to the Γ-point. If hot charge carriers underwent transient trapping while relaxing to the band edges, the band edge population would not rise as quickly as observed, but instead the buildup would take even longer. Furthermore, it is also questionable whether, in such a case, the simple three-level model would still provide an adequate description of the dynamics, as it does in our experiments. [Smi15] We attribute the slight red-shift of the GSB after 100 ps to a (although weak) signature of a dynamic Burstein-Moss-shift. [Yan15, Pri15, Man14] The photon energy-dependent TA measurements allow assumptions about the origin of the hot carriers. The delayed population of the ground state can be observed for excitation above 2.6 eV, but not for excitation at 2.05 eV, where it replicates published dynamics of perovskites films prepared from lead-chloride. [Che14, Tri15] Due to the limited probe range in our TA measurement we cannot probe the origin of the hot carriers directly. A tentative proposition for the origin of the hot carriers based on the photon energy-dependent TA measurements suggests a long-lived population at the M-point of the Brillouin zone. [Her16b, Fle15, Man14, Leg16, Ana16] Niesner *et al.* have shown a decay of the intensity of photoelectrons with an excess energy of $\sim$0.25 eV and a subsequent increase of the photoelectron intensity associated with a population close to the Fermi energy on a similar timescale as in our TA measurements. As such, our results validate those conclusions, but there are some notable differences between the experiments: TA measurements described above probe the bulk sample in transmission, and were carried out at room temperature, rather than being surface sensitive as 2-PPE spectroscopy and being measured at 190 K. 2-PPE also is sensitive to photoelectrons only, whereas TA probes both electrons and holes. Furthermore, a recently study by Guo *et al.* using spatially-resolved and pump-photon energy dependent transient absorption spectroscopy on MAPbI$_3$ films showed a similar slow rise of the GSB signal for a pump photon energy of 3.14 eV, while it was absent for a pump photon energy of 1.68 eV in excellent agreement with our data presented in figure 5.1. [Guo17] In fact, Guo *et al.* provide clear evidence for quasi-ballistic transport of hot charge carriers, which supports our conclusion that trapping effects are negligible for hot carriers excited with pump photon energies above 2.6 eV. The high-energy photoluminescence also originates from the hot carrier population. The exact mechanism of the high-energy photoluminescence itself is still under debate. Wehrenfennig *et al.* have proposed dynamic spectral broadening due to carrier-phonon interaction. [Weh14d] Chang *et al.* have proposed a transient change of the recombination rates with a characteristic timescale of $<$ 80 ps resulting from the emission of high-energy phonons (of the MA cations) and subsequent phonon-phonon

coupling. [Cha16] A transient change of the recombination rate caused by a long-lived population of hot carriers in combination with excitation of MA phonon modes could also explain the absence of a bleach signal in the TA measurements associated with the high-energy photoluminescence. In fact, it would also explain the lack of high-energy photoluminescence from $CsPbI_3$ as reported by Zhu *et al.* [Zhu16] Different mechanisms could contribute to the rise of the GSB, including interband relaxation from a higher-lying conduction band to the lowest-energy conduction band and/or intervalley scattering. [Her16b, Nie16c, Xin13, Ana16] To better understand the origin of the various hot carrier processes, additional experiments are clearly required; specifically, the question whether polarons, as proposed by Zhu *et al.* [Zhu15b] are responsible for the low carrier scattering rates or whether a proposed spin-split indirect band gap can explain the remarkable hot carrier properties. [Hut17, Aza16, Fro16a]

5.1.5. Conclusions

In conclusion, we report high-energy photoluminescence and long-lived hot charge carriers in polycrystalline solution-processed $MAPbI_3(Cl)$ films similar to previous reports on co-evaporated $MAPbI_3$ and $MAPbBr_3$ single crystals. [Nie16c, Zhu16] Our results suggest that the high-energy photoluminescence, which exhibits an excess energy of up to 0.15 eV, is correlated with a delayed population of the band edges with charge carriers after excitation with a photon energy larger than 2.6 eV. The similar timescales of the hot carrier relaxation and the increased population of the band edges indicate a direct depopulation of hot states without transient trapping of charge carriers during the cooling process.

5.1.6. Acknowledgments

5.1.7. Supporting information

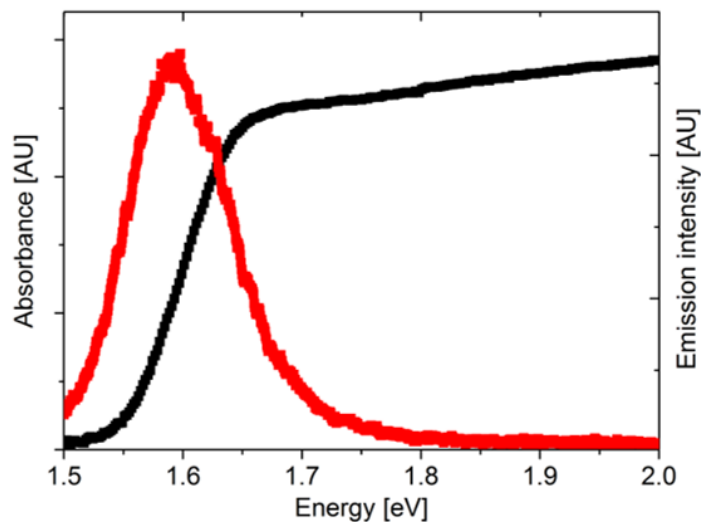
Figure 5.3.: Optical characterization of the MAPbI$_3$(Cl) sample for the measurement: absorbance shown in black, integrated emission shown in red.
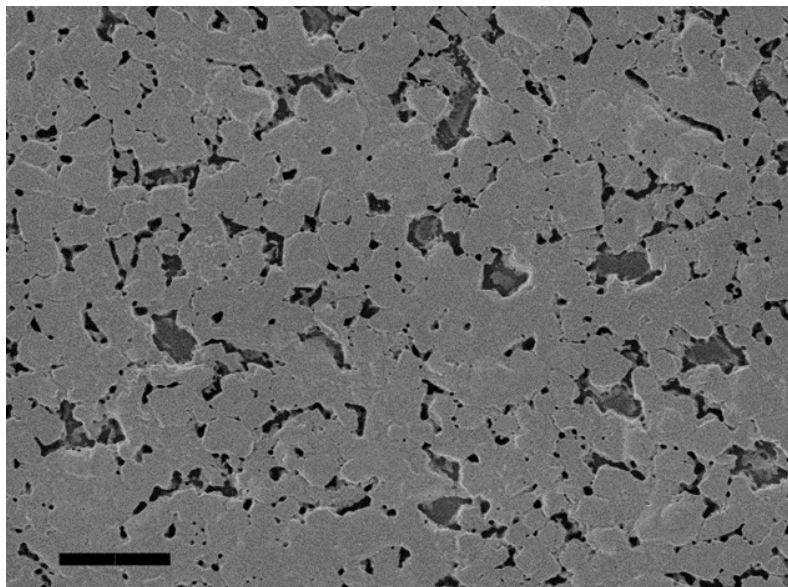

Figure 5.4.: Scanning-electron microscopy of the MAPbI$_3$(Cl) sample for the measurement. The scale bar is 2 μm.
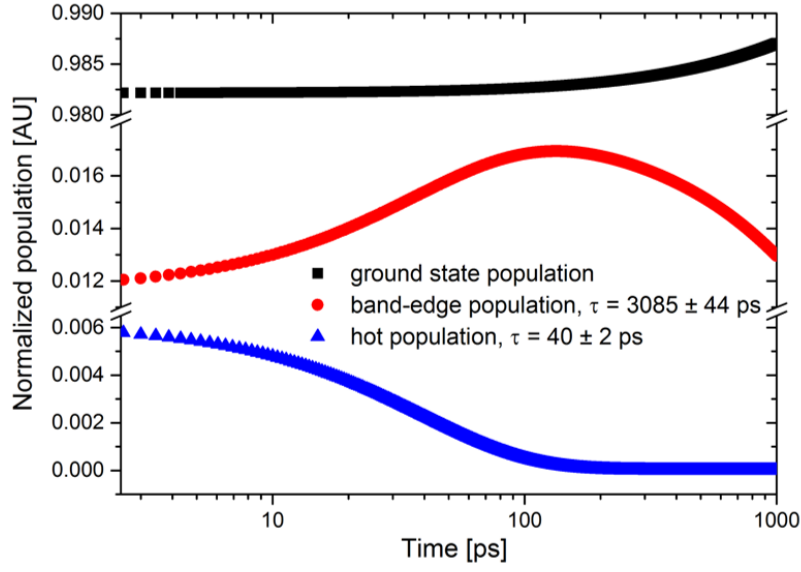
Figure 5.5.: Population of the ground state, the band edges and the hot state obtained from the fitting of the three-level rate equation.
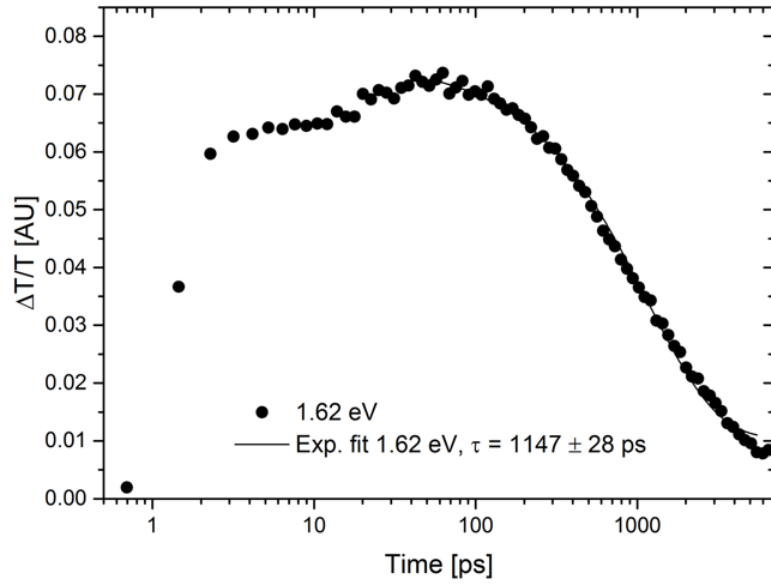

Figure 5.6.: Ultrafast transient absorption measurements $MAPbI_3(Cl)$ after excitation with a 150 fs pulse at 3.1 eV for a fluence of 12.5 $\mu J/cm^2$. The bleach probed at 1.62 eV shows the delayed rise with a peak at ~ 60 ps. The decay was fitted with a single exponential function; the lifetime is 1147 ± 28 ps for the signal at 1.62 eV.

The parameters of the fit shown in 5.1, C are

$\tau_{relax} = 3085 \pm 44$ ps

$\tau_{cool} = 40.1 \pm 1.8$ ps

$\gamma = 0.012 \pm 9.6 \cdot 10^{-5}$ and
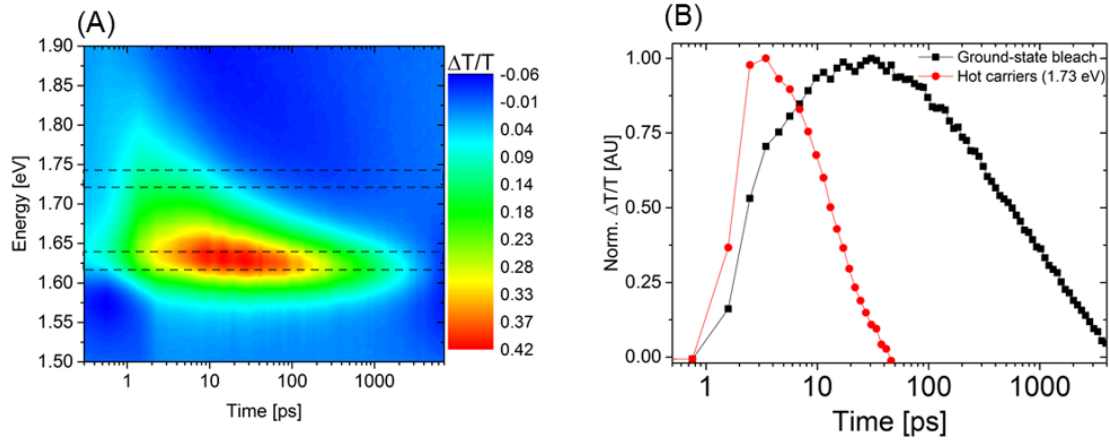
$\delta = 0.0058 \pm 1.1 \cdot 10^{-4}$

Figure 5.7.: Ultrafast transient absorption measurements of MAPbI$_3$(Cl) after excitation with a $\sim$150 fs pulse at 3.1 eV for a fluence of 39 μJ/cm^2. (A) shows the false color two-dimensional transient absorption data for a pump fluence. It shows the same sub-ps feature as in Fig. 2a, but a much broader high-energy tail extending towards 1.9 eV and the ground-state bleach with stronger red-shift (0.02 eV between 1 ps and 1 ns). Both features have been associated with the hot-phonon bottleneck. [Yan15] (B) shows the comparison of the kinetics of the ground-state bleach (black) and of the hot carriers, probed at 1.73 eV; indicated by the dashed boxes in (A). The hot carriers decay exponentially with a time constant of $\tau = 15.57 \pm 0.55$ ps, on a similar timescale to the ingrowth of the peak of the ground-state bleach. For the high fluence measurement, similar timescales were extracted for the delayed rise of the GSB signal (23 $\pm$ 3 ps) and the decay of the hot carriers (probed at 1.7 eV: $\tau = 15.6 \pm 0.6$ ps). Compared to the low-fluence measurement, the high-energy tail (see figure 5.6, A) becomes much more prominent. The similar timescale of the decay of hot carriers and the rise of the GSB, in combination with the spectral narrowing over time and the substantial redshift, indicates a hot-phonon bottleneck. This interpretation is in line with that by Yang et al. and Price et al. [Pri15, Yan15] They attributed the delayed rise of the GSB to spectral narrowing of the bleach signal, which, for a slowly decaying population, will result in an increase of the bleach signal. [Yan15] The increased carrier density enhances bimolecular- and Auger recombination, and accordingly, the overall lifetime of the GSB is significantly reduced, evident also from the kinetics shown in above. [Her16b]
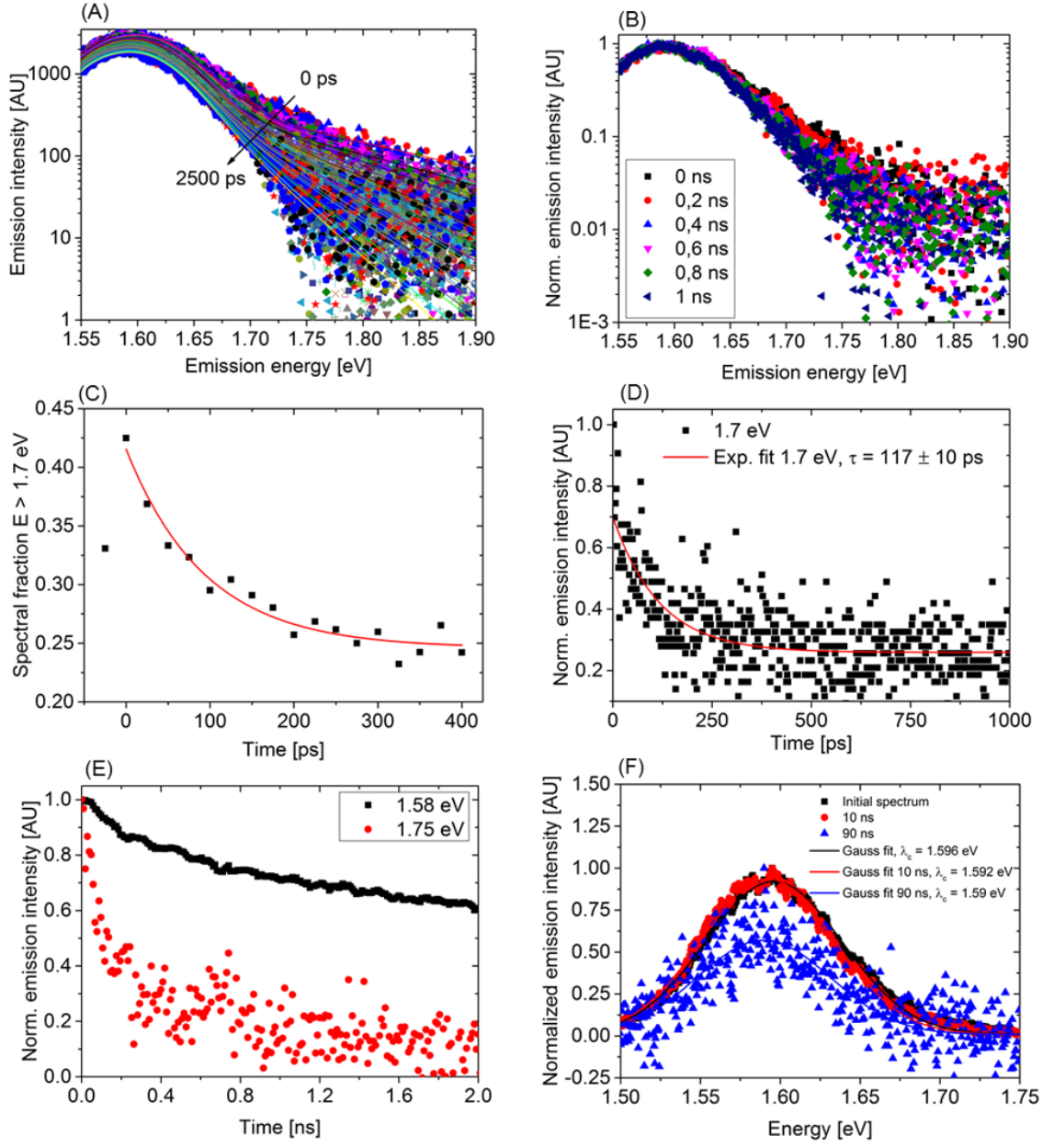
Figure 5.8.: Time-resolved photoluminescence measurements of MAPbI$_3$(Cl) measured at a fluence of 2.5 μJ/cm^2 after excitation with a 100 fs pulse at 400 nm. (A) shows the temporal evolution of the emission peak between 0 and 1500 ns and the associated global fits based on the model proposed by Zhu. [Zhu16] (B) shows the normalized emission spectra between 0 and 1 ns. The high-energy tail is still observable in normalized intensity. (C) shows the fraction of the spectrally integrated fraction of the high-energy photoluminescence above 1.7 eV and the photoluminescence originating from band-to-band transition. The signal fraction rises with the emission signal up to 0.42 before it decays within 400 ps. A fit of the decay with a single exponential function reveals a lifetime of 94 $\pm$ 13 ps. The background of the signal (0.25) is substantial; we attribute the background to the relatively low signal-to-noise ratio obtained above 1.7 eV, which is why we use 1.7 eV as limit of the hot emission. (D) shows the linear kinetics and a single-exponential fit for the hot photoluminescence at 1.7 eV ($\tau = 117 \pm 10$ ps) measured in a time-window of 2 ns and an instrument response function of 16 ps. (E) shows the linear kinetics for band-edge and hot photoluminescence. In comparison to Chang et al., the amplitude of the sub-100 ps emission is much smaller than the 50% mentioned. [Cha16] (F) shows the normalized spectrum at t = 0, 10 and 90 ns. We do not observe a significant red-shift ($\leq$ 6 meV), suggestion limited effects of vertical carrier diffusion affecting our conclusions. [Zhu16, PO16, Nie16c]
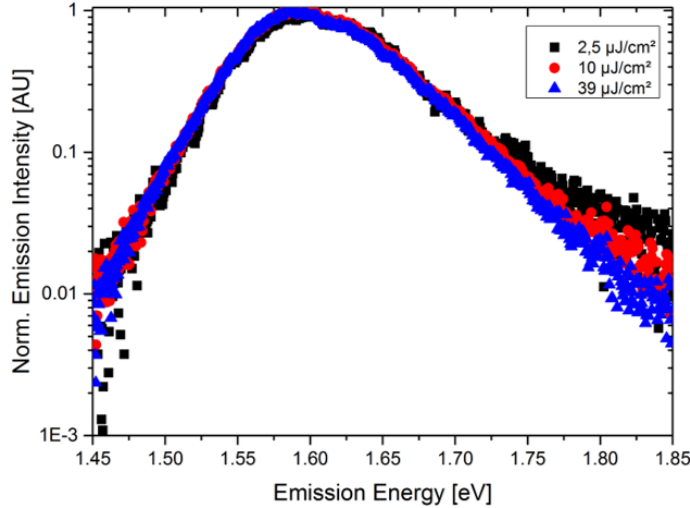

Figure 5.9.: Intensity-dependent time-resolved photoluminescence spectra of MAPbI$_3$(Cl). The fluence was increased from μJ/cm^2 to μJ/cm^2, resulting in a reduction of the high-energy tail of the photoluminescence. [Zhu16, Nie16c]

5.2. Ultra long hot carrier lifetimes in lead-iodide perovskites

In addition to the results presented in section 5.1, another sample showed similar qualitative properties. However, the ground state bleach was observed to reach its maximum after more than 500 picoseconds.
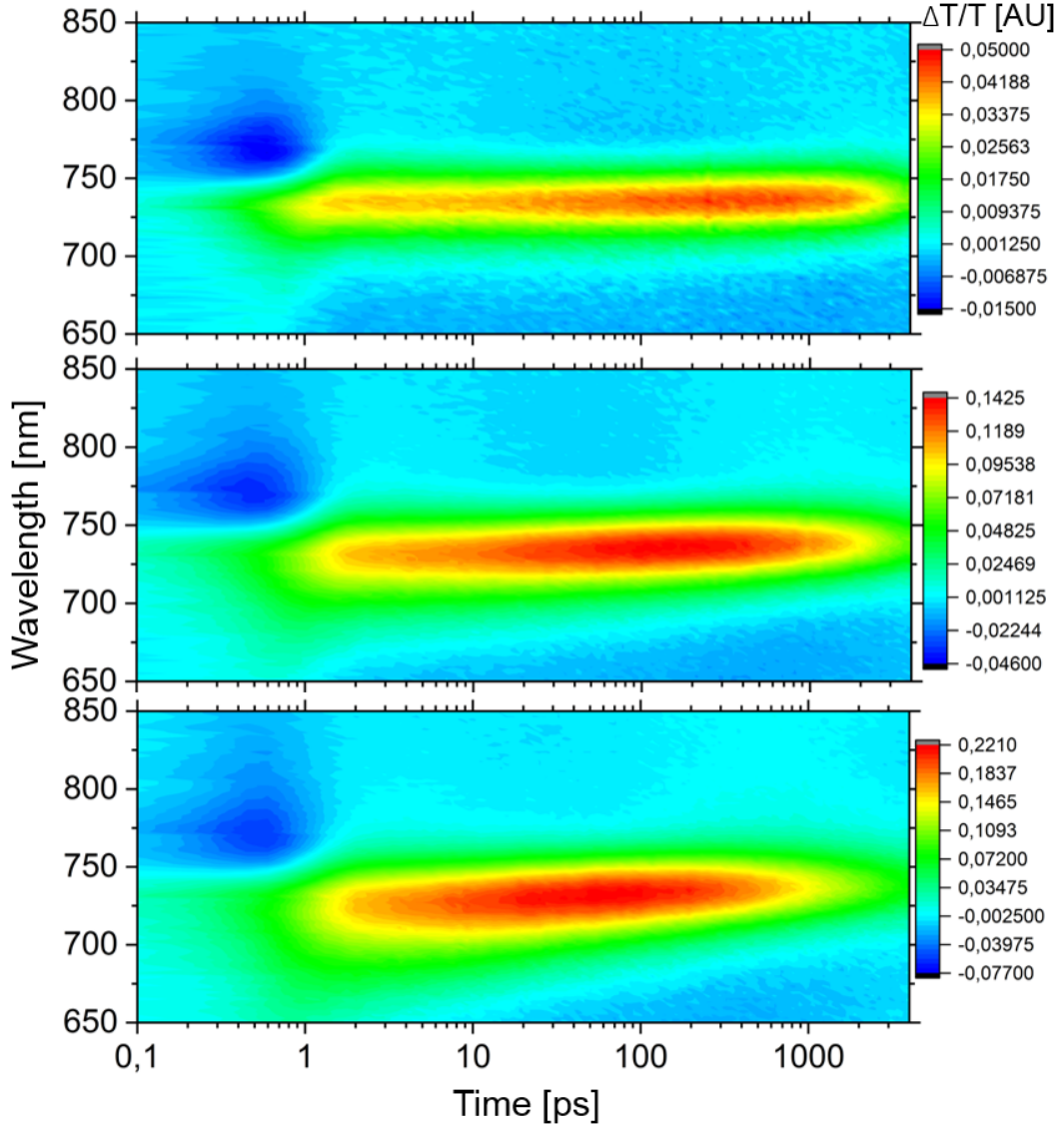

Figure 5.10.: Transient absorption measurements of an MAPbI$_3$(Cl) sample after excitation with an $\sim$ 150 fs pulse with a wavelength of 400 nm for fluences of 3 (top), 16 (middle) and 39 μJ/cm^2 (bottom).

The corresponding lifetime of the hot emission was in the nanosecond timescale. The sample prepared from CH_3NH_3 and $PbCl_2$ to form $CH_3NH_3PbI_3(Cl)$ was investigated using fluence-dependent ultrafast transient absorption spectroscopy. Measurements with fluences of 3, 16 and 39 $\mu J/cm^2$ are shown in Fig. 5.10. For all measured fluences, two distinct spectral features can be observed: the ground state bleach with fluence-dependent dynamics centered around 730 nm and the fluence-dependent short -wavelength tail below 700 nm associated with hot carrier cooling. For the measurement with a fluence of 39 $\mu J/cm^2$, one can observe the signatures of a hot-phonon bottleneck: a temporal coincidence of the reduction of the short-wavelength tail and the maximum of the ground state bleach. [Pri15, Yan15] In contrast to results published by Yang *et al.* and Price *et al.*, the ground state bleach reaches its maximum around 60 ps pump-probe delay rather than at 20 ps, but with a similar high energy tail extending to 625 nm. [Pri15, Yan15] When exciting with gradually lower fluence, a transition from the hot-phonon bottleneck to the delayed rise of the ground-state bleach can be observed. When the sample is excited with 3 $\mu J/cm^2$, the ground state bleach reaches its maximum at 600 ps but without the short-wavelength tail, indicating a different cooling regime. In contrast to the observations in section 5.1, the ground state bleach reaches its peak at 600 ps for comparable fluence. For the lowest fluence, the peak ground state bleach increases by $\sim$ 40 % in intensity. This indicates that also a significantly higher fraction of charge carriers is excited to the long-living hot state, much more in comparison to the results published in section 5.1. For the fluence of 16 $\mu J/cm^2$, a combination of the long-living hot state and the energetic onset of the hot-phonon bottleneck would be expected. The high-energy tail is depleted much earlier than the ground state bleach reaches its maximum, but one can observe a redshift of the ground state bleach. The redshift is commonly associated with the hot-phonon bottleneck due to the cooling and the corresponding band-gap renormalization. [Pri15, Yan15] The redshift is superimposed with the delayed peak of the ground state bleach due to the long living hot state.

To study not just the population of states close to the band edges, but also the emission related to the cooling of hot carriers, the emission was measured using ultrafast photoluminescence spectroscopy (see Fig. 5.11). The sample was excited at 400 nm, the emission was observed with the streak camera system (100 ns time range, resulting in an instrument response function of $\sim$0.8 ns). The band edge emission is centered at 780 nm and shows a spectrally homogeneous decay. At shorter wavelengths compared to the band edge emission, one can observe an additional emission signal between 655 nm and 710 nm, 125 nm less than the characteristic band edge emission wavelength. The hot emission is highlighted in panel B of figure 5.11. It is apparent that the hot emission starts to decay within one nanosecond, comparable to the timescale of the instrument response function.
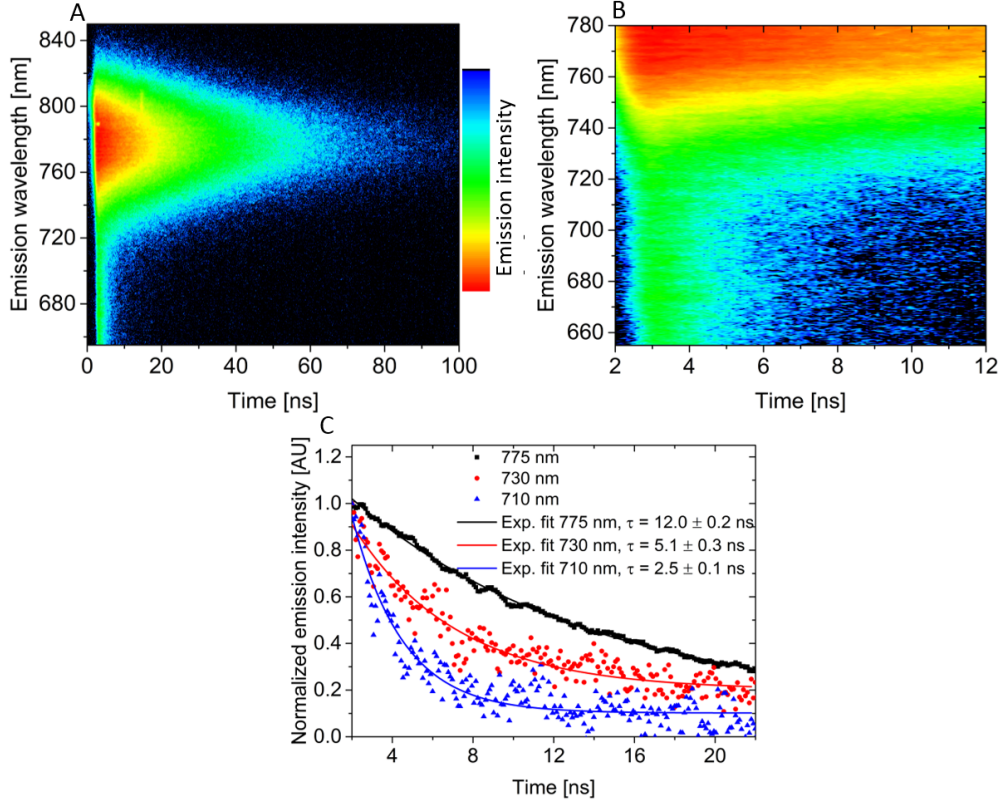
Figure 5.11.: Photoluminescence measurements of a $CH_3NH_3PbI_3(Cl)$ sample after excitation with a ~ 150 fs pulse with a wavelength of 400 nm for a fluence of 1 $\mu J/cm^2$. Panel A shows a contour plot of the measurement, the short-wavelength tail associated with the recombination of hot charge carriers is apparent at early time scales; panel B shows the hot emission in more dynamic detail. Panel c shows the recombination dynamics probed at 775, 730 and 710 nm, each with an average of $\pm$ 0.63 nm. A shorter lifetime is observed with lower probe wavelength.

In figure 5.11, panel C, the dynamics of the band edge and hot emission probed at 730 and 710 nm are compared. The emission from the band-edges can be fitted with a single exponential function, resulting in a lifetime of 12 ± 0.2 ns. The lifetime decreases to 5.1 ± 0.3 ns when probed at 730 nm (1.7 eV) and to 2.5 ± 0.1 ns when probed at 710 nm (1.75 eV). The lifetime probed at 710 nm exceed the lifetimes reported in section 5.1 by a factor of ~ 25.

Numerous attempts have been made to explain the long lifetimes of hot states and the origin of the hot emission. Possible explanations of the former include the electronic band structure of the lead-halide perovskite itself, electron-phonon interaction (polaron formation) and transient trap states in the conduction band. [Dem16, Zhu15b, Yin14b] The electronic band structure of lead-halide perovskite allows multiple transitions after

excitation at 3.1 eV, either between the valence and conduction band in the Γ-Valley or around the M-point, where a transition energy 2.5 - 2.7 eV was proposed by Demchenko *et al.* Additional transitions are possible around the Γ-point, but from lower or to higher-energetic bands. [Her16b, Dem16] Several groups have reported a population of charge carriers with a long lifetime and similar transition energies to the ones at the M-point (2.4 - 2.6 eV, < 100 ps lifetime) and with slightly higher energy (2.5 - 2.7 eV, > 100 ps lifetime). These populations can be associated with a transition from the band minima to a lower/higher energetic band. [App17b, Man14, Tri15] As indicated in section 2.5, the highest transition probabilities compared to the transition to a different conduction band are expected around the M-point.

A tentative assignment of the transition would associate the population at 2.5 eV with the M-point and the more energetic transition with a second conduction band. The actual origin of the long lifetime of carriers is still being discussed, but the large momentum mismatch between the M-point and the Γ-point and the ultra-low thermal conductivity of the lattice can certainly play a role for the exact mechanism. [Pis14, App17b]

The formation of polarons is another concept that has been introduced in order to explain the long-living excited states measured in lead-halide perovskites and is discussed in detail in chapter 4. Here we provide a short overview of the mechanism. After photoexcitation, non-equilibrium carriers are generated. Due to carrier-carrier interaction, the excess energy of the hot carriers will follow a Boltzmann distribution after ∼ 100 fs (thermalization). Due to the interaction of (thermalized) charge carriers and phonons in a polar lattice, a polaron is formed. The effective mass of the polaron is ∼ 1/3 larger compared to the bare free electron in the perovskite. [Fro17a] One putative consequence of the polaron formation is reduced scattering of charge carriers and phonons in comparison to bare charge carriers. Scattering of charge carriers and phonons is a limiting factor to the recombination of charge carriers and hot carrier lifetime. [Mil15, Zhu15b] The formation of a polaron prior to carrier cooling will result in a longer hot carrier lifetimes.[Ric17] In addition to the reduced scattering, the localization of electron and hole polarons was proposed to occur in spatially separated regions, which would reduce the recombination further. [Iva17, Miy17b, Amb18]

It has recently been proposed that the hot emission from lead-halide perovskite is related to the organic cation. Specifically, Chang *et al.* have proposed that the sub-ns recombination is associated with the excitation of high-energy phonon modes associated with the MA-cations. [Cha16] For hot emission occurring in MAPbBr$_3$, it has been proposed that the reorientation dynamics of the MA-cations leads to different local structures with larger or smaller band gaps. [Zha17b] The smaller bandgap structure features polaron-like charge localization with low overlap of the electron and hole wave function,

i.e. slower recombination and were associated with the band edge emission. The higher energy structure (energetic difference 0.3 eV) was associated with delocalized charges with a larger overlap of the electron and hole wave function, i.e. faster recombination. The high-energy emission was related to the hot emission.

The delayed peak of the ground state bleach at $\sim$ 600 ps can be attributed to an ultra-long-lived population of hot carriers. If the hot emission is actually related to the cooling of hot carriers (LO-phonon emission and subsequent coupling of LO phonons to high-energy phonons related to the organic cation), than the nanosecond hot emission lifetimes cannot be explained by cooling alone. The discrepancy of the timescales of cooling and emission is in striking contrast to section 5.1, where the time scale of cooling and emission vary by 20% rather than at least a factor of four for the measurements discussed above. An additional contribution might therefore arise from transient trapping and de-trapping of charge carriers. The majority of the defects, such as iodine vacancies and interstitials, are located in the proximity of the band edges within the band gap. However some, e.g. MA, vacancies are located in the valence band. [Yin14a] Due to the large excess energy of the carriers, de-trapping on a ps timescale and subsequent relaxation to the band edges is possible and could explain both, the increase of the population of the band-edges and the delayed, high-energetic photoluminescence.

In conclusion, the cooling of hot carriers and hot emission of $MAPbI_3(Cl)$ films was investigated using transient absorption and time-resolved photoluminescence measurements. The delayed rise of the ground state bleach can be associated with the slow cooling of excited carriers. On a slightly longer timescale compared to the rise of the ground state bleach, hot emission was observed. The ultimate origin of the long-lived excited population and the hot emission could not be identified so far. A tentative assignment of the origin points to a combination of polarons, ultra-low thermal conductivity and high-energy phonon modes associated with the organic cations. After formation of polarons at the M-point, the density of phonons that are in thermal contact with the hot carriers is limited. As a direct result, the cooling of charge carrier at the M-point is rather slow. [Fro17b] The slow cooling is enhanced due to the low thermal dissipation within the lattice. Along with the cooling of hot carriers, high-energy phonon modes are excited. The vibronic coupling between the hot carriers and the high-energy phonon modes results in a two different emission processes, namely hot and band edge emission. It has been suggested that hot carriers could enhance the efficiency of a solar cell. Although extraordinary high hot carrier extraction ratios up to 85% have previously been reported for colloidal perovskite nanocrystals after excitation at 500 nm, the overall efficiency increase for a realistic scenario would be small. [Li17a] The AM1.5 standard, which is used to test solar cells, results in a carrier density which is 2 - 3 orders of magnitude lower compared to the density used by Li *et al*, a condition that reduces the

total amount of long-living hot carriers significantly. In combination with the spectral distribution of the solar radiation, the additional extractable current is negligible. Beyond the physical limitation, a technical one is as important: the engineering challenge to build a solar cell with two charge extraction layers for each, electrons and holes. [Li17a, Ric17]

6. Photophysical changes of lead-halide perovskite films following methylamine treatment

The performance of a perovskite solar cell is highly dependent on the morphology of the perovskite layer. Common preparation techniques, such as spin-coating, show widespread effects on the final film morphology if it is not possible to control all the parameters that influence the film formation. Methylamine (MA) can be used to improve a perovskite film *post* deposition. In this chapter, the photophysical properties of lead-iodide perovskites prior and after the MA-treatment are discussed.

Section 6.1 discusses the photophysics of the MA-treatment related to a bare film and covers the fundamentals of this method. The work presented in section 6.1 is based on the collaboration with Amala Elizabeth from the Max Planck Institute for Polymer Research. Section 6.2 covers the photophysics of the MA-treatment when the perovskite film is used in a solar cell. Section 6.2 is based on the contribution to the paper "Structure-Property Relations of Methylamine Vapor Treated Hybrid Perovskite $CH_3NH_3PbI_3$ Films and Solar Cells". Adapted with permission from ACS Appl. Mater. Interfaces, (2017), 9 (9), pp 8092-8099. Copyright (2017) American Chemical Society. The work presented in section 6.2 was a cooperation between the Max Planck Institute for Polymer Research Mainz (Germany), the Institute for Materials Research at Hasselt University (Belgium) who collaboratively initiated the project, the Department of Physics of the University of Oxford (United Kingdom) and electron microscopy facility of the University of Antwerp (Belgium).

6.1. Photophysics of methylamine-treated perovskite films

Lead-halide perovskites have gained recognition in photovoltaic and optoelectronic research not only owing to easy and economic manufacturing by simple solution processing at low temperatures, but also due to their exceptional charge recombination and transport properties. Solution-processed solar cells manufactured by using lead-halide perovskite as

absorber material reach power conversion efficiencies of 22%. However, solution-processed films typically contain substantial surface defects, which require additional treatment to realize the full potential of the device. Methylamine (MA) treatment has been proposed as a post-processing treatment to enhance the power conversion efficiency of perovskite solar cells. However, the effect of MA treatment on the carrier recombination properties in lead-halide perovskites have not been widely studied. Here, we observe a substantial blue shift of the photoluminescence, lower photoluminescence intensity and faster trap-assisted recombination of lead-iodide perovskite films upon MA treatment. We propose that the MA treatment increases the trap density. The reduced emission intensity and the faster trap-assisted recombination can be directly related to the increased trap density. We assign the blue shift of the emission to the enhancement of the electric field in the surface layer of the perovskite as well as to structural disorder.

6.1.1. Introduction

Perovskite-structured lead halides ($APbX_3$, where A is CH_3NH_3, $CH(NH_2)_2$, Cs or Rb and X is I, Cl, Br) continue to remain a promising class of materials in the field of optoelectronic devices, including light-emitting diodes, nano-lasers and photovoltaics. [Zha16b, Li17b, CB17] The success of perovskite-based optoelectronic devices is based on their excellent charge generation, thermalization, recombination and transport properties, broad absorption range in the visible region and easy manufacturing. [Weh14a, Bre17b, Pri15, Yan17b, Her16b] Within 5 years after the initial report of a high-performance perovskite devices, solar cells with polycrystalline thin film $MAPbI_3$ as absorbers have achieved efficiencies greater than 22%. [Yan17a, Lee12] The ease of manufacturing of $MAPbI_3$ thin films by solution processing makes it the most economical choice for large-scale production of this exceptional photovoltaic material. However, solution-processing leads to incomplete surface coverage, micro- and macroscopic defects, like recombination centers and pinholes, that need to be controlled. In a device, macroscopic defects, e.g. pinholes, will reduce the shunt-resistance of the solar cell, compromising efficiency. Microscopic defects, which are caused either extrinsically due to imperfect manufacturing or intrinsically due to halide interstitials and halide vacancy migration, will limit the solar cell performance below the theoretical limits.[Qui15, Mos16, deQ16b, Str14] Hence, several post-annealing techniques aimed at improving the film quality after fabrication by simple solution processing have been developed. One such method is methylamine (MA) gas-treatment, first reported by Zhou *et al.* [Zho15] Essentially, methylamine gas is used to disrupt the perovskite structure in the thin film into a liquefied form. On removing the gas, recrystallization occurs, albeit with a more homogeneous morphology relative to the original form. Zhou *et al.* observed

a considerable increase in the power conversion efficiency (PCE) from 5% to 15% in a solar cell made usinggas-treated perovskite films as an absorber. They attributed the improved efficiency to improved morphology and healed defects. Zhang *et al.* observed an increase in the PCE of a solar cell device made from the gas-treated perovskite film from 6 to 15% in comparison to the raw device and assigned it to preferred crystal orientation in the (110)-direction [Zha16a]. An increase in the PCE of their solar cell by using methylamine vapor exposed MAPbI$_3$ films was also observed by Zhao *et al.* (3 to 12%) and Conings *et al.* (6 to 16%). [Zha16c, Con17] Both observed reduced emissive lifetimes and a blue shift of the emission of the perovskite thin film after the MA-treatment. Jiang *et al.* used methylamine gas exposure during the annealing and also found an increased performance, but increased lifetime and no blue shift the emission. [Jia16] Conings *et al.* also observed a significant reduction in the size of the crystal grains that form the polycrystalline film after MA-treatment, with single crystals having a size of 40 nm in the pristine and 30 nm in the MA-treated case. [Con17] Despite contrary observations concerning carrier lifetimes and spectral shifts, it was found that methylamine gas-treatment of MAPbI$_3$ thin films were beneficial for device applications. However, the exact photophysical effects of the method on the perovskite layer are still under debate.

In this work, we study in detail the effects of MA-treatment on MAPbI$_3$ thin films using scanning electron microscopy and static and time-resolved photoluminescence (TRPL) spectroscopy. During the MA-treatment, the sample undergoes a reversible chemical interaction with the methylamine gas, which typically leads to a drastic reduction of pinholes in the film. The MA-treatment is accompanied by a blue shift of the photoluminescence (PL) emission by 8 nm and a $\geq$5-fold reduction in the photoluminescence lifetime. We attribute the faster recombination as well as the decreased emission intensity to an increased density of trap states after the MA-treatment. Furthermore, we assign the blue shift of the emission to the increased electric field due to the increased trap density in the surface layer of the perovskite. Low-temperature emission measurements point to structural disorder as an additional effect of the MA-treatment.

6.1.2. Results and discussion

Polycrystalline thin films of MAPbI$_3$ are fabricated by spin coating an equimolar solution of PbI$_2$ and methylammonium iodide in anhydrous dimethylformamide (DMF) onto fused silica substrates (See experimental methods section for details) and annealing at room temperature and 100 °C. The resulting films consist of (polycrystalline) micrometer-sized needle-like grains with a large size distribution ranging from 500 nm to 2 μm with large pinholes. Scanning electron microscopy (SEM) images of MAPbI$_3$ thin films are shown in

figure 6.1. Methylamine gas treatment of these MAPbI$_3$ samples is carried out according to an earlier reported procedure by Zhou *et al.* [Zho15] In short, a reactor containing the sample is flushed with methylamine gas for a few seconds. The collapse of the perovskite crystal structure is observed by the formation of a clear liquid layer on the substrate. On subsequent removal of the methylamine gas from the chamber by flushing with N$_2$ gas, perovskite recrystallization occurs.
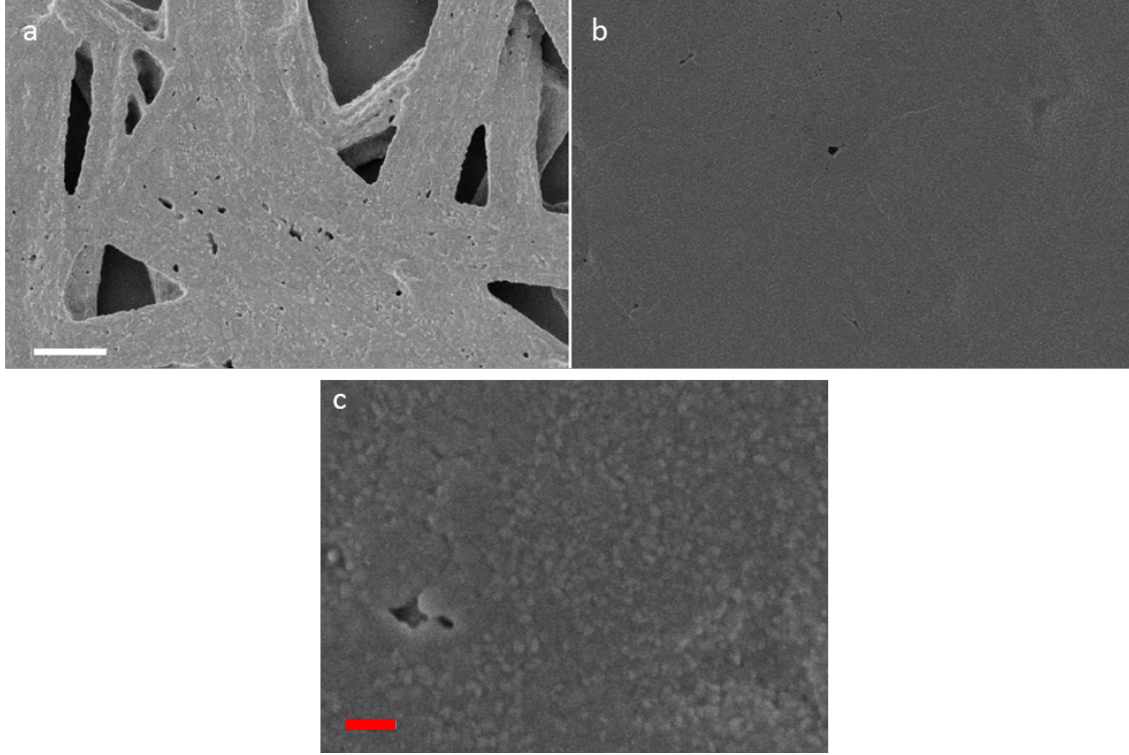

Figure 6.1.: Scanning electron microscopy images of pristine (a) and MA-treated (b) films. The scale bar is 1 μm. The pristine films consist of a discontinuous network of broad needle-like structures whereas the treated film shows a smooth surface with very few pinholes. A high-resolution image of the MA-treated film is shown in (c); the red scale bar is 200 nm. Small grains (<50 nm) can be observed. The pinhole in the left part of the image does not reach the substrate.

This procedure is intended to create uniform films with a smooth and homogeneous surface. As expected, the resulting films no longer contain the needle network structure, but instead form a homogeneous thin film with fewer pinholes as shown in figure 6.1, Panel B. Upon closer inspection, we find that both films (prior and after MA-treatment) consist of much smaller crystallites as shown in fig. 6.1C. The pristine film shows a large variety of grain sizes; whereas the MA-treated film shows more uniform size distribution and

overall smaller grain sizes (see figure 6.1C for a high-resolution image of the MA-treated film). To provide insight into the effect of MA-treatment on the optoelectronic properties of MAPbI$_3$, emission measurements from the pristine and MA-treated samples are compared (see fig. 6.2).
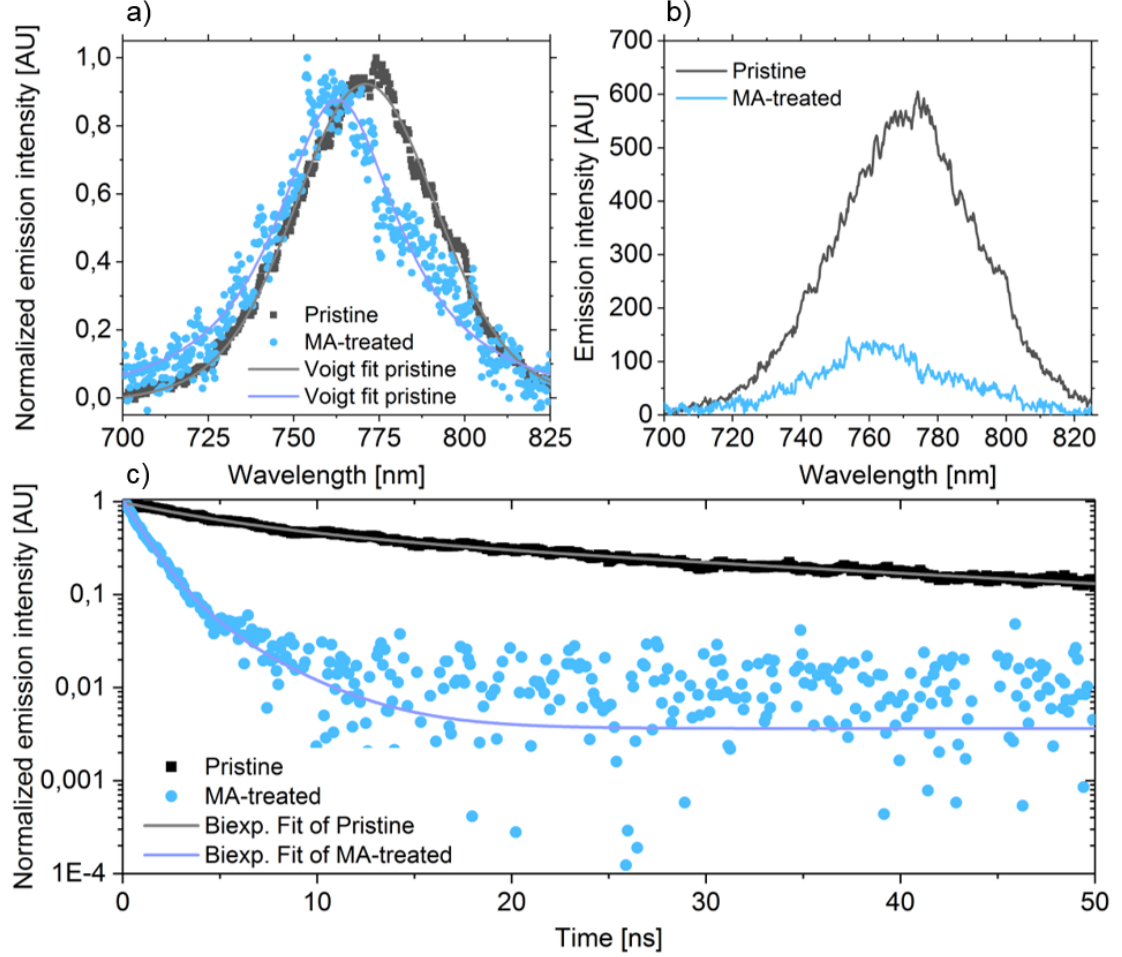

Figure 6.2.: Emission spectra and kinetics of the pristine and MA-treated film after excitation at 1μJ/cm^2 at 400 nm. Panel A visualizes the blue shift from 771 to 762 nm (8 nm) and the spectral narrowing (from 50 to 45 nm) upon the MA treatment. The spectra are fitted (solid lines) using a Voigt-function) Panel B shows the reduced emission intensity upon gas treatment (peaking at 600 compared to 130 counts). The peaks around 800 nm are spectral artifacts due to the overlap of the diffracted 400 nm excitation peaks. Panel C shows the recombination dynamics of the pristine and MA-treated samples including the much faster recombination after the MA treatment. The dynamics are fitted (solid lines) with a biexponential function.

For the pristine sample, the emission peak is at 771 ± 0.1 nm with an FWHM of 50.4 ± 0.2 nm (obtained from fitting with a Voigt-function. Upon methylamine treatment, we observe a blue shift of 8.1 nm to 762.8 ± 0.2 nm and a narrowing of the FWHM to 44.5 ± 0.7 nm. Time-resolved photoluminescence dynamics were measured along with the emission spectra (see fig. 6.2, Panel C) and reveal much faster recombination and therefore shorter emission lifetimes after the MA-treatment. Given the relatively high fluence ($1\mu J/cm^2$) and moderate signal-to-noise ratio, the trap-assisted lifetime cannot be obtained by fitting the dynamics with a single exponential function. Instead, we use a biexponential fitting function to obtain the trap-assisted lifetimes. The results of the fitting are given in table 6.1. Upon the MA-treatment, we observe a drastic reduction of the lifetimes τ_{fast} and τ_{slow}. The recombination dynamics of the pristine sample can be fitted with lifetimes of 5.7 and 35 ns. After the treatment, lifetimes of 1.1 and 3.3 ns can be extracted via fitting. The reduction of the lifetime in combination with the blue shift of the emission from lead-halide perovskite has also been previously reported by Sarmah *et al.*, who compared single- and two-photon absorption measurements. [Sar17] They found that the emission after single-photon excitation (more surface sensitive due to the smaller penetration depth) was blue shifted in comparison to two-photon-excitation, which is more bulk sensitive due to the large penetration depth. The blue shift was accompanied by a strong reduction of the lifetime. They related the blue shift of the emission and the reduction of the lifetime to the electric field in the surface layer of the perovskite, which is present owing to the selective migration of iodine interstitials to the surface. [Sar17] Since the MA-treatment results in the formation of smaller crystal

Table 6.1.: Fitting results of the emission dynamics

	A_{fast}	τ_{fast} [ns]	A_{slow}	τ_{slow} [ns]
Pristine sample	0,49±0,01	5,74±0,12	0,47±0,01	35,04±0,92
MA-treated sample	0,86±0,04	1,12±0,05	0,17±0,05	3,30±0,5

grains in comparison to the pristine films (see figure 6.1), the surface-to-volume ratio increases. Therefore, we associate the blue shift of the emission to the surface, especially to the increased density of surface traps. Several studies using ultrafast transient photoluminescence and transient absorption spectroscopy have identified the surface and grain boundaries of crystals (for both single crystals and polycrystalline films) as major sites for traps. [Yan17b, deQ16b, Wu15a, Gra15a, Gra17] Therefore, it can be assumed that the higher surface area is related to a higher trap density. A majority of these traps originate from mobile iodine interstitials and iodine vacancies (V_I^+/I_i^-)) as well as MA vacancies. [Mos16, Yin14b, Sar17, OY92] Under thermal equilibrium, (defect-induced) interstitial iodine ions move to the surface to reduce the elastic energy. Due to the separation of the charged defects, an electric field is generated in the surface layer.

[deQ16b, Sar17] Sarmah *et al.* were able to correlate the density of iodide interstitials $n_{\text{Iod-Int.}}$ to the strength of the electric field $\mathbf{E}$, which is proportional to the wavelength shift of the emission: $\Delta\lambda \sim \mathbf{E} \sim n_{\text{Iod-Int.}}$. [Sar17] We assume that the increased density of trap states after the MA-treatment results in an enhanced electric field in the surface layer of the perovskite and therefore in a blue shift of the emission in comparison to the pristine sample. Our proposition is supported by measurement by Li *et al.* who observed a size-dependent blue shift for single-crystalline perovskite microplates. [Li16]

Crothers *et al.* and Pazos-Outon *et al.* report on carrier recycling in 100+ nm thick films as a cause for shifts of the emission from perovskites. [Cro17, PO16] Crothers *et al.* observed a blue shift for thin (50 nm) samples compared to thicker (400 nm) samples as a result of the emission and re-absorption in thin films thicker than the absorption length of the pump pulse. [Cro17] We note that carrier recycling will also occur in both pristine and MA-treated sample as the film thickness exceeds 400 nm in both cases, but the blue shift of the MA-treated sample can still be observed, indicating that the surface trap-induced blue shift is a different mechanism from carrier recycling. In addition to increasing the density of traps, MA treatment can alter the nature of the trap states. We can also exclude strain as an exclusive origin, as it would result in a spectral widening of the emission peak, rather than the spectral narrowing in combination with a blue shift. [Li15] We note that the magnitude of the blue shift of the emission and the faster recombination upon gas-treatment is sample-dependent, but the trend can always be observed unless the sample suffers from excessive non-radiative recombination due to poor sample quality.

In addition to the effect of the surface traps, we suspect a second contribution from (structural) disorder originating from the soft, organic-inorganic nature of the perovskite and the small crystal size to the observed blue shift after MA treatment. [Gra17, Gra15b, Fro16b, Osh16] We performed time-resolved photoluminescence measurements at 77K, well below the nominal phase transition temperature (shown in fig. 6.3) using two different pump fluences (5 and 10 μJ/cm^2).

When excited with a pump fluence of 5 μJ/cm^2, the pristine sample shows only a single emission peak at 760 nm, including a weak red-shifted shoulder as a result of emissive traps. [Weh14c] For the MA-treated sample excited with a pump fluence at 5 μJ/cm^2, we observe two peaks at 787 and 745 nm. The lifetime of the peak at 745 nm is much shorter than the peak at 787 nm peak (see fig. 6.3C). These peaks represent the orthorhombic and tetragonal phase and are commonly associated with the phase-coexistence region around 150K. These peaks are observed even at 77K. [Osh16, Weh14c, Kon15, Dob17, Qin17] Recombination dynamics (see fig. 6.3C) of the peaks at 745 and 787 nm show a donor-
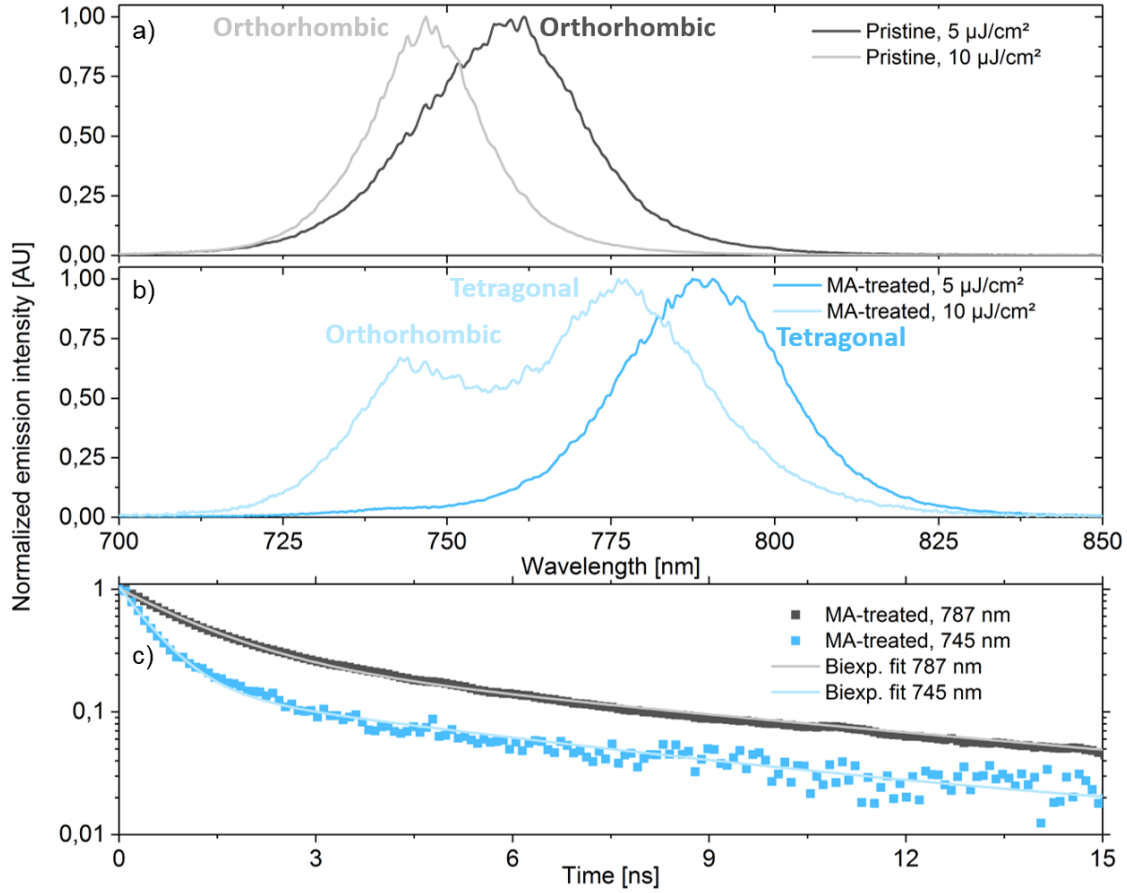
Figure 6.3.: Normalized emission measurements at 77K for pristine and MA-treated samples after excitation at 400 nm. A shows a single emission peak of the pristine sample, centered at 760 nm for a fluence of 5 μJ/cm^2 and at 746 nm for a fluence of 10 μJ/cm^2. B shows the emission spectra of the treated sample featuring two emission peaks, a fluence-independent peak at 745 nm and a second peak at 787 nm (5 μJ/cm^2) and 776 nm (10 μJ/cm^2). C shows the normalized recombination dynamics of the MA-treated sample at 77 K. The emission peak assigned to the orthorhombic structure (745 nm) and the tetragonal structure (787 nm) are shown. The (biexponential) fitted lifetimes (solid lines) for the peak at 787 nm are $\tau_{\text{fast}} = 1{,}22 \pm 0{,}01$ ns, $\tau_{\text{slow}} = 8{,}32 \pm 0{,}01$ ns and for the peak at 745 nm are $\tau_{\text{fast}} = 0{,}52 \pm 0{,}01$ ns, $\tau_{\text{slow}} = 5{,}80 \pm 0{,}01$ ns.

acceptor behavior, which is expected for phase-coexistence. [Kon15] In a donor-acceptor system, charge carriers are transported from the large energy-gap material (donor) to the low energy-gap material (acceptor). Therefore, the recombination dynamics should speed up in the donor material, as an additional decay channel for the carriers (transport to the acceptor, making radiative recombination impossible) exists. The observation of the shorter lifetime of the peak at 745 nm in comparison to the peak at 782 nm supports

the notion of donor-acceptor behavior. Comparison of the two emission spectra shows a size-dependent phase-transition temperature in our samples: the small crystals obtained via the MA-treatment show emission from the orthorhombic and tetragonal phases even at 77K, whereas the pristine sample shows only emission from the orthorhombic phase. Our conclusion is supported by observations from Li *et al.*, who reported size-dependent phase-transition for single-crystalline perovskite microplates. [Li16, Osh16] Although we cannot observe direct emission from the orthorhombic phase in our perovskite samples due to homogeneous and inhomogeneous broadening of the room-temperature emission peak, we propose the occurrence of structural disorder based on the phase coexistence well below and above the nominal phase transition temperature. This structural disorder also contributes to the blue shift of the emission in addition to the surface-trap induced blue shift. This is supported by observations by Conings *et al.*, who reports a higher Urbach-energy for MA-treated samples compared to pristine ones. [Con17] Chen *et al.* have reported the Burstein-Moss shift (a band-filling effect, where the band gap widens due to band filling effects) as a possible explanation for the size-dependent blue shift. [Weh14c] The Burstein-Moss shift has also been observed in lead-halide perovskites, but only as a dynamic phenomenon. [Han14, Yan15, Pri15] In fig. 6.3, we also show a comparison of the emission spectra for pump fluences of 5 and 10 μJ/cm^2 averaged over the first 5 nanoseconds. The Burstein-Moss shift can be observed for the orthorhombic peak of the pristine sample and the tetragonal peak of the MA-treated sample, but not for the orthorhombic peak of the MA-treated sample in addition to the surface trap induced blue shift. We attribute the absence of the shift to the fast relaxation of carriers from the orthorhombic to the tetragonal phase. Fig. 6.2B also shows the lower emission intensity of MA-treated samples compared to pristine samples. The coexistence of the phase at room temperature gives rise to additional sub-bandgap levels, which increases the non-radiative decay, thereby decreasing radiative emission. [Qin17]

6.1.3. Conclusion

In conclusion, we report the effects of methylamine treatment on solution-processed lead-halide perovskite films and observe a strong blue shift of the photoluminescence and substantial recombination lifetime reduction of lead-halide perovskite film upon methylamine-treatment. Photoluminescence measurements at 77 K show phase coexistence well below the nominal orthorhombic-tetragonal phase transition temperature of 150 K for the MA-treated films, but not for pristine ones. Based on these observations, we suggest a combination of the enhancement of the electric field in the surface layer of the perovskite due to the additional traps and structural disorder even at room temperature as the origin of the blue shift upon methylamine treatment.

6.1.4. Methods

Equimolar ratio (1.1 M) of the precursors lead iodide PbI_2 (99.999% Sigma Aldrich) and methylammonium iodide (MAI) (Solaronix) were dissolved in anhydrous N,N-Dimethylformamide (DMF) (Sigma Aldrich) and stirred overnight at 60 °C to obtain 42 wt% solution of $MAPbI_3$. 30 μl of the perovskite solution was spin coated onto a piranha cleaned 1 cm x 1 cm fused silica substrates at 2000 rpm for 60 s and annealed at 100 °C for 25 min. Prior to annealing, the spin coated samples were left in the inert atmosphere at RT for 22 minutes to allow slow evaporation of the excess solvent present. (Note there was no preheating of the substrates prior to the solution deposition). Although the films turn black within seconds of annealing signaling the formation of $MAPbI_3$, they were kept longer on the hotplate to ensure complete evaporation of the solvent. For gas-treatment, the samples were transferred to a sealed glass chamber in the inert atmosphere of the glovebox. Initially, the chamber is flushed with N2 for 15 ± 2 s to ensure the atmosphere is inert. This is followed by flushing the chamber with methylamine (CH_3NH_2) gas (Methylamin 2.0, Linde) for 10 ± 2 s. Consequently, the gas is removed from the chamber by flushing with N_2 again for 15 ± 2 s. The glass sample holder ensured that the perovskite thin films never came in contact with atmospheric conditions before and during the gas-treatment.

Scanning electron microscopy (SEM) images were collected using LEO Gemini 1530 microscope at a working bias of 3 kV.

Time-resolved photoluminescence was measured under dynamic high vacuum conditions with a C5680 Hamamatsu streak camera system following excitation at 400 nm from a frequency-doubled mode-locked titanium:sapphire amplifier (Coherent LIBRA HE, 3.5 mJ, 100 fs) with a repetition rate of 1 kHz (100 ns time window).

6.2. Photophysics of methylamine-treated perovskite layers used in solar cells

The preparation of a pinhole-free lead-halide perovskite layer is a crucial step in order to obtain a high-performance perovskite solar cell. The state of the art deposition techniques require precise control over numerous variables, e.g. the solvent atmosphere in a glovebox, making commercialization difficult. An alternative approach is to improve the properties such as the trap density or the surface coverage *post* deposition. A number of post-processing strategies are used to improve the morphology and the charge-transport of the perovskite. Commonly used methods include solvent annealing or solid-gas interaction of $MAPbI_3$ with methylamine (MA) gas. Using a MA-treatment to improve the performance of the solar cell was initially reported by Zhou *et al.* The treatment led to a drastic improvement of the surface coverage and was later expanded to improve the performance of $FAPbI_3$ devices. [Zho15, Zho16]

In order to not only study the improvement of the device but also attempt to unravel the underlying mechanisms of the MA-treatment, the following systematic approach was chosen. The method combines the comparison of structural information from X-ray diffraction (XRD) and electron microscopy with transport as well as time-resolved photoluminescence measurements. Two sets of perovskite films were prepared using a single-step deposition method on top of a mesoporous layer. During thermal annealing, large ($\simeq$ 500 nm) crystallites form, however at this point the surface coverage is still incomplete. In order to investigate the charge extraction and charge recombination, two different mesoporous layer were used: semiconducting mesoporous TiO_2 or insulating mesoporous Al_2O_3. While a set of samples was used as-prepared (pristine), another set of samples was exposed to methylamine and subsequently dried with nitrogen[1]. Upon the MA-treatment, the $MAPbI_3$ crystallites shrunk in combination with a complete coverage of the substrate surface. Solar cells prepared from the pristine and MA-treated perovskite films yielded efficiencies of 6.2% and 16.9%, respectively. XRD measurements showed much higher diffraction peaks of the treated films, indicating improved crystallinity compared to pristine films. To elucidate the origin of the improved crystallinity despite the reduced crystal size, transmission electron microscopy measurements were performed. It was found that the single-crystalline grain size was $\sim$ 40 nm for pristine and MA-treated films. The analysis of the width of the diffraction peaks using the *Scherrer* equation reveals grain sizes $\sim$ 30 nm for the MA-treated grains and $\sim$ 40 nm for pristine grains. As a complementary method, time-resolved photoluminescence was measured (see figure 6.4). In order to distinguish between the contribution of the recombination originating from perovskite capping layer and the perovskite confined in the mesoporous network, each side was illu-

---

[1]for complete experimental details, see [Con17]

minated separately as used by D'Innocenzo *et al.*[2] [DI14b] The resulting kinetics of the photoluminescence decay were fitted with a biexponential function. A biexponential was used to fit the dynamics instead of an exponential function in order to account for the relatively high fluence (1 μJ/cm^2) required for an acceptable signal-to-noise ratio used in the experiment. The decay kinetics for the Al$_2$O$_3$ demonstrate a change in the slope after 5 to 10 ns (see figure 6.4, panel A). The change of slope can be interpreted as the progression from bimolecular to trap-assisted recombination. Due to the use of biexponential fitting, the interpretation of the initial slope, which is associated with the first decay time (τ_1, for Al$_2$O$_3$ in the first ∼10 ns), is not straightforward. However, the decay of the photoluminescence after the change of slope can be associated with trap-assisted recombination (characterized by τ_2) and can be therefore be interpreted as a measure of the trap density. [Qui15, Ric16] As shown in figure 6.4, panel A, after the MA-treatment, the trap-assisted lifetime is reduced from 19.8 ± 0.3 ns to 16.1 ± 0.5 ns. The single-crystal size was determined to be quite similar before and after the treatment. The reduction of the trap-assisted lifetime is assumed to be correlated with increased non-radiative recombination, originating from a higher trap density. Our results and interpretation are consistent with measurements of Zhao *et al.* [Zha16c] The increased non-radiative recombination correlates well to the reduced emission intensity, which appears in the spectra in figure 6.4, panel B. For the case of the perovskite confined in the Al$_2$O$_3$, the trap-assisted lifetime increases upon MA-treatment from 12.6 ± 0.3 ns to 16 ± 0.5 ns. Interestingly, after the MA-treatment the trap-assisted lifetimes of the perovskite capping layer and the perovskite confined in the mesoporous layer are almost identical. This observation suggests that the MA-treatment is responsible for the increased trap density rather than the local structural environment. The proposed explanation is supported by the nearly identical positions of the emission peaks. Nevertheless, the trap-assisted lifetime increases due to the MA-treatment, which is interpreted to be related to the increased pore filling of the Al$_2$O$_3$ and the resulting increase crystallite size. Due to the charge extraction into the TiO$_2$ as an additional decay channel competing with the photoluminescence, the interpretation of the photoluminescence decay lifetimes is different compared to the measurements of perovskite in Al$_2$O$_3$. In figure 6.4, panel E, one can observe slightly faster radiative recombination for the case of the MA-treatment. The faster reduction of the photoluminescence intensity suggests improved charge extraction at the perovskite/TiO$_2$-interface, valid under the assumption that the results of the perovskite in the mesoporous Al$_2$O$_3$ are transferable to the TiO$_2$.

The discrepancy between the improved device performance and the increased trap density is still under intense discussion. Several possibilities are being discussed to explain the behavior:

---

[2]Excitation with 400 nm corresponds to a penetration depth of around 100 nm. The thickness of the mesoporous and capping layer is > 150 nm.

As a consequence of the growth-mechanism of the perovskite grains after the initial crystallization (Oswald-ripening, see section 3.1), using MA-treatment without subsequent annealing might retain imperfect grains. The preservation of imperfect grains is evident from the higher trap density and lower PLQY. [Str15a, Str15b]

The crystallization mechanism of the *liquefied* perovskite-methylamine-phase is most likely different from the Volmer-Weber growth discussed in section 3.1. It was observed that the properties of perovskite film after the treatment depend on the characteristics of the substrate as the liquefied phase was partially found to form a meniscus on the substrate.

For any metal-organic chemical vapor deposition process, obtaining the right parameters, such as process temperature and timing, is crucial for the outcome of the process. The uncontrolled recrystallization from the colorless intermediate state, which improves the surface coverage and presumably the pore-filling and the physical contact to the interface can be obtained quite easily. Based on extensive experiments, which include various flow- and purging rates of the treatment chamber, recrystallization under nitrogen-, vacuum or mixed methylamine-nitrogen atmospheric conditions within a temperature range between 5 and 60 °C and different post-treatment annealing procedures, the trap-assisted lifetime was limited to the lifetime of the pristine sample. A reduced external PLQY due to the increase non-radiative recombination was observed for all the treated samples.

A successful treatment was published by Jiang *et al.*, who applied a combination of the methylamine treatment while annealing the sample. They were able to not only increase the device performance by 50%, but also to increase the trap-assisted lifetime by a factor of ~ 3, indicating a net lower trap-density.[Jia16]

To summarize, methylamine treatment of perovskite films was successfully used to improve the device efficiency by a factor of nearly three. Based on complementary characterization tools, it was concluded that the improvement of the device efficiency is related to the improved surface coverage and better filling of the mesoporous metal oxide layer. Partially as a consequence of the improved pore filling, the electron extraction across the perovskite/TiO$_2$-interface was found to improve as well. The improvement is even more astonishing with respect due to the increased non-radiative recombination and increased trap density in the perovskite capping layer. The improvement of the charge extraction despite the increased trap density can be seen as confirmation of the proposed defect tolerance of lead-halide perovskites. At the same time, it is required to understand and control the recrystallization of the perovskite under methylamine atmosphere especially on the local scale in order to utilize the full potential of the treatment.
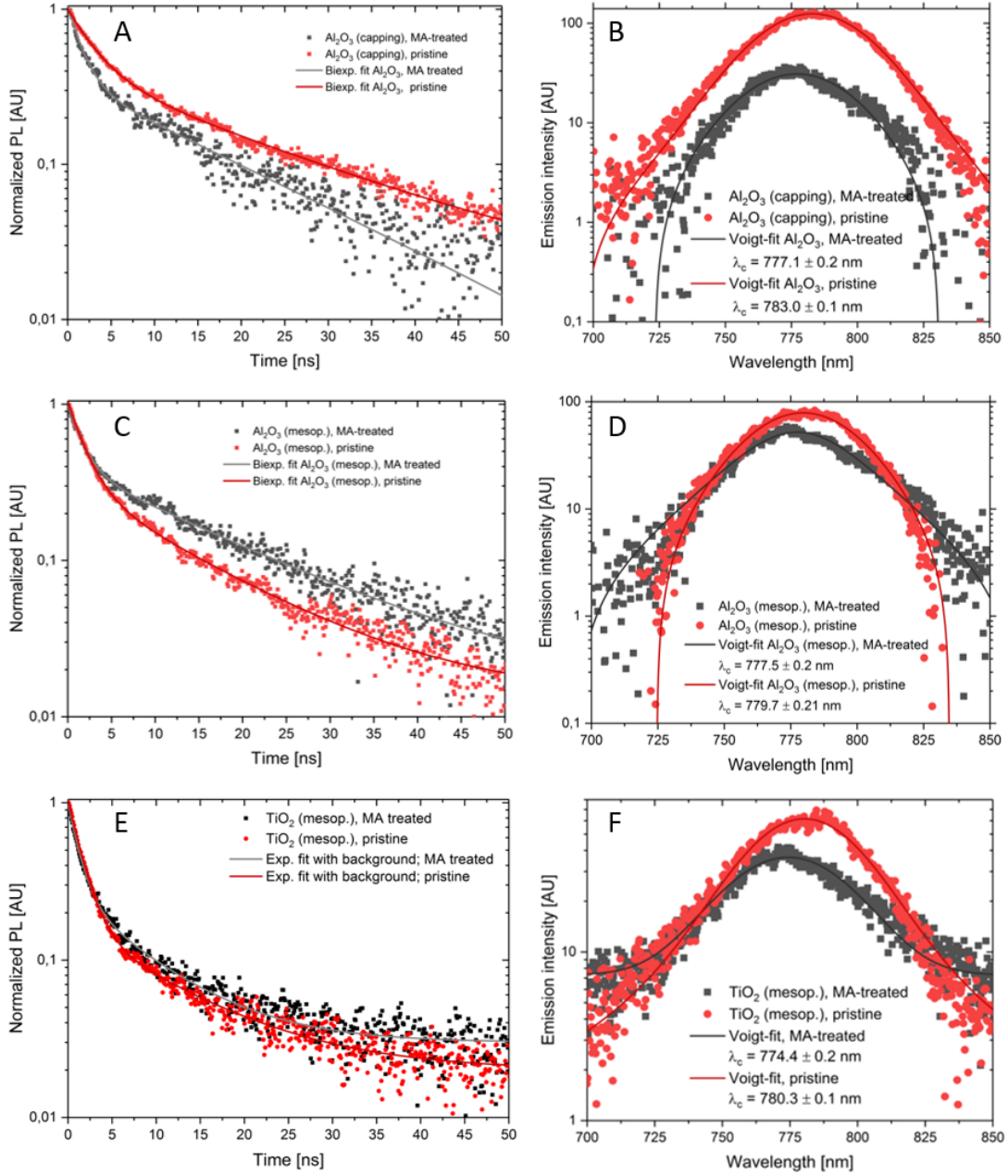
Figure 6.4.: Time-resolved photoluminescence measurements of pristine and MA-treated samples. Panel A shows the faster recombination of the perovskite capping layer after the MA-treatment; B the corresponding substantial blue-shift due to the MA-treatment; C shows the slower recombination of the perovskite in the mesoporous Al_2O_3 after the MA-treatment; D the corresponding small blue-shift and spectral broadening after the treatment. E shows the slightly faster recombination of the perovskite in the mesoporous TiO_2 after the MA-treatment, F the corresponding blue-shift of 6 nm after the MA-treatment. Adapted from [Con17] with permission of the American Chemical Society (2017).

7. Conclusion and outlook

Solar cells provide an ideal opportunity to generate electrical power without the emission of greenhouse gases. Due to the drastic reduction of the cost of photovoltaics in the last years, Si-based solar cells have become the cheapest option for new power plants. The reduction of cost per kWh is mostly caused by the mass production effects rather than an improvement of the efficiencies of solar cells. To reduce the cost per kWh even further, new concepts to enhance the solar cell efficiency, such as multi-junction solar cells, are required. In addition to silicon as an established absorber material, a number of compounds, which absorb in the visible spectral range such as InGaAs, InGaN or halide perovskites are proposed for the role as a complementary material. Halide perovskites can be solution processed and have tunable absorption, which makes them an ideal partner to Silicon in a low-cost multi-junction solar cell. Single-junction solar cells made from halide perovskites reach astonishing power conversion efficiencies exceeding 22.5%, however some of the most basic properties, such as the origin of the low recombination rates, have not been clearly understood yet.

In this thesis, the fundamental photophysical and engineering-related properties of solution-processed lead-iodide have been investigated using ultrafast spectroscopy. Three separate characteristics were studied. The formation of polarons and initial charge carrier cooling were investigated using time-resolved THz spectroscopy. The slow cooling of hot carriers and the corresponding hot emission were examined using transient absorption and time-resolved photoluminescence spectroscopy. The effects of a post-preparation methylamine treatment to the luminescent properties were investigated using photoluminescence spectroscopy.

Hybrid organic-inorganic lead-halide perovskites show exceptionally low bimolecular recombination rates, making them much more comparable to inorganic semiconductors like GaAs, instead of organic semiconductors. Despite similar low effective masses ($m_e^* \simeq 0.12 m_e$ and $m_h^* \simeq 0.15 m_e$), the charge carrier mobility of lead-halide based perovskites was reported to be rather moderate. The moderate carrier mobility in lead-halide perovskites is surprisingly low compared to GaAs, where the mobility is more than two orders of magnitude higher. The low bimolecular recombination in

combination with the moderate mobility suggests the formation of polarons. Due to the local interaction of charge carriers with the lattice, the effective mass of the polarons is increased in comparison to the bare electron in the conduction band, which could explain the moderate mobility of charge carriers in lead-iodide perovskites. As a side effect of the polaron formation, opposite charge carriers become localized in spatially different regions, lowering the recombination rate due to the reduced spatial overlap of electron/hole wave functions. [Iva17, Miy17b, Amb18]

The dynamics of polaron formation in MAPbI$_3$ and FAPbI$_3$ is discussed in chapter 4. Time-resolved THz spectroscopy was used to investigate the polaron formation, specifically to probe the rise of the photoconductivity on a sub-ps timescales. The transient photoconductivity is a good indicator for the formation of polarons in the Γ-valley due to its dependence on the scattering time τ_s and the effective mass m_e^* via the mobility μ (section 2.6.1). As the generation of free charge carriers was determined to occur on a sub-0.05 ps timescale, the photoconductivity should rise on a comparable timescale. In stark contrast, we observed that the photoconductivity rises within 1.5 ps for resonant excitation. When the pump photons carried excess energy in comparison to the band gap, the rise of the photoconductivity was even slower (within 2.5 ps at an excess energy of 1.5 eV). A lower temperature resulted in slower rise time of the photoconductivity. The dynamics were analyzed using a three-level system, which distinguishes between populations of hot carriers, cold carriers and polarons. It was assumed that hot carriers cool before forming polarons. The rise of the photoconductivity was found to contain contributions from both the formation of the polarons and the initial carrier cooling. The polaron was found to form with a characteristic timescale of 0.4 $\pm$ 0.02 ps, independent of the cation and the lattice temperature in a range of 160 K to room temperature. The cooling of carriers in the Γ-Valley is cation- and temperature-dependent, resulting in cooling times of 0.28 $\pm$ 0.02 ps for FAPbI$_3$ and 0.32 $\pm$ 0.02 ps for MAPbI$_3$ after excitation at 3.1 eV at room temperature. The data and the chosen model could not determine whether polarons are formed before cooling to the lattice temperature or if free charge carriers cool before the polarons are formed. The temperature-dependence of the transient photoconductivity can be attributed to scattering of optical phonons with the polarons. The phonon-polaron scattering ultimately limits the carrier mobility and cooling. In addition to the investigated timescale of a few picoseconds, polarons play an essential role for the low bimolecular recombination of charge carriers due to localization of oppositely charged polarons in spatially separated regions. [Amb18]

The cooling of charge carriers and hot emission in MAPbI$_3$(Cl) is discussed in chapter 5. The temporal and spectral evolution of the ground state bleach, i.e. the

lowest-energetic excited state, was investigated using transient absorption spectroscopy whereas the emissive properties were investigated using photoluminescence spectroscopy. When excited at 2.05 eV with a low fluence of 2.5 μJ/cm^2, the population of the band edges monitored using the ground state bleach was measured to be constant for nearly 100 ps before decreasing due to the recombination of charge carriers. When excited at or above an energy of 2.6 eV, the population of the band edges increased during the first 100 ps, before decreasing. Using a three-level system, we found that the increased population of the band edges is related to the decay of a hot population with a lifetime of 40 $\pm$ 2 ps. This slow cooling mechanism is different from the hot-phonon bottleneck, which can be observed for excitation at 3.1 eV with a fluence of 39 μJ/cm^2 (discussed in section 2.5). The slow cooling after excitation 2.6 or 3.1 eV is related to a long-living hot carrier population at the M-point. The origin of the slow cooling of the population is assigned to a combination of four effects. The formation of the polaron results in reduced scattering with optical phonons, which was reported to be the main cooling mechanism of carriers (compare to section 2.5). The large momentum mismatch between the M- and the Γ-point, the limited density of states 0.3 eV above the conduction band minimum and the ultra-low thermal conductivity also contribute to the slow cooling. [Pis14, Nie16c] As discussed in appendix A, the morphology affects the dynamics of the ground state population due to locally different trap nature and density. Along with the cooling of hot carriers, the emission from states with an excess energy of up to 0.15 eV above the band edges was observed. The hot emission decayed within $\sim$ 100 ps with a relaxation rate of 0.16 $\pm$ 0.01 meV/ps and was assigned to originate from the coupling of charge carriers and the organic cations. [Zha17b] As for the population of the ground state discussed in appendix A, the local properties affect also the radiative recombination.

The recombination in pristine and post-processed MAPbI$_3$ films is discussed in chapter 6. A methylamine treatment is a promising method to improve a perovskite film *post* deposition, resulting in an enhancement of the efficiency of perovskite solar cells. Upon methylamine treatment, the surface coverage of MAPbI$_3$ films improved, resulting in an overall boost of the power conversion efficiency by a factor of three. Along with the improvement of the efficiency, we measured a reduction of the radiative emission intensity by a factor of four, a five-fold reduction of the trap-assisted lifetime and a blue shift of the emission by 9 nm. The counterintuitive improvement of the solar cell efficiency and the decreased radiative lifetime and emission intensity are related to separate effects of the treatment. While the single crystalline grain size was not affected by the methylamine treatment, the nature and the density of surface traps are affected. Due to the increased density of traps, the trap-assisted radiative recombination occurs faster. The emission intensity is reduced as a result of increased non-radiative recombination.[Yin14b] The

blue shift of the emission is also attributed to the higher density of trap states. Under thermal equilibrium, iodine interstitials, which are common traps, were reported to diffuse to the surface in order to reduce the elastic energy. [Sar17] Due to the separation of iodine interstitials and iodine vacancies in the bulk perovskite, an electric field at the surface is generated. The strength of the electric field and the correlated blue shift of the emission are related to the density of charged trap states. Furthermore, it is proposed that, with regard to the effect of the treatment on the device efficiency, the increased trap density is more than balanced by an enhancement of the surface coverage and improved charge carrier extraction. The fact that the power conversion efficiency increases despite an increased trap density highlights the potential of methylamine treatment to improve the overall performance of halide perovskite optoelectronic devices.

This thesis aims to contribute to the understanding of the ultrafast photophysical properties of lead-iodide perovskites. The observation and quantification of polaron formation in $MAPbI_3$ and $FAPbI_3$ allows for a better comprehension of the success of perovskite solar cells. The polarons result in low recombination and band-like transport of charge carriers. The slow cooling of charge carriers and the subsequent increase of the ground state population shows the unique fundamental properties of lead-iodide perovskite. The importance and nature of the trap density were furthermore illustrated with the preparation-dependent ground state population dynamics and radiative recombination, contributing therefore to the knowledge of the extrinsic effects to the photophysics of perovskite films.

While the future of solar power is bright, the future of solar cells prepared from lead-halide solar cell has not yet been decided. The intrinsic instabilities of the perovskite due to the low threshold of ion and vacancy migration has not yet been resolved, however initial steps, such as iodide and contact management, show promising results. [Yan17a, Aro17, Hou17] As a positive side-effect of ion migration, self-healing of light-induced trap states occurs, which could be crucial for the stability of a device under terrestrial conditions, i.e. a day and night cycles. [Nie16a] While small area perovskite solar cells reach efficiencies exceeding 22.5 %, the scaling of these devices towards commercially usable sizes using spin-coating technology remains challenging. Only a few techniques, for instance costly co-evaporation and complicated multi-step chemical vapor deposition, have already been successfully used for the preparation of larger cells. [Jia18, Hsi16] A much better perspective share colloidal lead-halide perovskite quantum dots and low-dimensional perovskite structures for lighting and lasing applications. The fully inorganic perovskite quantum dots such as $CsPbBr_3$ or $CsPbCl_3$ are successfully used as light emitting diodes, whereas single crystalline nanoplates

and nanowires show low lasing thresholds. [Xin14, Zhu15a, Shi17a, Son15, Kov17] Beyond the application, the investigation of the fundamental properties of halide perovskite remains an ongoing challenge. The investigation of carrier recombination, thermalization and the non-equilibrium transport with high spatial and temporal resolution are currently widely investigated. [Qui15, Nah17, Nah18, Guo17] Following the work presented in this thesis about the formation of polarons, an important challenge remains: to reveal the origin of the low recombination rates taking into account the combined or complementary effects of the Rashba-effect, polarons and the electronic band structure of halide perovskites. [Hut17, Nie16b, Che17] Tackling the fundamental and engineering challenges will hopefully allow us to shift to a cleaner energy economy.

The shift to a cleaner energy economy won't happen overnight, and it will require some tough choices along the way.
But the debate is settled. Climate change is a fact. And when our children's children look us in the eye and ask if we did all we could to leave them a safer, more stable world, with new sources of energy, I want us to be able to say yes, we did.
Barack Obama, 2014 State of the Union Address

A. Morphology-dependent ground state population in MAPbI$_3$(Cl)

In addition to the standard deposition of MAPbI$_3$(Cl), a modified annealing scheme was used. The spin-coated film was annealed under ambient conditions for 30 min, followed by solvent annealing. The samples were annealed for 1h at 100 °C under a petri dish in the presence of 10 μL of DMF followed by 1h at 100 °C in a nitrogen atmosphere. [Xia14b, Her16a] The standard deposition method resulted in crystals with sizes around 1 μm, whereas the solvent annealing resulted in much large crystals, as shown in figure A.1.
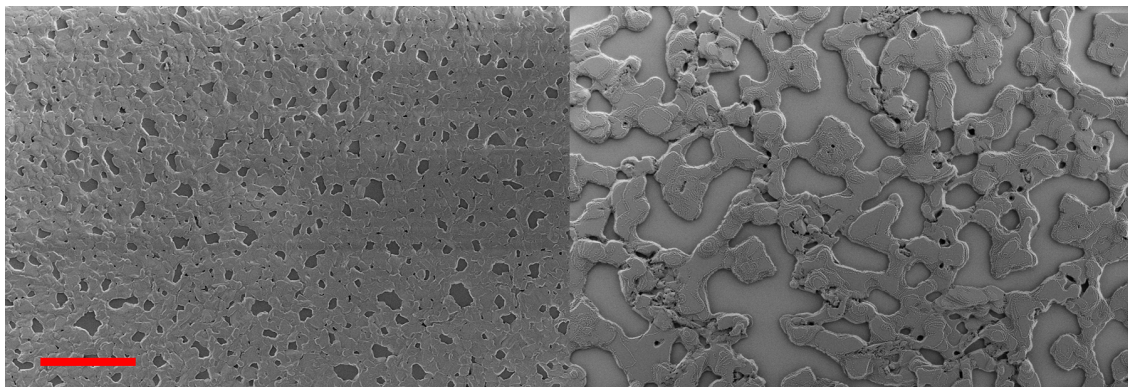
Figure A.1.: SEM images of MAPbI$_3$(Cl) films prepared from thermal (left) and solvent annealing (right). The scale bar is 10 μm, and applies to both images.

The samples were investigated using transient absorption spectroscopy in order to elucidate the dynamics of the ground state bleach and the carrier cooling. The graphical comparison of the measurements is shown in figure A.2. Two features can be identified for both annealing procedures; the ground state bleach centered around 740 nm and the derivative-like signal associated to the band gap renormalization at 760 nm at around 1 ps. The signature of the hot carrier cooling is highly dependent on the annealing procedure. For the thermal annealing, the spectral signature of the hot-phonon bottleneck can clearly be observed. [Yan15, Pri15] The slow cooling of charge carriers above the band

edges is visible in the low-wavelength tail accompanied by the redshift of the ground state bleach, both happening on the order of 100 ps.
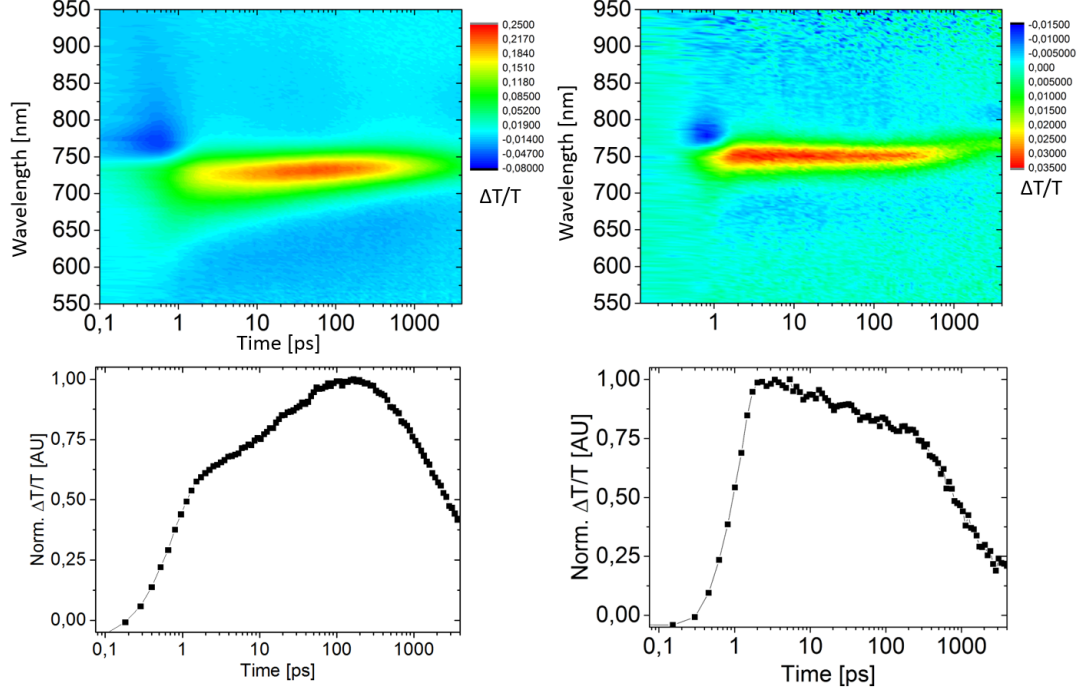

Figure A.2.: Transient absorption measurements of MAPbI$_3$(Cl) films prepared from thermal (left) and solvent annealing (right). The samples were excited with a fluence of 39 μJ/cm^2 at 3.1 eV. The upper panels show the two-dimensional maps of the measurements, the lower ones the kinetics of the ground state bleach of the corresponding measurements.

The low-wavelength tail accompanied by the redshift of the ground state bleach are absent in the measurement of the solvent annealed sample. The absence of the hot phonon bottleneck can be explained by the trap density, which depends on the annealing scheme. In particular, the formation of MAPbI$_3$(Cl) crystals relies on the evaporation of excess MACl during the annealing process. As the solvent annealing is performed under a petri-dish, the evaporation of excess MA might be reduced. The deviation from the nominal stoichiometric composition might lead to the formation of trap states within in valence or conduction bands in the proximity of the band minima.[1] For a high trap density within the valence and conduction bands, additional scattering of hot carriers with impurities is expected to result in faster cooling in comparison to scattering only with optical phonons.

---

[1]The most relevant trap states outside of the band gap are MA-interstitials and lead-vacancies, which are positioned within $\pm$ 0.25 eV of the band edges. [Yin14b]

List of Figures

Bibliography

[Ama14]   A. Amat, E. Mosconi, E. Ronca, C. Quarti, P. Umari, M. K. Nazeeruddin, M. Grätzel und F. De Angelis, *Cation-induced band-gap tuning in organohalide perovskites: Interplay of spin-orbit coupling and octahedra tilting*, Nano Letters **14**(6), S. 3608 (2014), URL `http://dx.doi.org/10.1021/nl5012992`.

[Amb18]   F. Ambrosio, J. Wiktor, F. De Angelis und A. Pasquarello, *Origin of low electron hole recombination rate in metal halide perovskites*, Energy and Environmental Science (2018), URL `http://dx.doi.org/10.1039/C7EE01981E`.

[Ana16]   B. Anand, S. Sampat, E. O. Danilov, W. Peng, S. M. Rupich, Y. J. Chabal, Y. N. Gartstein und A. V. Malko, *Broadband transient absorption study of photoexcitations in lead halide perovskites: Towards a multiband picture*, Physical Review B **93**(16), S. 161205 (2016), URL `http://link.aps.org/doi/10.1103/PhysRevB.93.161205`.

[Anu17]   I. Anusca, S. Balciunas, P. Gemeiner, S. Svirskas, M. Sanlialp, G. Lackner, C. Fettkenhauer, J. Belovickis, V. Samulionis, M. Ivanov, B. Dkhil, J. Banys, V. V. Shvartsman und D. C. Lupascu, *Dielectric response: Answer to many questions in the methylammonium lead halide solar cell absorbers*, Advanced Energy Materials **7**(19), S. 1700600 (2017), URL `http://dx.doi.org/10.1002/aenm.201700600`.

[App17a] K. Appavoo, W. Y. Nie, J. C. Blancon, J. Even, A. D. Mohite und M. Y. Sfeir, *Ultrafast optical snapshots of hybrid perovskites reveal the origin of multiband electronic transitions*, Physical Review B **96**(19) (2017), URL `<GotoISI>://WOS:000416312900005`.

[App17b] K. Appavoo, W. Y. Nie, J. C. Blancon, J. Even, A. D. Mohite und M. Y. Sfeir, *Ultrafast optical snapshots of hybrid perovskites reveal the origin of multiband electronic transitions*, Physical Review B **96**(19), S. 195308 (2017), URL `<GotoISI>://WOS:000416312900005`.

[Aro17]   N. Arora, M. I. Dar, A. Hinderhofer, N. Pellet, F. Schreiber, S. M. Zakeeruddin und M. GrÃ¤tzel, *Perovskite solar cells with cuscn hole extraction layers yield stabilized efficiencies greater than 20 percent*, Science (2017).

[Aza16]   P. Azarhoosh, S. McKechnie, J. M. Frost, A. Walsh und M. v. Schilfgaarde, *Research update: Relativistic origin of slow electron-hole recombination in hybrid halide perovskite solar cells*, APL Materials **4**(9), S. 091501 (2016), URL `http://aip.scitation.org/doi/abs/10.1063/1.4955028`.

[Bak15]   A. A. Bakulin, O. Selig, H. J. Bakker, Y. L. A. Rezus, C. MÃ¼ller, T. Glaser, R. Lovrincic, Z. Sun, Z. Chen, A. Walsh, J. M. Frost und T. L. C. Jansen, *Real-time observation of organic cation reorientation in methylammonium lead iodide perovskites*, The Journal of Physical Chemistry Letters **6**(18), S. 3663 (2015), URL `http://dx.doi.org/10.1021/acs.jpclett.5b01555`.

[Bal97]   N. Balkan, *Hot electrons in semiconductors. Physics and Devices.*, Oxford University Press (1997).

[Ber14]   V. W. Bergmann, S. A. L. Weber, F. Javier Ramos, M. K. Nazeeruddin, M. GrÃ¤tzel, D. Li, A. L. Domanski, I. Lieberwirth, S. Ahmad und R. Berger, *Real-space observation of unbalanced charge distribution inside a perovskite-sensitized solar cell*, Nat Commun **5** (2014), URL `http://dx.doi.org/10.1038/ncomms6001`.

[Bet02]   M. Betz, G. Goger, A. Leitenstorfer, P. Gartner, L. Banyai und H. Haug, *Virtual carrier-lo phonon interaction in the intermediate coupling region: the quantum dynamical formation of polarons*, Physica B: Condensed Matter **314**(1), S. 76 (2002), URL `http://www.sciencedirect.com/science/article/pii/S0921452601014569`.

[Bet04]   M. Betz, R. Huber, F. Tauser, A. Brodschelm, A. Leitenstorfer, P. Gartner, L. Banyai und H. Haug, *Ultrafast Formation of Quasiparticles in Semiconductors: How Bare Charges Get Dressed*, S. 231–249, Springer Berlin Heidelberg, Berlin, Heidelberg (2004), URL `https://doi.org/10.1007/978-3-662-08990-3_13`.

[Bok16]   M. Bokdam, T. Sander, A. Stroppa, S. Picozzi, D. D. Sarma, C. Franchini und G. Kresse, *Role of polar phonons in the photo excited state of metal halide perovskites*, Scientific Reports **6**, S. 28618 (2016), URL `http://dx.doi.org/10.1038/srep28618`.

[Bon17] M. Bonn, K. Miyata, E. Hendry und X. Zhu, *On the role of dielectric drag in polaron mobility in lead halide perovskites*, ACS Energy Letters (2017), URL `http://dx.doi.org/10.1021/acsenergylett.7b00717`.

[Boy08] R. Boyd, *Nonlinear Optics*, Academic Press, Elsevier, 3rd editon Auflage (2008).

[Bre10] S. A. Bretschneider, *Development of a High-Repetition Rate Modelocked Yb-Fiber Laser for THz Spectroscopy*, Bachelor thesis (2010).

[Bre13] S. A. Bretschneider, *Perovskite Absorber Hybrid Solar Cells*, Master thesis (2013).

[Bre14] S. A. Bretschneider, J. Weickert, J. A. Dorman und L. Schmidt-Mende, *Research update: Physical and electrical characteristics of lead halide perovskites for solar cell applications*, APL Materials **2**(4), S. 040701 (2014), URL `http://scitation.aip.org/content/aip/journal/aplmater/2/4/10.1063/1.4871795`.

[Bre17a] R. Brenes, D. Guo, A. Osherov, N. K. Noel, C. Eames, E. M. Hutter, S. K. Pathak, F. Niroui, R. H. Friend, M. S. Islam, H. J. Snaith, V. Bulovic, T. J. Savenije und S. D. Stranks, *Metal halide perovskite polycrystalline films exhibiting properties of single crystals*, Joule **1**(1), S. 155 (2017), URL `http://www.sciencedirect.com/science/article/pii/S2542435117300314`.

[Bre17b] S. A. Bretschneider, F. Laquai und M. Bonn, *Trap-free hot carrier relaxation in lead-halide perovskite films*, Journal of Physical Chemistry C **121**(21), S. 11201 (2017), URL `<GotoISI>://WOS:000402775200022`.

[CB17]   J.-P. Correa-Baena, M. Saliba, T. Buonassisi, M. Grätzel, A. Abate, W. Tress und A. Hagfeldt, *Promises and challenges of perovskite solar cells*, Science **358**(6364), S. 739 (2017).

[Cer03] G. Cerullo und S. De Silvestri, *Ultrafast optical parametric amplifiers*, Review of Scientific Instruments **74**(1), S. 1 (2003), URL `https://doi.org/10.1063/1.1523642`.

[Cha16] A. Y. Chang, Y. J. Cho, K. C. Chen, C. W. Chen, A. Kinaci, B. T. Diroll, M. J. Wagner, M. K. Y. Chan, H. W. Lin und R. D. Schaller, *Slow organic-to-inorganic sub-lattice thermalization in methylammonium lead halide perovskites observed by ultrafast photoluminescence*, Advanced Energy Materials **6**(15), S. 1600422 (2016), URL `<GotoISI>://WOS:000381695700003`.

[Che14] K. Chen, A. J. Barker, F. L. C. Morgan, J. E. Halpert und J. M. Hodgkiss, *Effect of carrier thermalization dynamics on light emission and amplification in organometal halide perovskites*, The Journal of Physical Chemistry Letters **6**(1), S. 153 (2014), URL http://dx.doi.org/10.1021/jz502528c.

[Che16] Y. Chen, H. T. Yi, X. Wu, R. Haroldson, Y. N. Gartstein, Y. I. Rodionov, K. S. Tikhonov, A. Zakhidov, X. Y. Zhu und V. Podzorov, *Extended carrier lifetimes and diffusion in hybrid perovskites revealed by hall effect and photoconductivity measurements*, Nature Communications **7**, S. 12253 (2016), URL http://dx.doi.org/10.1038/ncomms12253.

[Che17] Z. Chen, M.-i. Lee, Z. Zhang, H. Diab, D. Garrot, F. Lédée, P. Fertey, E. Papalazarou, M. Marsi, C. Ponseca, E. Deleporte, A. Tejeda und L. Perfetti, *Time-resolved photoemission spectroscopy of electronic cooling and localization in* **ch$_3$nh$_3$pbi$_3$** *crystals*, Physical Review Materials **1**(4), S. 045402 (2017), URL https://link.aps.org/doi/10.1103/PhysRevMaterials.1.045402.

[Cho17] K. T. Cho, S. Paek, G. Grancini, C. Roldan Carmona, P. Gao, Y. H. Lee und M. K. Nazeeruddin, *Highly efficient perovskite solar cells with a compositional engineered perovskite/hole transporting material interface*, Energy and Environmental Science **10**(2), S. 621 (2017), URL http://dx.doi.org/10.1039/C6EE03182J.

[Con17] B. Conings, S. A. Bretschneider, A. Babayigit, N. Gauquelin, I. Cardinaletti, J. Manca, J. Verbeeck, H. J. Snaith und H.-G. Boyen, *Structure property relations of methylamine vapor treated hybrid perovskite ch3nh3pbi3 films and solar cells*, ACS Applied Materials and Interfaces **9**(9), S. 8092 (2017), URL http://dx.doi.org/10.1021/acsami.6b15175.

[Cro17] T. W. Crothers, R. L. Milot, J. B. Patel, E. S. Parrott, J. Schlipf, P. Müller-Buschbaum, M. B. Johnston und L. M. Herz, *Photon reabsorption masks intrinsic bimolecular charge-carrier recombination in ch3nh3pbi3 perovskite*, Nano Letters (2017), URL http://dx.doi.org/10.1021/acs.nanolett.7b02834.

[CT09] C. Cohen-Tannoudji, *Quantum Mechanics*, De Gruyter, Berlin, 4th Auflage (2009).

[Dem08] W. Demtroeder, *Laser spectroscopy*, Springer-Verlag, Springer-Verlag Berlin Heidelberg, 4th edition Auflage (2008).

[Dem16] D. O. Demchenko, N. Izyumskaya, M. Feneberg, V. Avrutin, U. Ozgur, R. Gold-hahn und H. Morkoç, *Optical properties of the organic inorganic hybrid perovskite ch3nh3pbi3: Theory and experiment*, Physical Review B **94**(7), S. 075206 (2016), URL `https://link.aps.org/doi/10.1103/PhysRevB.94.075206`.

[deQ16a] D. W. deQuilettes, S. Koch, S. Burke, R. K. Paranji, A. J. Shropshire, M. E. Ziffer und D. S. Ginger, *Photoluminescence lifetimes exceeding 8 Î¼s and quantum yields exceeding 30passivation*, ACS Energy Letters **1**(2), S. 438 (2016), URL `http://dx.doi.org/10.1021/acsenergylett.6b00236`.

[deQ16b] D. W. deQuilettes, W. Zhang, V. M. Burlakov, D. J. Graham, T. Leijtens, A. Osherov, V. Bulovic, H. J. Snaith, D. S. Ginger und S. D. Stranks, *Photo induced halide redistribution in organic inorganic perovskite films* **7**, S. 11683 (2016), URL `http://dx.doi.org/10.1038/ncomms11683`.

[DI14a] V. D Innocenzo, G. Grancini, M. J. P. Alcocer, A. R. S. Kandada, S. D. Stranks, M. M. Lee, G. Lanzani, H. J. Snaith und A. Petrozza, *Excitons versus free charges in organo-lead tri-halide perovskites*, Nat Commun **5** (2014), URL `http://dx.doi.org/10.1038/ncomms4586`.

[DI14b] V. D Innocenzo, A. R. Srimath Kandada, M. De Bastiani, M. Gandini und A. Petrozza, *Tuning the light emission properties by band gap engineering in hybrid lead halide perovskite*, Journal of the American Chemical Society **136**(51), S. 17730 (2014), URL `http://dx.doi.org/10.1021/ja511198f`.

[Die06] J.-C. Diels und W. Rudolph, *Ultrashort laser pulse phaenomena*, Elsevier, Academic Press, 2nd Auflage (2006).

[Dob17] A. Dobrovolsky, A. Merdasa, E. L. Unger, A. Yartsev und I. G. Scheblykin, *Defect-induced local variation of crystal phase transition temperature in metal-halide perovskites*, Nature Communications **8**(1), S. 34 (2017), URL `http://dx.doi.org/10.1038/s41467-017-00058-w`.

[End16a] J. Endres, D. A. Egger, M. Kulbak, R. A. Kerner, L. Zhao, S. H. Silver, G. Hodes, B. P. Rand, D. Cahen, L. Kronik und A. Kahn, *Valence and conduction band densities of states of metal halide perovskites: A combined experimental-theoretical study*, The Journal of Physical Chemistry Letters **7**(14), S. 2722 (2016), URL `http://dx.doi.org/10.1021/acs.jpclett.6b00946`.

[End16b] J. Endres, D. A. Egger, M. Kulbak, R. A. Kerner, L. Zhao, S. H. Silver, G. Hodes, B. P. Rand, D. Cahen, L. Kronik und A. Kahn, *Valence and conduction band densities of states of metal halide perovskites: A combined experimental-theoretical study*, The Journal of Physical Chemistry Letters **7**(14), S. 2722 (2016), URL http://dx.doi.org/10.1021/acs.jpclett.6b00946.

[Eti16] T. Etienne, E. Mosconi und F. De Angelis, *Dynamical origin of the rashba effect in organohalide lead perovskites: A key to suppressed carrier recombination in perovskite solar cells?*, The Journal of Physical Chemistry Letters **7**(9), S. 1638 (2016), URL http://dx.doi.org/10.1021/acs.jpclett.6b00564.

[Etz14] F. Etzold, *A Photophysical Study of Excited State Dynamics in Donor-Acceptor Copolymer Photovoltaic Blends*, Phd thesis (2014).

[Eve14] J. Even, L. Pedesseau und C. Katan, *Analysis of multivalley and multibandgap absorption and enhancement of free carriers related to exciton screening in hybrid perovskites*, The Journal of Physical Chemistry C **118**(22), S. 11566 (2014), URL http://dx.doi.org/10.1021/jp503337a.

[Fab17] D. H. Fabini, T. A. Siaw, C. C. Stoumpos, G. Laurita, D. Olds, K. Page, J. G. Hu, M. G. Kanatzidis, S. Han und R. Seshadri, *Universal dynamics of molecular reorientation in hybrid lead iodide perovskites*, Journal of the American Chemical Society (2017), URL http://dx.doi.org/10.1021/jacs.7b09536.

[Fen14] J. Feng, *Mechanical properties of hybrid organic-inorganic ch3nh3bx3 (b = sn, pb; x = br, i) perovskites for solar cell absorbers*, APL Materials **2**(8), S. 081801 (2014), URL http://aip.scitation.org/doi/abs/10.1063/1.4885256.

[Fey55] R. P. Feynman, *Slow electrons in a polar crystal*, Physical Review **97**(3), S. 660 (1955), URL https://link.aps.org/doi/10.1103/PhysRev.97.660.

[Fey62] R. P. Feynman, R. W. Hellwarth, C. K. Iddings und P. M. Platzman, *Mobility of slow electrons in a polar crystal*, Physical Review **127**(4), S. 1004 (1962), URL https://link.aps.org/doi/10.1103/PhysRev.127.1004.

[Fle15] O. Flender, J. R. Klein, T. Lenzer und K. Oum, *Ultrafast photoinduced dynamics of the organolead trihalide perovskite ch3nh3pbi3 on mesoporous tio2 scaffolds in the 320-920 nm range*, Physical Chemistry Chemical Physics (2015), URL http://dx.doi.org/10.1039/C5CP01973G.

[Fri05] P. A. R. Friedman, *Molecular Quantum Mechanics*, Oxford University Press, Oxford University Press, 4th Auflage (2005).

[Fro16a] J. M. Frost, P. Azarhoosh, S. McKechnie, M. van Schilfgaarde und A. Walsh, *A photon ratchet route to high-efficiency hybrid halide perovskite intermediate band solar cells*, ArXiv e-prints **1611** (2016), URL https://arxiv.org/abs/1611.09786.

[Fro16b] J. M. Frost und A. Walsh, *What is moving in hybrid halide perovskite solar cells?*, Accounts of Chemical Research **49**(3), S. 528 (2016), URL http://dx.doi.org/10.1021/acs.accounts.5b00431.

[Fro17a] J. M. Frost, *Calculating polaron mobility in halide perovskites*, Physical Review B **96**(19), S. 195202 (2017), URL https://link.aps.org/doi/10.1103/PhysRevB.96.195202.

[Fro17b] J. M. Frost, L. D. Whalley und A. Walsh, *Slow cooling of hot polarons in halide perovskite solar cells*, ACS Energy Letters S. 2647–2652 (2017), URL http://dx.doi.org/10.1021/acsenergylett.7b00862.

[Fu17] J. Fu, Q. Xu, G. Han, B. Wu, C. H. A. Huan, M. L. Leek und T. C. Sum, *Hot carrier cooling mechanisms in halide perovskites*, Nature Communications **8**(1), S. 1300 (2017), URL https://doi.org/10.1038/s41467-017-01360-3.

[Gao16] W. Gao, X. Gao, T. A. Abtew, Y.-Y. Sun, S. Zhang und P. Zhang, *Quasiparticle band gap of organic-inorganic hybrid perovskites: Crystal structure, spin-orbit coupling, and self-energy effects*, Physical Review B **93**(8), S. 085202 (2016), URL http://link.aps.org/doi/10.1103/PhysRevB.93.085202.

[Gho17] T. Ghosh, S. Aharon, L. Etgar und S. Ruhman, *Free carrier emergence and onset of electron phonon coupling in methylammonium lead halide perovskite films*, Journal of the American Chemical Society (2017), URL http://dx.doi.org/10.1021/jacs.7b09508.

[Giu17] F. Giustino, *Electron-phonon interactions from first principles*, Reviews of Modern Physics **89**(1), S. 015003 (2017), URL https://link.aps.org/doi/10.1103/RevModPhys.89.015003.

[Gra15a] G. Grancini, V. D'Innocenzo, E. R. Dohner, N. Martino, A. R. Srimath Kandada, E. Mosconi, F. De Angelis, H. I. Karunadasa, E. T. Hoke und a. petrozza, *Ch3nh3pbi3 perovskite single crystals: Surface photophysics and its interaction with the environment*, Chemical Science (2015), URL http://dx.doi.org/10.1039/C5SC02542G.

[Gra15b] G. Grancini, A. R. Srimath Kandada, J. M. Frost, A. J. Barker, M. De Bastiani, M. Gandini, S. Marras, G. Lanzani, A. Walsh und A. Petrozza, *Role of microstructure in the electron-hole interaction of hybrid lead-halide perovskites*, Nat Photonics **9**(10), S. 695 (2015), URL http://www.ncbi.nlm.nih.gov/pubmed/26442125.

[Gra17] G. Grancini, D. Viola, M. Gandini, D. Altamura, E. A. A. Pogna, V. D Innocenzo, I. Bargigia, C. Giannini, G. Cerullo und A. Petrozza, *Lattice distortions drive electron-hole correlation within micrometer-size lead-iodide perovskite crystals*, ACS Energy Letters **2**(1), S. 265 (2017), URL http://dx.doi.org/10.1021/acsenergylett.6b00607.

[Gre03] M. Green, *Third Generation Photovoltaics*, Springer-Verlag Berlin Heidelberg (2003).

[Guo15] Y. Guo, K. Shoyama, W. Sato, Y. Matsuo, K. Inoue, K. Harano, C. Liu, H. Tanaka und E. Nakamura, *Chemical pathways connecting lead(ii) iodide and perovskite via polymeric plumbate(ii) fiber*, Journal of the American Chemical Society **137**(50), S. 15907 (2015), URL http://dx.doi.org/10.1021/jacs.5b10599.

[Guo17] Z. Guo, Y. Wan, M. Yang, J. Snaider, K. Zhu und L. Huang, *Long-range hot-carrier transport in hybrid perovskites visualized by ultrafast microscopy*, Science **356**(6333), S. 59 (2017).

[Han14] F. C. Hanusch, E. Wiesenmayer, E. Mankel, A. Binek, P. Angloher, C. Fraunhofer, N. Giesbrecht, J. M. Feckl, W. Jaegermann, D. Johrendt, T. Bein und P. Docampo, *Efficient planar heterojunction perovskite solar cells based on formamidinium lead bromide*, The Journal of Physical Chemistry Letters S. 2791–2795 (2014), URL http://dx.doi.org/10.1021/jz501237m.

[Hen04] E. Hendry, F. Wang, J. Shan, T. F. Heinz und M. Bonn, *Electron transport in tio2 probed by thz time-domain spectroscopy*, Physical Review B **69**(8), S. 081101 (2004), URL https://link.aps.org/doi/10.1103/PhysRevB.69.081101.

[Her16a] I. M. Hermes, S. A. Bretschneider, V. W. Bergmann, D. Li, A. Klasen, J. Mars, W. Tremel, F. Laquai, H.-J. Butt, M. Mezger, R. Berger, B. J. Rodriguez und S. A. L. Weber, *Ferroelastic fingerprints in methylammonium lead iodide perovskite*, The Journal of Physical Chemistry C **120**(10), S. 5724 (2016), URL http://dx.doi.org/10.1021/acs.jpcc.5b11469.

[Her16b] L. M. Herz, *Charge carrier dynamics in organic inorganic metal halide perovskites*, Annual Review of Physical Chemistry **67**(1), S. 65 (2016), URL `http://www.annualreviews.org/doi/abs/10.1146/annurev-physchem-040215-112222`.

[Hou17] Y. Hou, X. Du, S. Scheiner, D. P. McMeekin, Z. Wang, N. Li, M. S. Killian, H. Chen, M. Richter, I. Levchuk, N. Schrenker, E. Spiecker, T. Stubhan, N. A. Luechinger, A. Hirsch, P. Schmuki, H.-P. Steinrück, R. H. Fink, M. Halik, H. J. Snaith und C. J. Brabec, *A generic interface to reduce the efficiency-stability-cost gap of perovskite solar cells*, Science (2017).

[Hsi16] S.-Y. Hsiao, H.-L. Lin, W.-H. Lee, W.-L. Tsai, K.-M. Chiang, W.-Y. Liao, C.-Z. Ren-Wu, C.-Y. Chen und H.-W. Lin, *Efficient all-vacuum deposited perovskite solar cells by controlling reagent partial pressure in high vacuum*, Advanced Materials **28**(32), S. 7013 (2016), URL `http://dx.doi.org/10.1002/adma.201601505`.

[Hut17] E. M. Hutter, M. C. Gelvez-Rueda, A. Osherov, V. Bulovic, F. C. Grozema, S. D. Stranks und T. J. Savenije, *Direct-indirect character of the bandgap in methylammonium lead iodide perovskite*, Nat Mater **16**(1), S. 115 (2017), URL `http://dx.doi.org/10.1038/nmat4765`.

[Iba09] H. Ibach; und H. Luth, *Solid-state physics*, Springer-Verlag, Berlin Heidelberg (2009).

[Iva17] T. Ivanovska, C. Dionigi, E. Mosconi, F. De Angelis, F. Liscio, V. Morandi und G. Ruani, *Long-lived photoinduced polarons in organohalide perovskites*, The Journal of Physical Chemistry Letters S. 3081–3086 (2017), URL `http://dx.doi.org/10.1021/acs.jpclett.7b01156`.

[Jeo14] N. J. Jeon, J. H. Noh, Y. C. Kim, W. S. Yang, S. Ryu und S. I. Seok, *Solvent engineering for high performance inorganic organic hybrid perovskite solar cells*, Nat Mater **13**(9), S. 897 (2014), URL `http://dx.doi.org/10.1038/nmat4014`.

[Jep11] P. U. Jepsen, D. G. Cooke und M. Koch, *Terahertz spectroscopy and imaging: Modern techniques and applications*, Laser and Photonics Reviews **5**(1), S. 124 (2011), URL `http://dx.doi.org/10.1002/lpor.201000011`.

[Jia16] Y. Jiang, E. J. Juarez-Perez, Q. Ge, S. Wang, M. R. Leyden, L. K. Ono, S. R. Raga, J. Hu und Y. Qi, *Post-annealing of mapbi3 perovskite films with methylamine for efficient perovskite solar cells*, Materials Horizons **3**(6), S. 548 (2016), URL `http://dx.doi.org/10.1039/C6MH00160B`.

[Jia18] Y. Jiang, M. R. Leyden, L. Qiu, S. Wang, L. K. Ono, Z. Wu, E. J. Juarez-Perez und Y. Qi, *Combination of hybrid cvd and cation exchange for upscaling cs-substituted mixed cation perovskite solar cells with high efficiency and stability*, Advanced Functional Materials **28**(1), S. 1703835 (2018), URL `http://dx.doi.org/10.1002/adfm.201703835`.

[Kaw15] H. Kawai, G. Giorgi, A. Marini und K. Yamashita, *The mechanism of slow hot hole cooling in lead-iodide perovskite: First principles calculation on carrier lifetime from electron phonon interaction*, Nano Letters **15**(5), S. 3103 (2015), URL `http://dx.doi.org/10.1021/acs.nanolett.5b00109`.

[Kel17] U. Keller, *Ultrafast Laser Physics*, ETH Zurich, ETH Zurich (2017).

[Koh65] W. Kohn und L. J. Sham, *Self-consistent equations including exchange and correlation effects*, Physical Review **140**(4A), S. A1133 (1965), URL `https://link.aps.org/doi/10.1103/PhysRev.140.A1133`.

[Koj09] A. Kojima, K. Teshima, Y. Shirai und T. Miyasaka, *Organometal halide perovskites as visible-light sensitizers for photovoltaic cells*, Journal of the American Chemical Society **131**(17), S. 6050 (2009), URL `http://dx.doi.org/10.1021/ja809598r`.

[Kon15] W. Kong, Z. Ye, Z. Qi, B. Zhang, M. Wang, A. Rahimi-Iman und H. Wu, *Characterization of an abnormal photoluminescence behavior upon crystal-phase transition of perovskite ch3nh3pbi3*, Physical Chemistry Chemical Physics **17**(25), S. 16405 (2015), URL `http://dx.doi.org/10.1039/C5CP02605A`.

[Kov17] M. V. Kovalenko, L. Protesescu und M. I. Bodnarchuk, *Properties and potential optoelectronic applications of lead halide perovskite nanocrystals*, Science **358**(6364), S. 745 (2017), URL `http://science.sciencemag.org/content/sci/358/6364/745.full.pdf`.

[Kue10] W. Kuehn, P. Gaal, K. Reimann, M. Woerner, T. Elsaesser und R. Hey, *Coherent ballistic motion of electrons in a periodic potential*, Physical Review Letters **104**(14), S. 146602 (2010), URL `https://link.aps.org/doi/10.1103/PhysRevLett.104.146602`.

[Kut14] Y. Kutes, L. Ye, Y. Zhou, S. Pang, B. D. Huey und N. P. Padture, *Direct observation of ferroelectric domains in solution-processed ch3nh3pbi3 perovskite thin films*, The Journal of Physical Chemistry Letters **5**(19), S. 3335 (2014), URL `http://dx.doi.org/10.1021/jz501697b`.

[La15] O. V. C. La, T. Salim, J. Kadro, M. T. Khuc, R. Haselsberger, L. Cheng, H. Xia, G. G. Gurzadyan, H. Su, Y. M. Lam, R. A. Marcus, M. E. Michel-Beyerle und E. E. Chia, *Elucidating the role of disorder and free-carrier recombination kinetics in ch3nh3pbi3 perovskite films*, Nat Comm. **6**, S. 7903 (2015), URL `https://www.ncbi.nlm.nih.gov/pubmed/26224196`.

[Lan48] L. Landau und S. Pekar, *Effective mass of a polaron*, Zh. Eksp. Teor. Fiz. (JETP Letters) **18**(5), S. 419 (1948).

[Lee12] M. M. Lee, J. Teuscher, T. Miyasaka, T. N. Murakami und H. J. Snaith, *Efficient hybrid solar cells based on meso-superstructured organometal halide perovskites*, Science **338**(6107), S. 643 (2012), URL `http://www.sciencemag.org/content/338/6107/643.abstract`.

[Leg16] A. M. A. Leguy, P. Azarhoosh, M. I. Alonso, M. Campoy-Quiles, O. J. Weber, J. Yao, D. Bryant, M. T. Weller, J. Nelson, A. Walsh, M. van Schilfgaarde und P. R. F. Barnes, *Experimental and theoretical optical properties of methylammonium lead halide perovskites*, Nanoscale **8**(12), S. 6317 (2016), URL `http://dx.doi.org/10.1039/C5NR05435D`.

[Lei11] A. Leitenstorfer, *Semiconductor physics* (2011).

[Li15] D. Li, Y. Liu, M. de la Mata, C. Magen, J. Arbiol, Y. Feng und Q. Xiong, *Strain-induced spatially indirect exciton recombination in zinc-blende/wurtzite cds heterostructures*, Nano Research **8**(9), S. 3035 (2015), URL `https://doi.org/10.1007/s12274-015-0809-8`.

[Li16] D. Li, G. Wang, H.-C. Cheng, C.-Y. Chen, H. Wu, Y. Liu, Y. Huang und X. Duan, *Size-dependent phase transition in methylammonium lead iodide perovskite microplate crystals*, Nature Communications **7**, S. 11330 (2016), URL `http://dx.doi.org/10.1038/ncomms11330`.

[Li17a] M. Li, S. Bhaumik, T. W. Goh, M. S. Kumar, N. Yantara, M. Grätzel, S. Mhaisalkar, N. Mathews und T. C. Sum, *Slow cooling and highly efficient extraction of hot carriers in colloidal perovskite nanocrystals*, Nature Communications **8**, S. 14350 (2017), URL `http://dx.doi.org/10.1038/ncomms14350`.

[Li17b] W. Li, Z. Wang, F. Deschler, S. Gao, R. H. Friend und A. K. Cheetham, *Chemically diverse and multifunctional hybrid organic inorganic perovskites*, Nature Reviews Materials S. 16099 (2017), URL `http://dx.doi.org/10.1038/natrevmats.2016.99`.

[Man14]   J. S. Manser und P. V. Kamat, *Band filling with free charge carriers in organometal halide perovskites*, Nat Photon **8**(9), S. 737 (2014), URL `http://dx.doi.org/10.1038/nphoton.2014.171`.

[Man17]   P.-A. Mante, C. C. Stoumpos, M. G. Kanatzidis und A. Yartsev, *Electron-acoustic phonon coupling in single crystal ch3nh3pbi3 perovskites revealed by coherent acoustic phonons*, Nature Communications **8**, S. 14398 (2017), URL `http://dx.doi.org/10.1038/ncomms14398`.

[Mil15]   R. L. Milot, G. E. Eperon, H. J. Snaith, M. B. Johnston und L. M. Herz, *Temperature-dependent charge-carrier dynamics in ch3nh3pbi3 perovskite thin films*, Advanced Functional Materials **25**(39), S. 6218 (2015), URL `<GotoISI>://WOS:000363207000008`.

[Miy15]   A. Miyata, A. Mitioglu, P. Plochocka, O. Portugall, J. T.-W. Wang, S. D. Stranks, H. J. Snaith und R. J. Nicholas, *Direct measurement of the exciton binding energy and effective masses for charge carriers in organic-inorganic tri-halide perovskites*, Nat Phys **11**(7), S. 582 (2015), URL `http://dx.doi.org/10.1038/nphys3357`.

[Miy17a]   K. Miyata, T. L. Atallah und X.-Y. Zhu, *Lead halide perovskites: Crystal-liquid duality, phonon glass electron crystals, and large polaron formation*, Science Advances **3**(10) (2017).

[Miy17b]   K. Miyata, D. Meggiolaro, M. T. Trinh, P. P. Joshi, E. Mosconi, S. C. Jones, F. De Angelis und X.-Y. Zhu, *Large polarons in lead halide perovskites*, Science Advances **3**(8) (2017).

[Mon17]   D. M. Monahan, L. Guo, J. Lin, L. Dou, P. Yang und G. R. Fleming, *Room-temperature coherent optical phonon in 2d electronic spectra of ch3nh3pbi3 perovskite as a possible cooling bottleneck*, The Journal of Physical Chemistry Letters **8**(14), S. 3211 (2017), URL `http://dx.doi.org/10.1021/acs.jpclett.7b01357`.

[Mos16]   E. Mosconi, D. Meggiolaro, H. J. Snaith, S. D. Stranks und F. De Angelis, *Light induced annihilation of frenkel defects in organo lead halide perovskites*, Energy and Environmental Science **9**(10), S. 3180 (2016), URL `http://dx.doi.org/10.1039/C6EE01504B`.

[Mos17]   J.-E. Moser, *Perovskite photovoltaics: Slow recombination unveiled*, Nat Mater **16**(1), S. 4 (2017), URL `http://dx.doi.org/10.1038/nmat4796`.

[Nah17] NahS, SpokoynyB, StoumposC, C. M. M. Soe, KanatzidisM und HarelE, *Spatially segregated free-carrier and exciton populations in individual lead halide perovskite grains*, Nat Photon **advance online publication** (2017), URL `http://dx.doi.org/10.1038/nphoton.2017.36`.

[Nah18] S. Nah, B. M. Spokoyny, C. M. M. Soe, C. C. Stoumpos, M. G. Kanatzidis und E. Harel, *Ultrafast imaging of carrier cooling in metal halide perovskite thin films*, Nano Letters (2018), URL `http://dx.doi.org/10.1021/acs.nanolett.7b04520`.

[Nie16a] W. Nie, J.-C. Blancon, A. J. Neukirch, K. Appavoo, H. Tsai, M. Chhowalla, M. A. Alam, M. Y. Sfeir, C. Katan, J. Even, S. Tretiak, J. J. Crochet, G. Gupta und A. D. Mohite, *Light-activated photocurrent degradation and self-healing in perovskite solar cells*, Nature Communications **7**, S. 11574 (2016), URL `http://dx.doi.org/10.1038/ncomms11574`.

[Nie16b] D. Niesner, M. Wilhelm, I. Levchuk, A. Osvet, S. Shrestha, M. Batentschuk, C. Brabec und T. Fauster, *Giant rashba splitting in ch3nh3pbbr3 organic-inorganic perovskite*, Physical Review Letters **117**(12), S. 126401 (2016), URL `https://link.aps.org/doi/10.1103/PhysRevLett.117.126401`.

[Nie16c] D. Niesner, H. Zhu, K. Miyata, P. P. Joshi, T. J. S. Evans, B. J. Kudisch, M. T. Trinh, M. Marks und X. Zhu, *Persistent energetic electrons in methylammonium lead iodide perovskite thin films*, Journal of the American Chemical Society **138**(48), S. 15717 (2016), URL `http://dx.doi.org/10.1021/jacs.6b08880`.

[Nie17] D. Niesner;, M. Hauck;, S. Shrestha;, I. Levchuk;, G. J. Matt;, A. Osvet;, M. Batentschuk;, C. Brabec;, H. B. Weber; und T. Fauster, *Spin-split bands cause the indirect band gap of (ch3nh3)pbi3: Experimental evidence from circular photogalvanic effect*, arXiv e-prints **1703.08740** (2017), URL `https://arxiv.org/abs/1703.08740`.

[Oba17] B. Obama, *The irreversible momentum of clean energy*, Science **355**(6321), S. 126 (2017), URL `https://www.ncbi.nlm.nih.gov/pubmed/28069665`.

[Oga14] H. Oga, A. Saeki, Y. Ogomi, S. Hayase und S. Seki, *Improved understanding of the electronic and energetic landscapes of perovskite solar cells: High local charge carrier mobility, reduced recombination, and extremely shallow traps*, Journal of the American Chemical Society **136**(39), S. 13818 (2014), URL `http://dx.doi.org/10.1021/ja506936f`.

[Osh16] A. Osherov, E. M. Hutter, K. Galkowski, R. Brenes, D. K. Maude, R. J. Nicholas, P. Plochocka, V. Bulovic, T. J. Savenije und S. D. Stranks, *The impact of phase retention on the structural and optoelectronic properties of metal halide perovskites*, Advanced Materials **28**(48), S. 10757 (2016), URL `http://dx.doi.org/10.1002/adma.201604019`.

[OY92] N. Onoda-Yamamuro, T. Matsuo und H. Suga, *Dielectric study of ch3nh3pbx3 (x = cl, br, i)*, Journal of Physics and Chemistry of Solids **53**(7), S. 935 (1992), URL `http://www.sciencedirect.com/science/article/pii/002236979290121S`.

[Pet17] M. L. Petrus, J. Schlipf, C. Li, T. P. Gujar, N. Giesbrecht, P. Müller-Buschbaum, M. Thelakkat, T. Bein, S. Hüttner und P. Docampo, *Capturing the sun: A review of the challenges and perspectives of perovskite solar cells*, Advanced Energy Materials **7**(16), S. 1700264 (2017), URL `http://dx.doi.org/10.1002/aenm.201700264`.

[Pis14] A. Pisoni, J. Jacimovic, O. S. Barisic, M. Spina, R. Gaal, L. Forro und E. Horvath, *Ultra-low thermal conductivity in organic inorganic hybrid perovskite ch3nh3pbi3*, The Journal of Physical Chemistry Letters **5**(14), S. 2488 (2014), URL `http://dx.doi.org/10.1021/jz5012109`.

[PJ16] C. S. Ponseca Jr und V. Sundstrom, *Revealing the ultrafast charge carrier dynamics in organo metal halide perovskite solar cell materials using time resolved thz spectroscopy*, Nanoscale **8**(12), S. 6249 (2016), URL `http://dx.doi.org/10.1039/C5NR08622A`.

[PO16] L. M. Pazos-Outon, M. Szumilo, R. Lamboll, J. M. Richter, M. Crespo-Quesada, M. Abdi-Jalebi, H. J. Beeson, M. Vrucinic, M. Alsari, H. J. Snaith, B. Ehrler, R. H. Friend und F. Deschler, *Photon recycling in lead iodide perovskite solar cells*, Science **351**(6280), S. 1430 (2016).

[Pon14] C. S. Ponseca, T. J. Savenije, M. Abdellah, K. Zheng, A. Yartsev, T. Pascher, T. Harlang, P. Chabera, T. Pullerits, A. Stepanov, J.-P. Wolf und V. Sundström, *Organometal halide perovskite solar cell materials rationalized: Ultrafast charge generation, high and microsecond-long balanced mobilities, and slow recombination*, Journal of the American Chemical Society **136**(14), S. 5189 (2014), URL `http://dx.doi.org/10.1021/ja412583t`.

[Pon17] C. S. Ponseca, P. Chábera, J. Uhlig, P. Persson und V. Sundström, *Ultrafast electron dynamics in solar energy conversion*, Chemical Reviews (2017), URL `http://dx.doi.org/10.1021/acs.chemrev.6b00807`.

[Pri15] M. B. Price, J. Butkus, T. C. Jellicoe, A. Sadhanala, A. Briane, J. E. Halpert, K. Broch, J. M. Hodgkiss, R. H. Friend und F. Deschler, *Hot-carrier cooling and photoinduced refractive index changes in organic-inorganic lead halide perovskites*, Nat Commun **6** (2015), URL `http://dx.doi.org/10.1038/ncomms9420`.

[Qin17] L. Qin, L. Lv, C. Li, L. Zhu, Q. Cui, Y. Hu, Z. Lou, F. Teng und Y. Hou, *Temperature dependent amplified spontaneous emission of vacuum annealed perovskite films*, RSC Advances **7**(26), S. 15911 (2017), URL `http://dx.doi.org/10.1039/C7RA01155E`.

[Qui15] D. W. de Quilettes, S. M. Vorpahl, S. D. Stranks, H. Nagaoka, G. E. Eperon, M. E. Ziffer, H. J. Snaith und D. S. Ginger, *Impact of microstructure on local carrier lifetime in perovskite solar cells*, Science **348**(6235), S. 683 (2015), URL `http://science.sciencemag.org/content/sci/348/6235/683.full.pdf`.

[Rak17] Y. Rakita, O. Bar-Elli, E. Meirzadeh, H. Kaslasi, Y. Peleg, G. Hodes, I. Lubomirsky, D. Oron, D. Ehre und D. Cahen, *Tetragonal ch3nh3pbi3 is ferroelectric*, Proceedings of the National Academy of Sciences **114**(28), S. E5504 (2017), URL `http://www.pnas.org/content/114/28/E5504.abstract`.

[Ric16] J. M. Richter, M. Abdi-Jalebi, A. Sadhanala, M. Tabachnyk, J. P. H. Rivett, L. M. Pazos-Outon, K. C. Gödel, M. Price, F. Deschler und R. H. Friend, *Enhancing photoluminescence yields in lead halide perovskites by photon recycling and light out-coupling*, Nature Communications **7**, S. 13941 (2016), URL `http://dx.doi.org/10.1038/ncomms13941`.

[Ric17] J. M. Richter, F. Branchi, F. Valduga de Almeida Camargo, B. Zhao, R. H. Friend, G. Cerullo und F. Deschler, *Ultrafast carrier thermalization in lead iodide perovskite probed with two-dimensional electronic spectroscopy*, Nature Communications **8**(1), S. 376 (2017), URL `https://doi.org/10.1038/s41467-017-00546-z`.

[RN317] (2017), URL `https://www.nrel.gov/pv/assets/images/efficiency_chart.jpg`.

[Sak16] N. Sakai, S. Pathak, H.-W. Chen, A. A. Haghighirad, S. D. Stranks, T. Miyasaka und H. J. Snaith, *The mechanism of toluene-assisted crystallization of organic-inorganic perovskites for highly efficient solar cells*, Journal of Materials Chemistry A (2016), URL `http://dx.doi.org/10.1039/C6TA01087C`.

[Sal16] M. Saliba, T. Matsui, K. Domanski, J.-Y. Seo, A. Ummadisingu, S. M. Za-keeruddin, J.-P. Correa-Baena, W. R. Tress, A. Abate, A. Hagfeldt und M. Grätzel, *Incorporation of rubidium cations into perovskite solar cells improves photovoltaic performance*, Science **354**(6309), S. 206 (2016), URL `https://www.ncbi.nlm.nih.gov/pubmed/27708053`.

[Sar17] S. P. Sarmah, V. M. Burlakov, E. Yengel, B. Murali, E. Alarousu, A. M. El-Zohry, C. Yang, M. S. Alias, A. A. Zhumekenov, M. I. Saidaminov, N. Cho, N. Wehbe, S. Mitra, I. Ajia, S. Dey, A. E. Mansour, M. Abdelsamie, A. Amassian, I. S. Roqan, B. S. Ooi, A. Goriely, O. M. Bakr und O. F. Mohammed, *Double charged surface layers in lead halide perovskite crystals*, Nano Letters **17**(3), S. 2021 (2017), URL `http://dx.doi.org/10.1021/acs.nanolett.7b00031`.

[Sav14] T. J. Savenije, C. S. Ponseca, L. Kunneman, M. Abdellah, K. Zheng, Y. Tian, Q. Zhu, S. E. Canton, I. G. Scheblykin, T. Pullerits, A. Yartsev und V. Sund-ström, *Thermally activated exciton dissociation and recombination control the carrier dynamics in organometal halide perovskite*, The Journal of Physical Chemistry Letters **5**(13), S. 2189 (2014), URL `http://dx.doi.org/10.1021/jz500858a`.

[Sel17] O. Selig, A. Sadhanala, C. Müller, R. Lovrincic, Z. Chen, Y. L. A. Rezus, J. M. Frost, T. L. C. Jansen und A. A. Bakulin, *Organic cation rotation and immobilization in pure and mixed methylammonium lead-halide perovskites*, Journal of the American Chemical Society (2017), URL `http://dx.doi.org/10.1021/jacs.6b12239`.

[Sen16] M. Sendner, P. K. Nayak, D. A. Egger, S. Beck, C. Muller, B. Epding, W. Kowalsky, L. Kronik, H. J. Snaith, A. Pucci und R. Lovrincic, *Optical phonons in methylammonium lead halide perovskites and implications for charge transport*, Materials Horizons **3**(6), S. 613 (2016), URL `http://dx.doi.org/10.1039/C6MH00275G`.

[She18] H. Shen, T. Duong, J. Peng, D. Jacobs, N. Wu, J. Gong, Y. Wu, S. K. Karuturi, X. Fu, K. Weber, X. Xiao, T. White und K. Catchpole, *Mechanically-stacked perovskite/cigs tandem solar cells with efficiency of 23.9 percent and reduced oxygen sensitivity*, Energy and Environmental Science (2018), URL `http://dx.doi.org/10.1039/C7EE02627G`.

[Shi17a] Z. Shi, Y. Li, Y. Zhang, Y. Chen, X. Li, D. Wu, T. Xu, C. Shan und G. Du, *High-efficiency and air-stable perovskite quantum dots light-emitting diodes with an all-inorganic heterostructure*, Nano Letters **17**(1), S. 313 (2017), URL `http://dx.doi.org/10.1021/acs.nanolett.6b04116`.

[Shi17b] S. S. Shin, E. J. Yeom, W. S. Yang, S. Hur, M. G. Kim, J. Im, J. Seo, J. H. Noh und S. I. Seok, *Colloidally prepared la-doped basno₃ electrodes for efficient, photostable perovskite solar cells*, Science (2017).

[Sho61] W. Shockley und H. J. Queisser, *Detailed balance limit of efficiency of p-n junction solar cells*, Journal of Applied Physics **32**(3), S. 510 (1961).

[Smi15] C. T. Smith, M. A. Leontiadou, R. Page, P. O'Brien und D. J. Binks, *Ultrafast charge dynamics in trap-free and surface-trapping colloidal quantum dots*, Advanced Science **2**(10), S. 1500088 (2015), URL `https://www.ncbi.nlm.nih.gov/pubmed/27980905`.

[Sna14] H. J. Snaith, A. Abate, J. M. Ball, G. E. Eperon, T. Leijtens, N. K. Noel, S. D. Stranks, J. T.-W. Wang, K. Wojciechowski und W. Zhang, *Anomalous hysteresis in perovskite solar cells*, The Journal of Physical Chemistry Letters **5**(9), S. 1511 (2014), URL `http://dx.doi.org/10.1021/jz500113x`.

[Son15] J. Song, J. Li, X. Li, L. Xu, Y. Dong und H. Zeng, *Quantum dot light-emitting diodes based on inorganic perovskite cesium lead halides (cspbx3)*, Advanced Materials **27**(44), S. 7162 (2015), URL `http://dx.doi.org/10.1002/adma.201502567`.

[Ste16] K. X. Steirer, P. Schulz, G. Teeter, V. Stevanovic, M. Yang, K. Zhu und J. J. Berry, *Defect tolerance in methylammonium lead triiodide perovskite*, ACS Energy Letters **1**(2), S. 360 (2016), URL `http://dx.doi.org/10.1021/acsenergylett.6b00196`.

[Sto13] C. C. Stoumpos, C. D. Malliakas und M. G. Kanatzidis, *Semiconducting tin and lead iodide perovskites with organic cations: Phase transitions, high mobilities, and near-infrared photoluminescent properties*, Inorganic Chemistry **52**(15), S. 9019 (2013), URL `http://dx.doi.org/10.1021/ic401215x`.

[Sto17] M. Stolterfoht, C. M. Wolff, Y. Amir, A. Paulke, L. Perdigon-Toro, P. Caprioglio und D. Neher, *Approaching the fill factor shockley-queisser limit in stable, dopant-free triple cation perovskite solar cells*, Energy and Environmental Science **10**(6), S. 1530 (2017), URL `http://dx.doi.org/10.1039/C7EE00899F`.

[Str13]   S. D. Stranks, G. E. Eperon, G. Grancini, C. Menelaou, M. J. P. Alcocer, T. Leijtens, L. M. Herz, A. Petrozza und H. J. Snaith, *Electron-hole diffusion lengths exceeding 1 micrometer in an organometal trihalide perovskite absorber*, Science **342**(6156), S. 341 (2013), URL `http://www.sciencemag.org/content/342/6156/341.abstract`.

[Str14]   S. D. Stranks, V. M. Burlakov, T. Leijtens, J. M. Ball, A. Goriely und H. J. Snaith, *Recombination kinetics in organic-inorganic perovskites: Excitons, free charge, and subgap states*, Physical Review Applied **2**(3), S. 034007 (2014), URL `http://link.aps.org/doi/10.1103/PhysRevApplied.2.034007`.

[Str15a] S. D. Stranks, P. K. Nayak, W. Zhang, T. Stergiopoulos und H. J. Snaith, *Formation of thin films of organic inorganic perovskites for high efficiency solar cells*, Angewandte Chemie International Edition **54**(11), S. 3240 (2015), URL `http://dx.doi.org/10.1002/anie.201410214`.

[Str15b] S. D. Stranks und H. J. Snaith, *Metal halide perovskites for photovoltaic and light emitting devices*, Nat Nanotechnol **10**(5), S. 391 (2015), URL `https://www.ncbi.nlm.nih.gov/pubmed/25947963`.

[Str17]   S. D. Stranks, *Nonradiative losses in metal halide perovskites*, ACS Energy Letters **2**(7), S. 1515 (2017), URL `http://dx.doi.org/10.1021/acsenergylett.7b00239`.

[Sum14]   T. C. Sum und N. Mathews, *Advancements in perovskite solar cells: photophysics behind the photovoltaics*, Energy and Environmental Science **7**(8), S. 2518 (2014), URL `http://dx.doi.org/10.1039/C4EE00673A`.

[Sum16]   T. C. Sum, N. Mathews, G. Xing, S. S. Lim, W. K. Chong, D. Giovanni und H. A. Dewi, *Spectral features and charge dynamics of lead halide perovskites: Origins and interpretations*, Accounts of Chemical Research **49**(2), S. 294 (2016), URL `http://dx.doi.org/10.1021/acs.accounts.5b00433`.

[Tre17]   W. Tress, *Perovskite solar cells on the way to their radiative efficiency limit - insights into a success story of high open-circuit voltage and low recombination*, Advanced Energy Materials S. 1602358 (2017), URL `http://dx.doi.org/10.1002/aenm.201602358`.

[Tri15]   M. T. Trinh, X. Wu, D. Niesner und X. Y. Zhu, *Many-body interactions in photo-excited lead iodide perovskite*, Journal of Materials Chemistry A **3**(17), S. 9285 (2015), URL `http://dx.doi.org/10.1039/C5TA01093D`.

[Ulb11] R. Ulbricht, E. Hendry, J. Shan, T. F. Heinz und M. Bonn, *Carrier dynamics in semiconductors studied with time-resolved terahertz spectroscopy*, Reviews of Modern Physics **83**(2), S. 543 (2011), URL `https://link.aps.org/doi/10.1103/RevModPhys.83.543`.

[VC15] D. A. Valverde-Chavez, C. S. Ponseca, C. C. Stoumpos, A. Yartsev, M. G. Kanatzidis, V. Sundstrom und D. G. Cooke, *Intrinsic femtosecond charge generation dynamics in single crystal ch3nh3pbi3*, Energy and Environmental Science **8**(12), S. 3700 (2015), URL `http://dx.doi.org/10.1039/C5EE02503F`.

[Wan16] Q. Wang, Q. Dong, T. Li, A. Gruverman und J. Huang, *Thin insulating tunneling contacts for efficient and water-resistant perovskite solar cells*, Advanced Materials **28**(31), S. 6734 (2016), URL `http://dx.doi.org/10.1002/adma.201600969`.

[Weh14a] C. Wehrenfennig, G. E. Eperon, M. B. Johnston, H. J. Snaith und L. M. Herz, *High charge carrier mobilities and lifetimes in organolead trihalide perovskites*, Advanced Materials **26**(10), S. 1584 (2014), URL `http://dx.doi.org/10.1002/adma.201305172`.

[Weh14b] C. Wehrenfennig, M. Liu, H. J. Snaith, M. B. Johnston und L. M. Herz, *Charge-carrier dynamics in vapour-deposited films of the organolead halide perovskite ch3nh3pbi3-xclx*, Energy and Environmental Science **7**(7), S. 2269 (2014), URL `http://dx.doi.org/10.1039/C4EE01358A`.

[Weh14c] C. Wehrenfennig, M. Liu, H. J. Snaith, M. B. Johnston und L. M. Herz, *Charge carrier recombination channels in the low-temperature phase of organic-inorganic lead halide perovskite thin films*, APL Materials **2**(8), S. 081513 (2014), URL `http://aip.scitation.org/doi/abs/10.1063/1.4891595`.

[Weh14d] C. Wehrenfennig, M. Liu, H. J. Snaith, M. B. Johnston und L. M. Herz, *Homogeneous emission line broadening in the organo lead halide perovskite ch3nh3pbi3-xclx*, The Journal of Physical Chemistry Letters **5**(8), S. 1300 (2014), URL `http://dx.doi.org/10.1021/jz500434p`.

[Wel15] M. T. Weller, O. J. Weber, J. M. Frost und A. Walsh, *Cubic perovskite structure of black formamidinium lead iodide, hc(nh2)2pbi3, at 298 k*, The Journal of Physical Chemistry Letters **6**(16), S. 3209 (2015), URL `http://dx.doi.org/10.1021/acs.jpclett.5b01432`.

[Wil14]   S. T. Williams, F. Zuo, C.-C. Chueh, C.-Y. Liao, P.-W. Liang und A. K. Y. Jen, *Role of chloride in the morphological evolution of organo-lead halide perovskite thin films*, ACS Nano (2014), URL http://dx.doi.org/10.1021/nn5041922.

[Wol17]   C. Wolf, H. Cho, Y. H. Kim und T. W. Lee, *Polaronic charge carrier-lattice interactions in lead halide perovskites*, ChemSusChem **10**(19), S. 3705 (2017), URL https://www.ncbi.nlm.nih.gov/pubmed/28921874.

[Wri16]   A. D. Wright, C. Verdi, R. L. Milot, G. E. Eperon, M. A. Perez-Osorio, H. J. Snaith, F. Giustino, M. B. Johnston und L. M. Herz, *Electron-phonon coupling in hybrid lead halide perovskites*, Nat Comm. **7**, S. 11755 (2016), URL https://www.ncbi.nlm.nih.gov/pubmed/27225329.

[Wu15a]   X. Wu, M. T. Trinh, D. Niesner, H. Zhu, Z. Norman, J. S. Owen, O. Yaffe, B. J. Kudisch und X. Y. Zhu, *Trap states in lead iodide perovskites*, Journal of the American Chemical Society **137**(5), S. 2089 (2015), URL http://dx.doi.org/10.1021/ja512833n.

[Wu15b]   X. Wu, M. T. Trinh und X. Y. Zhu, *Excitonic many-body interactions in two-dimensional lead iodide perovskite quantum wells*, The Journal of Physical Chemistry C **119**(26), S. 14714 (2015), URL http://dx.doi.org/10.1021/acs.jpcc.5b00148.

[Wu17]   X. Wu, L. Z. Tan, X. Shen, T. Hu, K. Miyata, M. T. Trinh, R. Li, R. Coffee, S. Liu, D. A. Egger, I. Makasyuk, Q. Zheng, A. Fry, J. S. Robinson, M. D. Smith, B. Guzelturk, H. I. Karunadasa, X. Wang, X. Zhu, L. Kronik, A. M. Rappe und A. M. Lindenberg, *Light-induced picosecond rotational disordering of the inorganic sublattice in hybrid perovskites*, Science Advances **3**(7) (2017).

[Xia14a]   M. Xiao, F. Huang, W. Huang, Y. Dkhissi, Y. Zhu, J. Etheridge, A. Gray-Weale, U. Bach, Y.-B. Cheng und L. Spiccia, *A fast deposition-crystallization procedure for highly efficient lead iodide perovskite thin-film solar cells*, Angewandte Chemie International Edition **53**(37), S. 9898 (2014), URL http://dx.doi.org/10.1002/anie.201405334.

[Xia14b]   Z. Xiao, Q. Dong, C. Bi, Y. Shao, Y. Yuan und J. Huang, *Solvent annealing of perovskite-induced crystal growth for photovoltaic-device efficiency enhancement*, Adv Mater **26**(37), S. 6503 (2014), URL http://www.ncbi.nlm.nih.gov/pubmed/25158905.

[Xin13] G. Xing, N. Mathews, S. Sun, S. S. Lim, Y. M. Lam, M. Grätzel, S. Mhaisalkar und T. C. Sum, *Long-range balanced electron- and hole-transport lengths in organic-inorganic ch3nh3pbi3*, Science **342**(6156), S. 344 (2013), URL `http://www.sciencemag.org/content/342/6156/344.abstract`.

[Xin14] G. Xing, N. Mathews, S. S. Lim, N. Yantara, X. Liu, D. Sabba, M. Grätzel, S. Mhaisalkar und T. C. Sum, *Low-temperature solution-processed wavelength-tunable perovskites for lasing*, Nat Mater **13**(5), S. 476 (2014), URL `http://dx.doi.org/10.1038/nmat3911`.

[Yam15] Y. Yamada, M. Endo, A. Wakamiya und Y. Kanemitsu, *Spontaneous defect annihilation in ch3nh3pbi3 thin films at room temperature revealed by time-resolved photoluminescence spectroscopy*, The Journal of Physical Chemistry Letters **6**(3), S. 482 (2015), URL `http://dx.doi.org/10.1021/jz5026596`.

[Yan15] Y. Yang, D. P. Ostrowski, R. M. France, K. Zhu, J. van de Lagemaat, J. M. Luther und M. C. Beard, *Observation of a hot-phonon bottleneck in lead-iodide perovskites*, Nat Photon **10**(1), S. 53 (2015), URL `http://dx.doi.org/10.1038/nphoton.2015.213`.

[Yan17a] W. S. Yang, B.-W. Park, E. H. Jung, N. J. Jeon, Y. C. Kim, D. U. Lee, S. S. Shin, J. Seo, E. K. Kim, J. H. Noh und S. I. Seok, *Iodide management in formamidinium lead halide based perovskite layers for efficient solar cells*, Science **356**(6345), S. 1376 (2017).

[Yan17b] Y. Yang, M. Yang, D. Moore, Y. Yan, E. Miller, K. Zhu und M. Beard, *Top and bottom surfaces limit carrier lifetime in lead iodide perovskite films*, Nature Energy **2**, S. 16207 (2017), URL `http://dx.doi.org/10.1038/nenergy.2016.207`.

[Yin14a] W.-J. Yin, T. Shi und Y. Yan, *Unique properties of halide perovskites as possible origins of the superior solar cell performance*, Advanced Materials **26**(27), S. 4653 (2014), URL `http://dx.doi.org/10.1002/adma.201306281`.

[Yin14b] W.-J. Yin, T. Shi und Y. Yan, *Unusual defect physics in ch3nh3pbi3 perovskite solar cell absorber*, Applied Physics Letters **104**(6), S. (2014), URL `http://scitation.aip.org/content/aip/journal/apl/104/6/10.1063/1.4864778`.

[Yu16] Z.-G. Yu, *Rashba effect and carrier mobility in hybrid organic inorganic perovskites*, The Journal of Physical Chemistry Letters **7**(16), S. 3078 (2016), URL `http://dx.doi.org/10.1021/acs.jpclett.6b01404`.

[Zeg11] B. V. Zeghbroeck, *Principles of semiconductor devices* (2011), URL `http://ecee.colorado.edu/~bart/book/`.

[Zha16a] M.-J. Zhang, N. Wang, S.-P. Pang, Q. Lv, C.-S. Huang, Z.-M. Zhou und F.-X. Ji, *Carrier transport improvement of ch3nh3pbi3 film by methylamine gas treatment*, ACS Applied Materials and Interfaces **8**(45), S. 31413 (2016), URL `http://dx.doi.org/10.1021/acsami.6b10418`.

[Zha16b] W. Zhang, G. E. Eperon und H. J. Snaith, *Metal halide perovskites for energy applications*, Nature Energy **1**, S. 16048 (2016), URL `http://dx.doi.org/10.1038/nenergy.2016.48`.

[Zha16c] T. Zhao, S. T. Williams, C.-C. Chueh, D. W. deQuilettes, P.-W. Liang, D. S. Ginger und A. K. Y. Jen, *Design rules for the broad application of fast (<1 s) methylamine vapor based, hybrid perovskite post deposition treatments*, RSC Advances **6**(33), S. 27475 (2016), URL `http://dx.doi.org/10.1039/C6RA03485C`.

[Zha17a] M. Zhang, X. Zhang, L.-Y. Huang, H.-Q. Lin und G. Lu, *Charge transport in hybrid halide perovskites*, Physical Review B **96**(19), S. 195203 (2017), URL `https://link.aps.org/doi/10.1103/PhysRevB.96.195203`.

[Zha17b] Z. Zhang, R. Long, M. V. Tokina und O. V. Prezhdo, *Interplay between localized and free charge carriers can explain hot fluorescence in the ch3nh3pbbr3 perovskite: Time-domain ab initio analysis*, Journal of the American Chemical Society (2017), URL `http://dx.doi.org/10.1021/jacs.7b06401`.

[Zhe15a] F. Zheng, L. Z. Tan, S. Liu und A. M. Rappe, *Rashba spin orbit coupling enhanced carrier lifetime in ch3nh3pbi3*, Nano Letters **15**(12), S. 7794 (2015), URL `http://dx.doi.org/10.1021/acs.nanolett.5b01854`.

[Zhe15b] Y. C. Zheng, S. Yang, X. Chen, Y. Chen, Y. Hou und H. G. Yang, *Thermal induced volmer weber growth behavior for planar heterojunction perovskites solar cells*, Chemistry of Materials (2015), URL `http://dx.doi.org/10.1021/acs.chemmater.5b01924`.

[Zho15] Z. Zhou, Z. Wang, Y. Zhou, S. Pang, D. Wang, H. Xu, Z. Liu, N. P. Padture und G. Cui, *Methylamine gas induced defect healing behavior of ch3nh3pbi3 thin films for perovskite solar cells*, Angew Chem Int Ed Engl **54**(33), S. 9705 (2015).

[Zho16] Y. Zhou, M. Yang, S. Pang, K. Zhu und N. P. Padture, *Exceptional morphology-preserving evolution of formamidinium lead triiodide perovskite thin films via organic-cation displacement*, Journal of the American Chemical Society (2016), URL `http://dx.doi.org/10.1021/jacs.6b02787`.

[Zhu15a] H. Zhu, Y. Fu, F. Meng, X. Wu, Z. Gong, Q. Ding, M. V. Gustafsson, M. T. Trinh, S. Jin und X. Y. Zhu, *Lead halide perovskite nanowire lasers with low lasing thresholds and high quality factors*, Nat Mater **14**(6), S. 636 (2015), URL `http://dx.doi.org/10.1038/nmat4271`.

[Zhu15b] X. Y. Zhu und V. Podzorov, *Charge carriers in hybrid organic inorganic lead halide perovskites might be protected as large polarons*, The Journal of Physical Chemistry Letters **6**(23), S. 4758 (2015), URL `http://dx.doi.org/10.1021/acs.jpclett.5b02462`.

[Zhu16] H. Zhu, K. Miyata, Y. Fu, J. Wang, P. P. Joshi, D. Niesner, K. W. Williams, S. Jin und X.-Y. Zhu, *Screening in crystalline liquids protects energetic carriers in hybrid perovskites*, Science **353**(6306), S. 1409 (2016).

[Zhu17] H. Zhu, M. T. Trinh, J. Wang, Y. Fu, P. P. Joshi, K. Miyata, S. Jin und X. Y. Zhu, *Organic cations might not be essential to the remarkable properties of band edge carriers in lead halide perovskites*, Adv Mater **29**(1), S. 1603072 (2017), URL `https://www.ncbi.nlm.nih.gov/pubmed/27792264`.